# In Situ X-ray Spectroscopy and Environmental TEM Study on Manganite Water Oxidation Catalysts

## DISSERTATION

zur Erlangung des mathematisch-naturwissenschaftlichen Doktorgrades
„Doctor rerum naturalium“
der Georg-August-Universität Göttingen
——
im Promotionsprogramm ProPhys
der Georg-August University School of Science (GAUSS)

vorgelegt von
**Daniel Joachim Mierwaldt**
aus Oldenburg (Oldb)

Göttingen, 2017

## Betreuungsausschuss

Prof. Dr. Christian Jooß, Institut für Materialphysik
Prof. Dr. Simone Techert, Institut für Röntgenphysik

## Mitglieder der Prüfungskommission

| | |
|---|---|
| Referent: | Prof. Dr. Christian Jooß, Institut für Materialphysik |
| Korreferentin: | Prof. Dr. Simone Techert, Institut für Röntgenphysik |

## Weitere Mitglieder der Prüfungskommission

Prof. Dr. Inke Siewert
Prof. Dr. Michael Seibt
PD Dr. Martin Wenderoth
Prof. Dr. Wolfram Kollatschny

**Tag der mündlichen Prüfung: 01.11.2017**

# Contents

# Chapter 1

# General Scientific Background

## 1.1 Motivation

The depletability of fossil fuels and the effect of greenhouse gas emissions on global warming highlight the urgent need for a renewable and sustainable energy supply. [1,2] Presently, most renewable energy is generated as electricity from intermittent sources, namely wind and sunlight. Therefore, one of the greatest challenges for replacing fossil energy appears to be storing electrical energy and providing fuels for mobile and heating applications. Storing energy in chemical bonds by producing artificial fuels from water splitting is a promising method to meet this requirement at large scale. Such a scenario of molecular hydrogen or hydrocarbon production is depicted in Figure 1.1. The efficiency of this system is however strongly limited by the catalysis of the oxygen evolution reaction (OER) by water oxidation. [3]

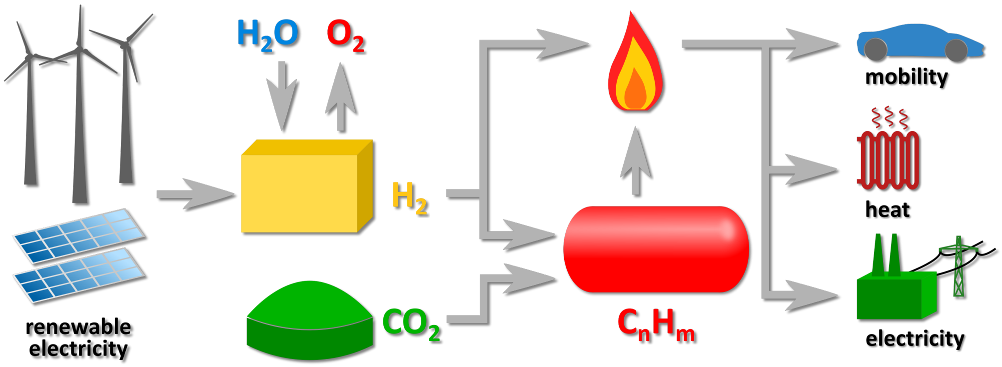

**Figure 1.1:** Schema of energy storage via artificial fuels ($H_2$ or various hydrocarbons). The energy can be used in fuel cells, engines or burners.

Water splitting is mainly performed by either polymer electrolyte membrane (PEM) or aqueous electrolysis.[4] For reasons of electrochemical stability of the catalysts, aqueous electrolysis is usually performed in alkaline media.[5] In contrast, acidic PEMs (proton exchange membranes) are much more stable than their alkaline counterparts (anion exchange membranes).[6] State-of-the-art PEM electrolysis requires highly pure water and noble metal oxide catalysts ($RuO_x$, $IrO_x$, Pt).[7–14] Aqueous electrolysis can be performed with earth-abundant catalyst materials (mainly Ni-alloys), but suffers from particularly low efficiencies.[15–21] These are some of the reasons why up to 96 % of present-day hydrogen production is based on fossil fuel reforming instead of water splitting.[21–23]

Transition metal oxides (TMOs) have received much attention in the field of oxygen evolution catalysis because of their flexible iono-covalent transition metal-oxygen bonds.[24–26] Particular interest lies in first-row TMOs due to their high abundance and relatively low price.[27] Manganese is one of the most studied transition metals for OER. [28–36] Perhaps the most prominent OER catalyst is the oxygen evolving complex (OEC) that is employed by the natural photosynthesis of green plants, cyanobacteria, and algae as part of the photosystem II.[37] The OEC serves as a blueprint for efficient OER catalysis by utilizing the flexible Mn valence (here 3+/4+) as well as a flexible structure around the active site. It consists of a $Mn_4CaO_5$ cluster and has produced the $O_2$ accounting for 21 % of earth's atmosphere.[38–41] (Figure 1.2)

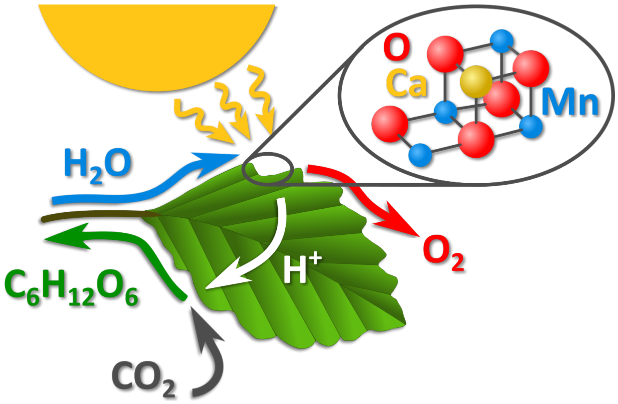

**Figure 1.2:** Simplified schema of natural photosynthesis focusing on water splitting by the $Mn_4CaO_5$ oxygen evolving complex in photosystem II.

Much effort has been made to reveal its OER mechanism, the so-called S-cycle. The system goes through a series of states (S0 - S4), in which the number represents the amount of accumulated oxidizing equivalents through oxidation of the neighboring Mn cations, while Ca (and Cl) are needed as cofactor.[42] The redox-inactive $Ca^{2+}$ modulates the reduction potentials stabilizing the critical high-valence $Mn_4^{4+}$ configuration needed for $O_2$ release.[43–45] The structure and complex reaction cycle of the OEC have inspired the search for artificial catalysts based on TMOs and perovskites in particular, as discussed in section 1.2. In particular, strongly correlated manganite perovskites offer opportunities for tuning the surface electronic structure.

A systematic search for useful, i.e. active and stable, OER catalysts requires an understanding of the underlying reaction mechanisms. However, during the reaction catalyst surfaces usually significantly differ from their equilibrium state, featuring different species and configurations as active sites. The nature of these sites in turn determines the corresponding reaction sequence. Studying catalysts in their active states by in situ techniques is therefore indispensable for identifying and characterizing reaction mechanisms.

This thesis presents in situ studies on the active states of manganite catalysts in $H_2O$ vapor. The study in chapter 2 probes the surface electronics of the strongly correlated $Pr_{1-x}Ca_xMnO_3$ ($0 \leq x \leq 0.8$) by in situ X-ray absorption and photoemission (XANES, XPS). Chapter 3 presents an environmental transmission electron microscopy (ETEM) study comparing the microscopic processes in $Pr_{1-x}Ca_xMnO_3$ ($x = 0.1$, 0.3) and the related layered Ruddlesden-Popper system $Pr_{0.5}Ca_{1.5}MnO_4$. A discussion about gas phase electrochemistry and further information on the experimental techniques is provided in section 1.3.

## 1.2 Perovskites as OER Catalysts

Several perovskites were found to be well-performing OER catalysts.[3,27,28,46–52] Perovskites are described by the general formula $ABO_3$, where the A-cation is commonly a rare-earth ($A^{3+}$) or alkaline earth ($A^{2+}$) element and the B-cation usually a transition metal ($B^{3+/4+}$) forming iono-covalent bonds with the oxygen ligands. The cubic parent structure is comprised of corner-sharing $BO_6$ octahedra with dodecahedrally coordinated A-cations in between. In other words, it is formed by oxygen ligand bridges between octahedrally coordinated transition metals in proximity to redox-inactive A-cations and therefore bares resemblance to the OEC.[40] The lattice sites can be doped almost independently because their ionic radii differ by a factor of about $\sqrt{2}$. Heterovalent substitution of A-cations can be used to tune the formal transition metal valence, while A-cations of different ionic radii tune distance, angle and hybridization of the transition metal oxygen bonds by tilting and stretching of the octahedra. These effects determine the electronic structure near the Fermi energy, which makes perovskites a very versatile and tunable material class and particularly interesting for scientific research.[53–55]

In particular, the small ionic radii of $Pr^{3+}$ and $Ca^{2+}$ in the perovskite $Pr_{1\text{-}x}Ca_xMnO_3$ (PCMO) cause strong tilting of the $MnO_6$ octahedra. This is reflected by a small Goldschmidt tolerance factor of $t \approx 0.94$ and results in an orthorombic unit cell with Mn-O-Mn bond angles between 152 and 157° instead of the 180° in cubic perovskites.[56,57] While a detailed description of the complex electronic structure is presented in ref. [58], its essential features are outlined in the following. Hybridization with the O 2p states in octahedral symmetry reduces the degeneracy of the Mn 3d states by splitting them into 3 $t_{2g}$ and 2 $e_g$ states. Hund's coupling with the large magnetic moment of the Mn cations leads to a high spin electron configuration of $t_{2g}^3\ e_g^{1\text{-}x}$ per Mn. The doping-dependent partial filling of the $e_g$ band causes distortions of the octahedra and further band splitting due to the Jahn-Teller effect. The splitting vanishes in $CaMnO_3$ ($e_g^0$) and is maximal in $PrMnO_3$ ($e_g^1$). Octahedral tilting and distortions reduce overlap of the hybridized Mn 3d and O 2p orbitals, producing narrow bands.[59] Moreover, strong electron-phonon coupling causes formation of small polarons with low mobility. Electron-electron coupling additionally affects the complex electronic structure of the valence and conduction bands. The upper valence band of $CaMnO_3$ is dominated by O 2p states. However, the band edge character transforms into the lower Jahn-Teller $e_g$ band upon electron doping due to replacement of $Ca^{2+}$ by $Pr^{3+}$ or formation of oxygen vacancies. The character of valence states is of particular interest during electron insertion by water oxidation catalysis.

Water splitting occurs via two half reactions, the hydrogen evolution reaction (HER) and the oxygen evolution reaction (OER). In alkaline media, they can be summarized by:

$$2\,H_2O + 2\,e^- \longrightarrow H_2 + 2\,OH^- \tag{HER}$$

$$4\,OH^- \longrightarrow O_2 + 2\,H_2O + 4\,e^- \tag{OER}$$

The equilibrium potentials with respect to the reversible hydrogen electrode (RHE) are 0 V for the HER and 1.23 V for the OER.[60,61] The requirement to transfer four electrons for the production of one $O_2$ molecule makes the OER the rate and efficiency limiting half reaction.[2,3,50,62–65] The overall free energy difference is 4.92 eV, or 1.23 eV per transferred electron. The subsequent transfer of electrons requires involvement of at least four intermediate states of the active site. To perform the corresponding reaction sequence at high efficiency, i.e. low overpotential, the (binding) energy of each intermediate state must be neither too low, nor too high. This coarse requirement is called the Sabatier's principle.[66] The detailed reaction sequence depends on the particular catalyst and is difficult to identify.

For perovskites, mainly two opposing principle mechanisms are discussed. A computationally derived mechanism, originally discussed for metal surfaces, considers O-based adsorbates ($OH^* \rightarrow O^* \rightarrow OOH^* \rightarrow OO^*$) on a single redox-active surface B-site.[67,68] This requires sufficiently flexible valence of the B-cation, which is alternately oxidized and reduced in each of the 4 reaction steps. The reaction cycle of hydroxide adsorption and subsequent deprotonation is depicted in Figure 1.3.

An ideal catalyst would bind all 4 adsorbates equally strong, so that the free energy difference $\Delta G_i$ equals 1.23 eV for each of the 4 reaction steps. Efficiency limiting overpotentials of real catalysts are thus the result of deviations from this condition. Computational work has shown that for real catalysts the adsorption energies are universally correlated.[68–70] The relative energy of the double bonded O* intermediate ($\Delta G_{O^*}$) determines whether step 1 or 2 is rate-limiting. Too strong adsorbate binding hampers the deprotonation of OH* (step 1), while too weak binding hampers the subsequent OH* adsorption (step 2). More importantly, a universal free energy difference $\Delta G_{OOH^*} - \Delta G_{OH^*}$ of approximately 3.0 - 3.4 eV has been found.[71] Given this mechanism, the combination of reaction steps 1 and 2 will therefore always considerably exceed the ideal value of $\Delta G_{1+2} = 2.46$ eV.[72]

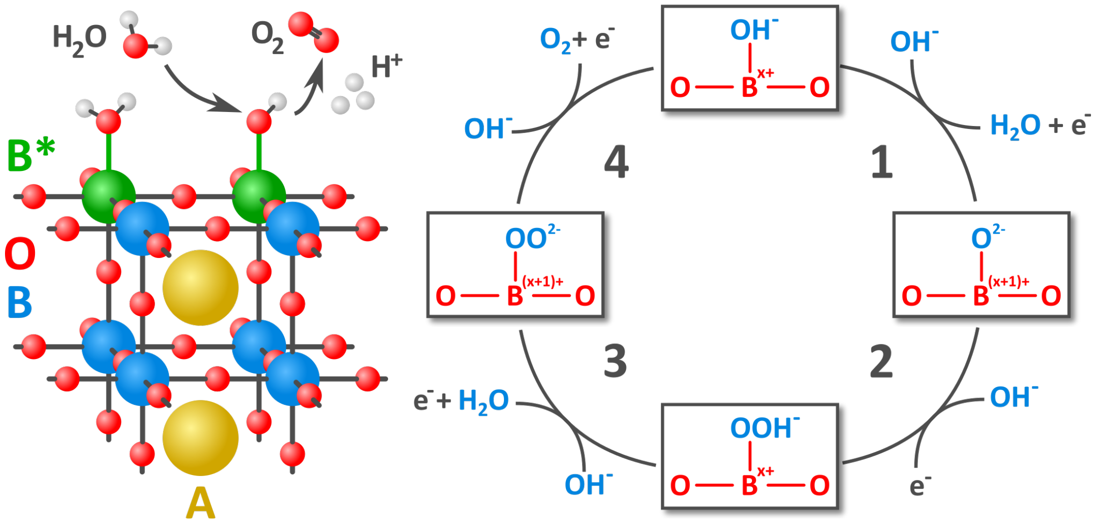

**Figure 1.3:** Adsorbate-based OER mechanism for perovskite catalysts in alkaline media. A redox-active B-cation binds different O-based intermediate species created by $OH^-$ adsorption (steps 2 and 4) and their subsequent deprotonation (steps 1 and 3).

More recent work proposes a model mechanism that includes the formation of oxygen vacancies for perovskites with high covalence of the B-O bond.[73–76] Covalent bond character, i.e. stronger O 2p contributions to the anti-bonding molecular orbitals, facilitates the formation of ligand holes which in turn promote O vacancies.[73, 77–80] In addition, recent theoretical work suggests that vacancy formation is especially triggered by introduction of holes in non-bonding atomic O 2p states which exhibit higher reactivity in comparison to the more delocalized B-O molecular orbitals.[80–82] The corresponding reaction sequence of a vacancy involving mechanism is presented in Figure 1.4. The essential difference to the purely adsorbate-based mechanism is that deprotonation of the OH* adsorbate in step 1 is associated with reorganization of the surface. In this scenario, the unstable terminal O* adsorbate binds to a neighboring lattice O, forming the $O_2$ molecule which is released from the B-cation in step 2. The thereby created vacancy is reoccupied by $OH^-$ in step 3.

Notably, such a mechanism does not involve O* or OOH* adsorbates, so that the energetic scaling relations of the adsorbate mechanism do not apply. Accordingly, lattice oxygen involvement is found for several highly active rutile OER catalysts.[83–85] However, the tendency to form oxygen vacancies is generally correlated with low thermodynamic and electrochemical stability, as further discussed in chapters 2 and 3.[86, 87] The character of hole states, which are introduced by the charge transfer during water oxidation, may therefore determine the amount of formed oxygen vacancies and, in addition, if the vacancies create a stable surface phase or lead to corrosion.

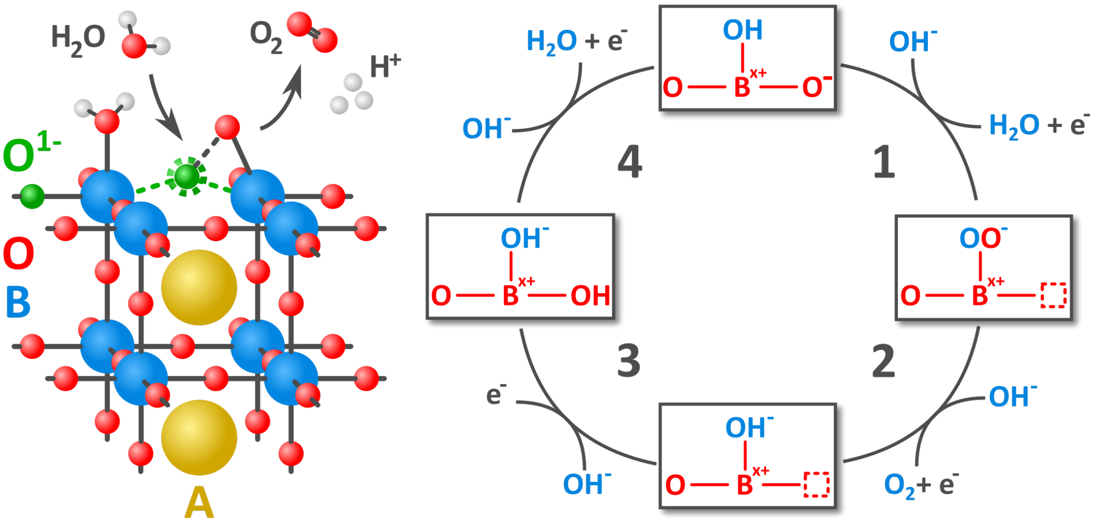

**Figure 1.4:** Lattice oxygen involving OER mechanism for perovskite catalysts in alkaline media. A surface oxygen vacancy is formed by reorganization of the terminal O* adsorbate to form $O_2$ (step 1), which is released in step 2. The vacancy is reoccupied by $OH^-$ in step 3 and deprotonated in step 4.

The involvement or exclusion of lattice oxygen presents an important fundamental difference in OER pathway. However, catalysts may favor various different reaction sequences that differ from the two proposed ones. In situ experiments can therefore provide valuable information on the formation processes of active catalyst surfaces. In situ spectroscopies probe factors like chemical composition, transition metal valence, bond covalence, and additional doping by formation of point defects like oxygen vacancies, while in situ electron microscopy provides information on surface morphology, atom dynamics, structural stability, and spatial distribution of valence states. For $Pr_{1-x}Ca_xMnO_3$, the in situ studies in chapters 2 and 3 give strong evidence for oxygen vacancy involvement in OER leading to doping-dependent corrosion. In contrast, the ETEM experiments show that the Ruddlesden-Popper type $Pr_{0.5}Ca_{1.5}MnO_4$ phase is much more stable, suggesting that it rather favors a metal centered mechanism as depicted in Figure 1.3.

## 1.3 Techniques for In Situ Investigation of Catalyst Surfaces in Gases

In this thesis, the experimental methods of in situ X-ray spectroscopy (XANES/XPS) and environmental transmission electron microscopy (ETEM) are used to study electrochemical reactions at solid-gas interfaces. The comparability of such observations with conventional electrochemical experiments is challenged by the use of $H_2O$ vapor in the µbar to mbar range instead of liquid electrolytes. [88]. Several aspects have to be considered when comparing and contrasting gas phase with liquid electrochemistry as depicted in Figure 1.5. First, according to the Nernst equation, equilibrium redox potentials depend on the activities of involved species which are determined by their partial pressure and therefore likely to differ from experiments in ambient pressure liquids. [89]

The second aspect concerns the electrolyte's conductivity. Liquid electrolytes exhibit high ionic conductivity which supplies the catalyst with reagents and dissipates reaction products. In addition, mass transport is usually experimentally enhanced by the use of rotating electrodes. [90] Moreover, buffer solutions stabilize the pH near oxygen or hydrogen evolving electrodes. [61,89,91] Contrarily, ion concentration and conductivity in gases is generally low although some conductivity may be generated by ionizing radiation. Also, in the thin liquid $H_2O$ layer which condenses on the catalyst surface when in contact with the vapor mass transport kinetics may differ due to its small volume. However, the continuously pumped and replenished vapor phase represents a reservoir which is only limited by the exchange kinetics across the liquid-gas interface.

Thirdly, the charge double layer created by alignment of the polar $H_2O$ molecules and ion migration may differ significantly. This affects the potential drop across the catalyst-electrolyte interface which is the driving force for redox reactions. In summary, some uncertainty about the electrochemical driving forces is produced by the combination of ionic transport in the low pressure vapor phase, across its interfaces with the liquid surface layers and within these layers as well as the effects of the charge double layers. On the other hand, the generally highly conductive liquid electrolytes can be regarded as equipotential volumes confining the potential drops to the thin charge double layers on the catalyst surfaces. However, when combined with conventional electrochemistry, in situ gas phase spectroscopy provides valuable complimentary information.

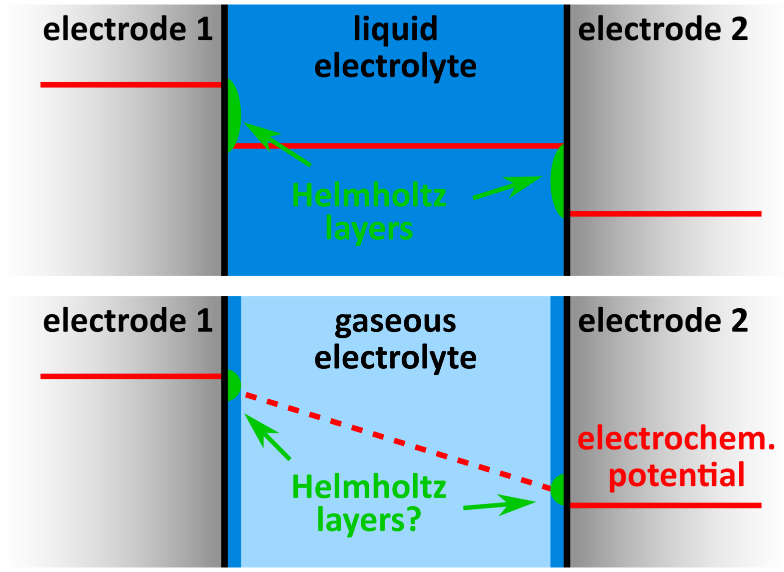

**Figure 1.5:** Schematic electrochemical potential distribution for 2-electrode electrochemistry contrasting liquid electrolytes with vapor phases. In liquid electrolyte, potential drops are confined to the thin charge double layers on the electrode surfaces. Gaseous electrolytes produce a more complex situation including condensed liquid surface layers.

### 1.3.1 In Situ X-Ray Spectroscopy (XANES/XPS)

X-ray absorption near-edge spectroscopy (XANES) and X-ray photoelectron spectroscopy (XPS) provide valuable information on redox processes like the OER because they probe the involved electronic states with high surface sensitivity and can be performed in situ by using $H_2O$ vapor or other gaseous environments.[92, 93] Changes in chemical composition, oxidation states and binding strengths define the processes that are involved in formation of active catalyst surfaces. The use of monochromated soft X-ray synchrotron radiation on manganite catalysts grants access to the hybridized Mn 3d - O 2p bands near the Fermi level. XANES probes excitations into the unoccupied states above the Fermi energy as a function of excitation photon energy. Instead, XPS measures the kinetic energy of photoelectrons from the occupied core or valence states at fixed excitation energy.

X-ray photons have a small scattering cross section with the specimen material and therefore a large penetration depth. However, photo-excited electrons are strongly reabsorbed within the specimen limiting the probing depth to the escape depth of the detected electrons. This amounts to about 1 - 2 nm for XPS using primary photoelectrons with kinetic energy of about 200 eV. In contrast, the total electron yield (TEY) used as XANES signal additionally contains Auger and secondary electrons from the specimen of various energies and therefore various escape depths as well as further secondary electrons from scattering with gas molecules. In the case of PCMO, 99.9 % of the TEY signal originate from the topmost 6 – 7 nm as discussed in section 2.2.[94]

The apparatus used for the study in chapter 2 was developed at the Fritz-Haber-Institut of the Max-Planck-Gesellschaft and is schematically depicted in Figure 1.6.[95, 96] The plane-grating monochromator selects the desired wavelength from the synchrotron radiation, which is being focussed onto a approximately 150 x 250 $\mu m^2$ area on the catalyst surface. Emitted photoelectrons are being focussed by electromagnetic lenses onto the entrance slit of a hemispherical analyzer. A differential pumping system maintains ultra-high vacuum within the analyzer, while reaction gases are let into the specimen chamber at up to mbar pressure range.

Electrochemical surface reactions can be driven by external biasing. The resulting surface potential is directly reflected by a shift in kinetic energy of the photoelectrons, which are decelerated (positive bias) or accelerated (negative bias). Moreover, Arrigo et al. demonstrated bias control over OER/HER at Pt nanoparticles in low pressure XPS experiments, measuring $O_2/H_2$ by mass spectrometer attached to the chamber.[97]

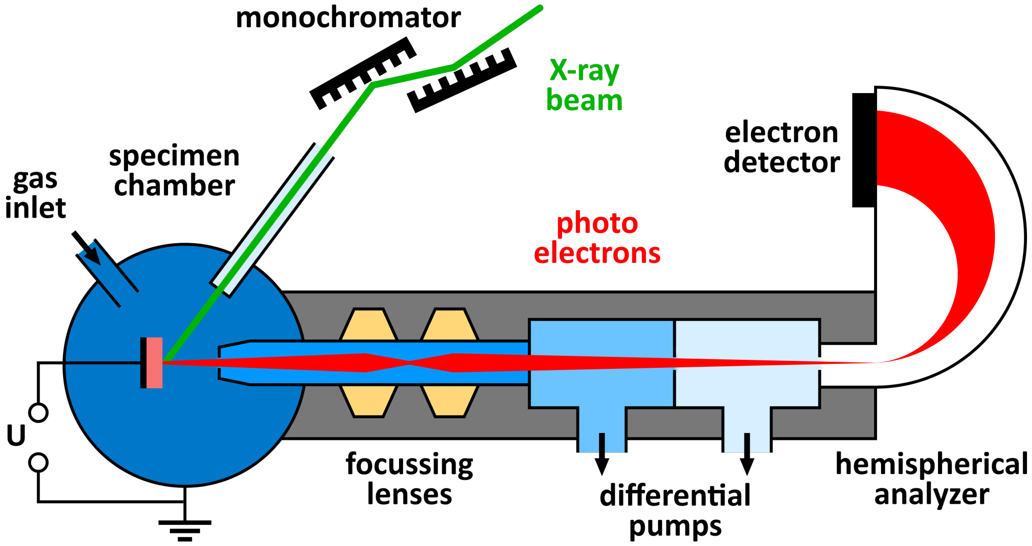

**Figure 1.6:** Schema of in situ XANES/XPS endstation, including a plane-grating monochromator, electromagnetic focusing lenses for the photoelectrons and a hemispherical analyzer. Differential pumping maintains ultra-high vacuum in the analyzer, while gas is introduced into the specimen chamber.

### 1.3.2 Environmental Transmission Electron Microscopy (ETEM)

The active state of electrode surfaces always varies from the equilibrium structure of the catalysts.[98–103] Analytical ETEM is a powerful complementary approach to in situ X-ray techniques because it provides atomically resolved information on structure and morphology under working conditions.[88, 104, 105] The technique allows real-time imaging of defect dynamics and morphological changes like the formation of nano-sized crystals as presented in chapter 3. This is supplemented by spectroscopic information on chemical composition and electronic structure via electron energy loss spectroscopy (EELS) and energy-dispersive X-Ray spectroscopy (EDX) with nanometer resolution in scanning transmission electron microscopy mode (STEM).

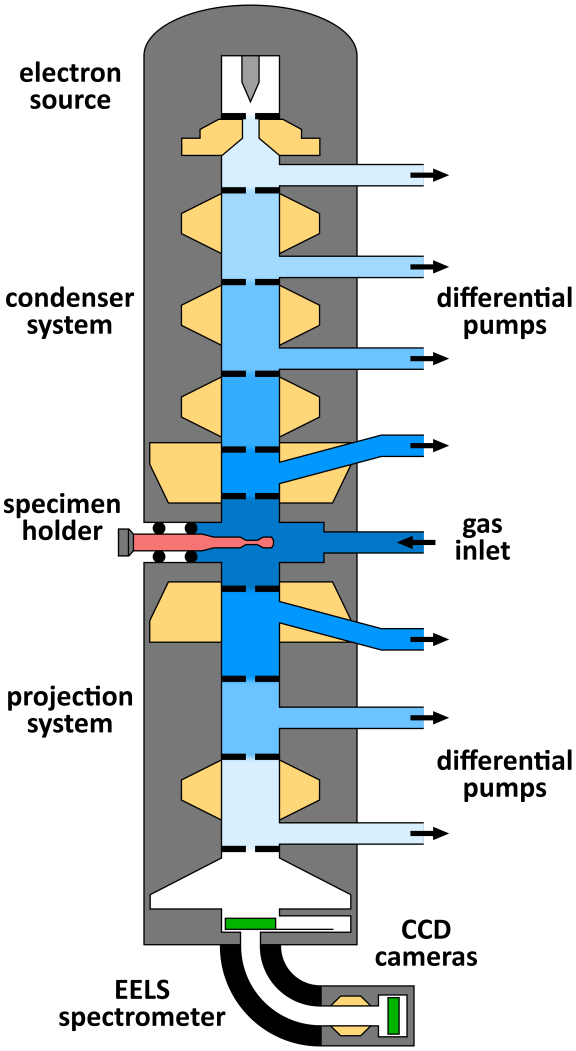

**Figure 1.7:** Schema of the differentially pumped column of an ETEM. Reaction gases can be inserted into the octagon (specimen chamber), while high vacuum is maintained at the bottom-mounted cameras and detectors and ultra-high vacuum is maintained at the electron gun.

The essential feature of an ETEM is the integration of a differential pumping system into the column. Figure 1.7 shows a schematic representation of such a system. It allows to expose specimen to gases at pressures up to several tens of mbar, while keeping the crucial ultra-high vacuum below $10^{-9}$ mbar at the electron source.[106–110] Correction of aberrations (e.g. spherical $C_s$) caused by imperfections of electromagnetic lenses allows sub-nanometer spatial resolution.[111–115] For high resolution studies, TEM specimens must be significantly thinner than the mean free path $\lambda$ of the high-energy beam electrons (usually 80 – 300 keV). Depending on its density the specimen's thickness is usually below approximately 50 nm. Negative specimen charging due to beam electron injection is therefore usually negligible. However, inelastic scattering excites electrons from the specimens valence band and core states, resulting in emission of secondary and Auger electrons.[116,117] (Figure 1.8) This provides local positive charging, which can be used to drive (anodic) electrochemical surface reactions with the gaseous electrolyte. Charging of manganite TEM specimens was adressed in more detail by earlier work including off-axis electron holography and electrostatic modeling.[88,105,118]

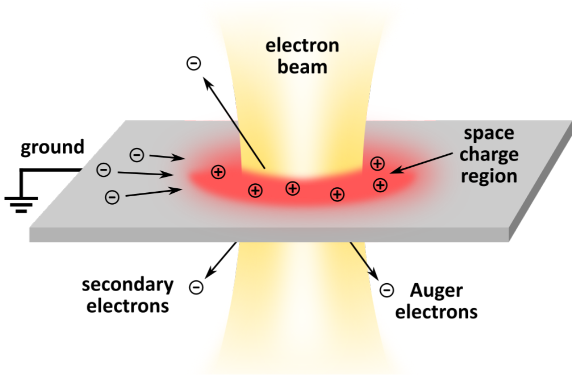

**Figure 1.8:** Beam-induced specimen charging in a TEM. Inelastic scattering causes emission of Auger and secondary electrons. Thereby generated positive space charge saturates due to compensation by ground current and backflow from the environment.

A major challenge of ETEM in terms of comparability with other in situ techniques is the large impact of high-energy electrons on the specimen, e.g. due to a four orders of magnitude higher scattering cross section in comparison to (X-ray) photons. The benefit of local electronic potentials comes with the risk of radiation damage, which must be considered and preferably avoided.[119] Specimen atoms can be displaced or even desorbed by knock-on damage, which depends on the impinging electron energy as well as on atomic masses and binding strengths of the material. Knock-on damage also depends on electron flux and density due to balance of induced displacements and their relaxation. High energy and flux densities may therefore lead to mass loss, structural damage and heating.[120] For the study presented in chapter 3, beam damage effects have been ruled out by control experiments in high vacuum or inert gases. The experiments thus demonstrate the possibility to generate beam-induced potentials for driving electrochemistry at beam fluxes below the damage threshold of the catalyst material.

# Chapter 2

# In Situ XANES/XPS Investigation

This chapter is a reproduction of the following original publication:

## In Situ XANES/XPS Investigation of Doped Manganese Perovskite Catalysts

***Daniel Mierwaldt***, *Stephanie Mildner*, *Rosa Arrigo*, *Axel Knop-Gericke*, *Emanuel Franke*, *Andreas Blumenstein*, *Jörg Hoffmann*, *and Christian Jooss*

*Catalysts* **2014**, *4*(2), 129-145; doi: 10.3390/catal4020129

References, labels and arrangement of figures have been modified to suit this thesis.

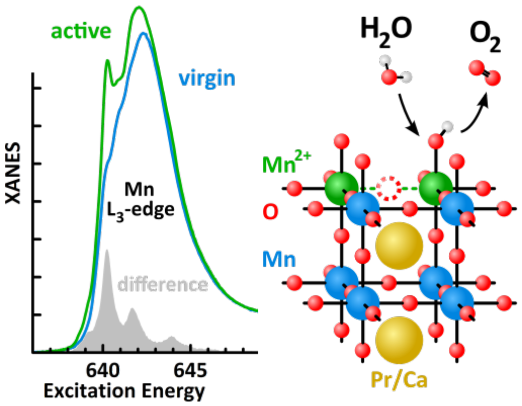

**Abstract** Studying catalysts in situ is of high interest for understanding their surface structure and electronic states in operation. Herein, we present a study of epitaxial manganite perovskite thin films ($Pr_{1-x}Ca_xMnO_3$) active for the oxygen evolution reaction (OER) from electrocatalytic water splitting. X-ray absorption near-edge spectroscopy (XANES) at the Mn L- and O K-edges, as well as X-ray photoemission spectroscopy (XPS) of the O 1s and Ca 2p states have been performed in ultra-high vacuum and in water vapor under positive applied bias at room temperature. It is shown that under the oxidizing conditions of the OER a reduced $Mn^{2+}$ species is generated at the catalyst surface. The Mn valence shift is accompanied

by the formation of surface oxygen vacancies. Annealing of the catalysts in $O_2$ atmosphere at 120 °C restores the virgin surfaces.

## 2.1 Introduction

The search for new energy storage technologies has sparked interest in electrocatalytic water splitting. Its overall efficiency is limited by the oxygen evolution reaction (OER). This half reaction can currently only be driven at high overpotentials because of limiting high potential steps in the multi-electron transfer reaction, where the formation of one $O_2$ molecule requires the cooperative transfer of four electrons to the catalyst. To facilitate this multi-electron transfer at low overpotential, a catalyst needs to adjust its acceptor states to the oxidation potentials of all involved intermediates. This ability requires a sufficiently complex atomic and electronic structure. Mn–O compounds represent a promising material class due to the flexible Mn valence.[31] Possible shifts in the Mn valence between 2+ and 4+ during the reaction steps may allow the catalyst to adjust the bonding characteristics between an active Mn site and oxygen intermediates.

At present, theoretical works on the catalytic activity of perovskites ($ABO_3$) are based on strong approximations, such as a frozen, defect free surface.[68,121] Those consider the bonding strength of the B-site cation to oxygen as a universal descriptor for oxygen evolution activity of perovskites. Systematic experimental studies of oxygen evolution activity of various transition metal oxide perovskites show a trend of activity with occupation of antibonding $e_g$ states of the B-site d subshell, i.e., a volcano type relation with maximum activity at an $e_g$ occupation of about one electron per B-cation.[49] However, manganites seem not to follow this dependence. The activity may strongly depend on factors such as pH value influencing the geometric and electronic structure of the catalyst surface.[73]

We present the investigation of the surface electronic structure of $Pr_{1\text{-}x}Ca_xMnO_3$ ($0 < x_{Ca} < 0.8$) by means of X-ray absorption near-edge spectroscopy (XANES) and X-ray photo-emission spectroscopy (XPS). The heterovalent Ca-doping results in a Mn valence shift with a bulk average value varying from 3.0+ ($x_{Ca} = 0.0$) to 3.8+ ($x_{Ca} = 0.8$). To what extent the average valence $Mn^{(3+x)+}$ is comprised of a mixture of $Mn^{3+}$ and $Mn^{4+}$ species, or formed by an intermediate valence state is controversially discussed in the literature.[122,123] A formation of intermediate Mn valences would be consistent with a more "covalent-like" electron density distribution within the Mn 3d–O 2p conduction band. By studying the thresholds and line shapes of the Mn L- and O K-edges, we give evidence for the presence of an intermediate Mn valence.

The central question addressed in this work is the surface electronic structure including the valence of the Mn surface sites during catalytic activity. In the presence of water vapor the surface valence may differ from the bulk value due to the bonding of various adsorbates and the formation of surface defects such as oxygen vacancies. The presented spectra have either been recorded in ultra-high vacuum (UHV), or in contact with water vapor at the crystalline catalyst surface with an applied positive electric potential, nominally corresponding to OER conditions. It is shown, that upon in situ activation of the catalyst surface $Mn^{2+}$ coexists with the mean bulk valence of $Mn^{(3+x)+}$. This is consistent with the reversible formation of surface oxygen vacancies as well as surface hydroxide adsorbates. It is furthermore shown that the virgin surface measured under UHV conditions can be restored by annealing at about 120 °C in 0.1 mbar $O_2$. The formation of surface oxygen vacancies contradicts the expectations from the oxidizing electro-chemical conditions during oxygen evolution and, thus, sheds light onto possible reaction mechanisms.

## 2.2 Results and Discussion

### 2.2.1 Doping Dependence of Virgin Samples

Mn L-edge and O K-edge spectra of the virgin samples under UHV conditions are shown in Figure 2.1. The Mn L-edge is split into two separate multiplets $L_3$ (at 642 eV) and $L_2$ (at 653 eV) due to spin-orbit interaction of the Mn $2p_{3/2}$ and $2p_{1/2}$ core states. The complex structure of these edges can be attributed to the Mn 3d states due to the octahedral ligand field including hybridization with O 2p states as well as Coulomb and exchange interactions within the 3d states.[124–126] Compared to simple Mn oxides, further complexity of the $L_3$ edge is produced by the lower local symmetry due to octahedral tilting in the orthorhombic PCMO phase.[127] Linear superposition (Figure 2.9) of the spectra at $x_{Ca} = 0$ and 0.8 resulted in poor agreement with the spectra at intermediate doping of $x_{Ca} = 0.3$ and 0.5, which indicates an intermediate valence state of $Mn^{(3+x)+}$ instead of coexisting $Mn^{3+}$ and $Mn^{4+}$ species.[128] This observation clearly supports the statement of a high covalence of the Mn-O bond.

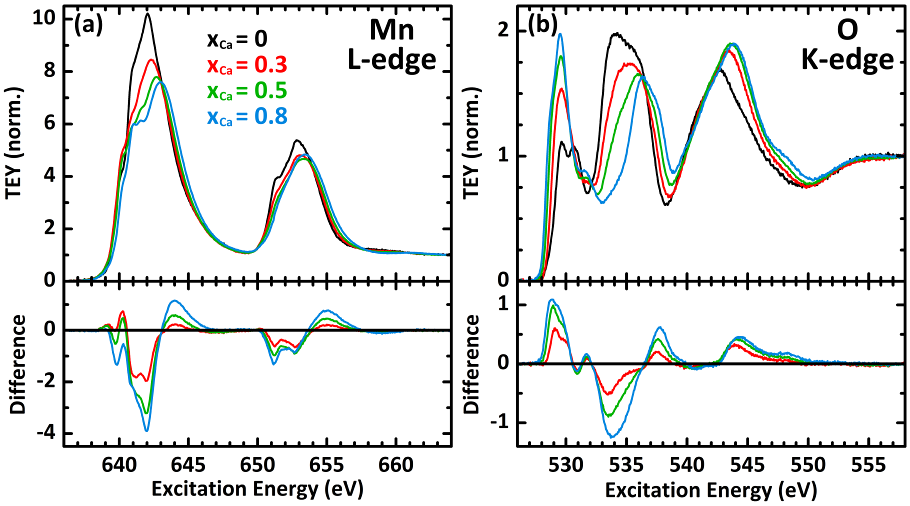

**Figure 2.1:** Normalized (see 2.3.2) X-ray absorption of virgin samples in UHV. (a) The Mn L-edge shows the systematic increase in Mn valence with increasing $x_{Ca}$; (b) Intensity of the pre-edge feature of the O K-edge (530 eV) increases with $x_{Ca}$.

The $L_3$ peak shifts to higher energies and its area decreases systematically with increasing $x_{Ca}$ and therefore increasing formal Mn valence of $(3 + x_{Ca})+$. A similar trend can be seen for the $L_2$ edge. This chemical shift is in good agreement with reported results on various manganite perovskites [129, 130] and other Mn compounds. [125] According to studies of Mn oxide compounds by means of Electron Energy Loss Spectroscopy (EELS) [131] the decreasing energetic distance $\Delta E_L$ between the maxima of the Mn $L_2$ and $L_3$ edges (Figure 2.1 a and Table 2.1) due to increasing $x_{Ca}$ corresponds to an increase in Mn valence. Despite the systematic error resulting from only taking into account the maximum position of the complex $L_3$ edge structure, our data represent a systematic valence shift as expected from sample stoichiometry (formal bulk valence from 3.0+ to 3.8+). Moreover, the integral intensity ratio of the $L_3$ and $L_2$ edges decreases systematically with increasing $x_{Ca}$ (Table 2.1, for details see 2.5.2). According to Riedl et al. [132] our data quantitatively represent the expectation of a systematic Mn valence increase between 3+ and 4+.

The pre-edge region of the O K-edge at roughly 530 eV (Figure 2.1 b) represents excitation into hybridized states containing O 2p and Mn 3d states. [133, 134] It is thus a direct expression of the degree of covalence of the Mn-O bond near the Fermi level. Our results show splitting of the pre-edge feature for the undoped $PrMnO_3$ (formal Mn valence of 3+), which can be explained by ligand field interaction and high-spin Hund's coupling resulting in O 2p states hybridized with majority spin Mn $e_g$ states

**Table 2.1:** Mn valence indicators obtained from the Mn L- and O K-edge spectra of virgin samples under ultra-high vacuum (UHV) conditions. The energetic distance between the Mn $L_3$ and $L_2$ edges ($\Delta E_L$), their intensity ratio ($I_3/I_2$) after subtraction of a constant $L_2$ background (BG1) or linear backgrounds for each edge (BG2, see 2.5.2) as well as the distance between the pre-edge feature and the first main resonance of the O K-edge ($\Delta E_K$) are summarized.

| $x_{Ca}$ | formal bulk valence | $\Delta E_L$ (eV) | $I_3/I_2$ (BG1) | $I_3/I_2$ (BG2) | $\Delta E_K$ (eV) |
|---|---|---|---|---|---|
| 0 | 3.0+ | 10.8 | 2.89 | 2.54 | 3.8 |
| 0.3 | 3.3+ | 10.8 | 2.88 | 2.53 | 5.8 |
| 0.5 | 3.5+ | 10.6 | 2.85 | 2.46 | 6.3 |
| 0.8 | 3.8+ | 10.4 | 2.75 | 2.32 | 6.8 |

at 529.6 eV and with minority spin Mn $t_{2g}$ states at 530.8 eV.[58][i] Heterovalent Ca-doping leads to a decreased Mn 3d occupation, which is reflected by the systematic intensity increase at the low energy flank of the pre-edge region. Furthermore, the first main resonance, which results from excitation into hybridized states containing Pr 5d and Ca 3d contributions,[135] shifts from 534 eV ($x_{Ca} = 0$) to 536.4 eV ($x_{Ca} = 0.8$), which is in good agreement with data reported on various Sr- and Ca-doped rare-earth manganites.[127,129] These trends can be expressed as an increasing energetic distance $\Delta E_K$ between the pre-edge feature and the first main resonance (Table 2.1), which reflects the effects of the hole doping.[132]

### 2.2.2 In Situ Investigation

In previous work, oxygen evolution at $Pr_{1-x}Ca_xMnO_3$ has been detected in two electrode configurations at sample bias above +1.6 V. These experiments have been performed in liquid water by differential electrochemical mass spectrometry (DEMS) and by mass spectrometry in environmental transmission electron microscopy (ETEM) in water vapor.[73] We here present in situ studies of the same catalyst in 0.1 mbar $H_2O$ at sample bias of +2.5 V, where oxygen evolution is expected.

Figure 2.2 presents the change of the Mn L-edge during catalyst activation. In contact with the water vapor an increase in $L_3$ and $L_2$ intensity was observed. To analyze the changes in the Mn valence states, the difference spectra between the UHV virgin spectra and the spectra in water vapor at positive bias have been generated and are shown as filled green curves. With peaks at 640.2, 641.6, and 643.9 eV, they bear a resemblance to a pure $Mn^{2+}$ spectrum, as will be shown in the following section.

---

[i] In the original publication, this has been cited as unpublished work, but is now available under the given reference.

After heating the samples for 10 min to about 120 °C in 0.1 mbar $O_2$ the post reaction analysis was done under UHV conditions. For $x_{Ca} = 0.3$ and 0.5 the original surface oxidation state was entirely restored, while minor changes remain for $x_{Ca} = 0$ and 0.8 (filled blue curves).

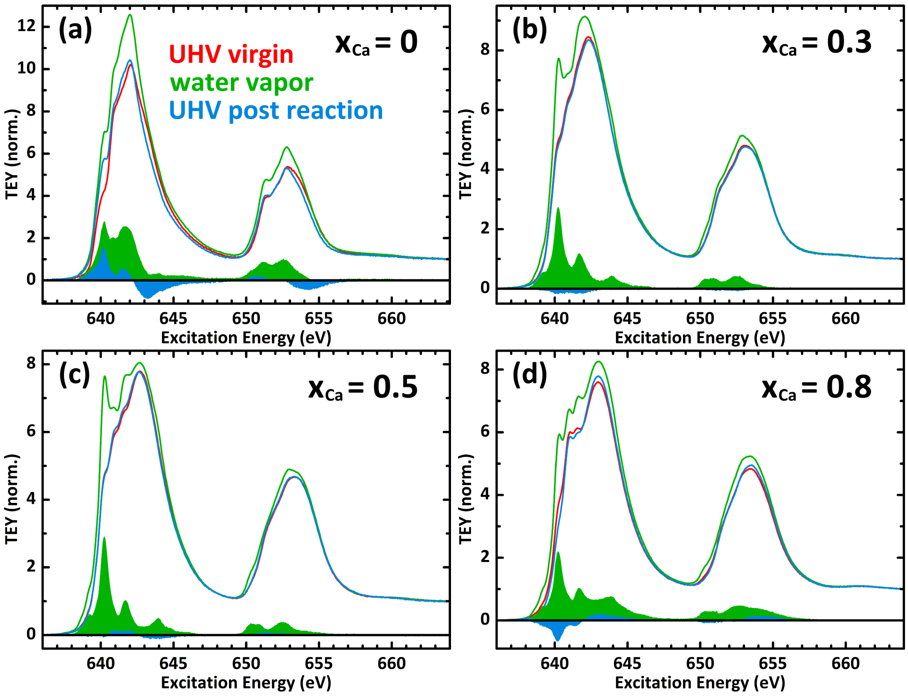

**Figure 2.2:** Normalized Mn L-edge spectra (Total Electron Yield) before (red) and during insertion of 0.1 mbar $H_2O$ with sample bias of +2.5 V against chamber ground (green), as well as in UHV after reoxidation in 0.1 mbar $O_2$ (blue). Samples with $x_{Ca} = 0$ (a), $x_{Ca} = 0.3$ (b), $x_{Ca} = 0.5$ (c), and $x_{Ca} = 0.8$ (d). Filled curves represent the change from virgin to activated (green) and from virgin to post reaction (blue).

In order to get insight into the changes of the catalyst surface upon contact with liquid water with respect to the effects of water vapor, we compare in Figure 2.3 the Mn L-edges of a virgin sample at $x_{Ca} = 0.8$ with a sample which has been pretreated in liquid water without bias application. After keeping the sample in distilled water at room temperature for 60 min, it was directly dried and transferred into the UHV chamber. The pretreatment results in formation of some $Mn^{2+}$ species in addition to the bulk $Mn^{3.8+}$. We observe a slight general decrease of the intensity to background ratio, which may be due to surface adsorbates such as hydroxides.

This pretreated sample has then been investigated by the same in situ procedure as the virgin samples, which is shown in Figure 2.3 b. The arising $Mn^{2+}$ spectrum in response to water vapor under positive bias is more pronounced than the one of the virgin sample (Figure 2.2 d), with its two main peaks at 640.2 and 641.6 eV dominating the $L_3$ edge. After heating the sample for 10 min in 0.1 mbar $O_2$ and returning to UHV the post reaction analysis shows the recovery of the pretreated state.

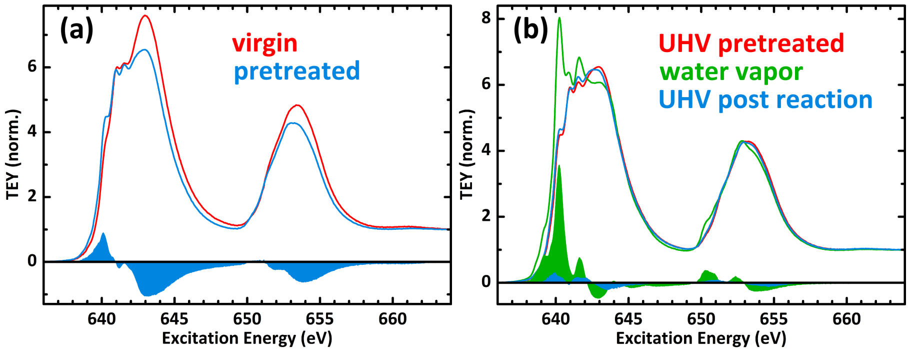

**Figure 2.3:** Normalized Mn L-edge of pretreated sample ($x_{Ca} = 0.8$). (a) Comparison to virgin sample with $x_{Ca} = 0.8$ in UHV; (b) Pretreated state in UHV (red), in 0.1 mbar $H_2O$ at a bias of +2.5 V against chamber ground (green), and post reaction in UHV (blue).

### 2.2.3 Mn Surface Species

Except for a small additional feature at 639 eV, the difference spectra of the Mn $L_3$ edge between virgin and activated state (filled green curves in Figure 2.2) correspond to a pure $Mn^{2+}$ spectrum (Figure 2.4), showing good agreement with calculated spectra based on atomic multiplet theory in a cubic crystal field [124] as well as with spectra measured at Mn(II)$O_x$ nanoparticles [136], commercial Mn(II)$SO_4$ [125], Mn(II)$CO_3$ [137, 138], Mn(II)O [139], and complex Mn(II) compounds [140].

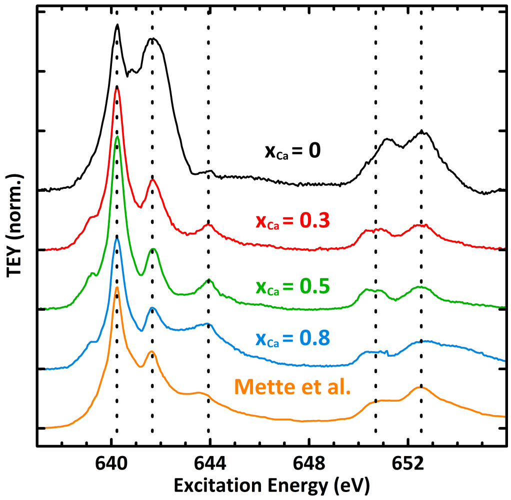

**Figure 2.4:** Difference spectra at Mn L-edge between in situ activated and virgin state compared with $Mn^{2+}$ spectrum taken from Mette et al. [136]

The information depth of XANES TEY spectra is determined by the escape depth of the photoelectrons, which are composed of electrons of quite different energies, namely primary photoelectrons, Auger electrons and secondary electrons. Contributions of the different types of emitted electrons depend on the material, the photon energy and the electron energy dependent transmission function of the detector. Exact values are presently not known. According to a study by Frazer et al.[94] on the escape depth of electrons through a Cr layer ($Z_{Cr} = 24$ compares to the average $Z = 21.5$ of $PrMnO_3$) we expect that 50 % of the signal originates from the topmost 0.6 nm (O K-edge) and 0.7 nm (Mn L-edge) and 99.9 % from the first 6 nm (O K-edge) and 7 nm (Mn L-edge), respectively.

The high reversibility after removing the water vapor by heating samples in oxygen and the nm range information depth of the TEY spectra suggest that the formation of $Mn^{2+}$ species results from surface and/or subsurface O vacancy formation during oxygen evolution.[138] At first sight this fundamentally contradicts the expectations from a "frozen surface - no surface defects" picture, since the Mn valence should increase under the nominally oxidizing conditions with an applied sample bias of +2.5 V vs. the grounded chamber. Under such conditions, no overall reduction via pure vacancy formation should take place in the catalyst. Our observations thus indicate that surface oxygen vacancies are directly involved in the reaction mechanism during water oxidation. In such a scenario, the (sub)surface oxygen may represent an exchange site for oxygen based intermediates, which is affected by the state of neighboring Mn sites. Alternatively, a Mn valence decrease may be induced by surface adsorbates such as $OH^-$ and $OOH^-$, which exhibit a lower formal valence compared to $O^{2-}$. However, the integral $L_3$ intensity increase due to $Mn^{2+}$ formation of 8.5 % to 13.9 % is quite strong considering the information depth of the order of several nm. We therefore conclude that the changes are not mainly due to surface adsorbates, but rather to formation of surface-near oxygen vacancies. The corresponding redox process is visible in cyclic voltammetry as a reversible surface process centered at $U_0 \approx +1$ V vs. SHE (see 2.3.1). It can be interpreted according to:

$$2\,Pr^{3+}_{1-x}\,Ca^{2+}_{x}\,Mn^{(3+x)+}\,O^{2-}_{3} + 2\,e^{-} \Leftrightarrow 2\,Pr^{3+}_{1-x}\,Ca^{2+}_{x}\,Mn^{(3+x)+}_{1-y}\,Mn^{2+}_{y}\,O^{2-}_{2.5} + V^{''}_{O} + \tfrac{1}{2}\,O_2. \quad (2.1)$$

Although the chemical equilibrium at reduced oxygen partial pressure is generally shifted towards oxygen vacancy formation, our finding that reoxidation by healing of vacancies can take place at a similar partial pressure (0.1 mbar $O_2$) as their formation seems to exclude this effect as the main driving force. We rather assume that surface oxygen formation is a non-equilibrium property of the active catalyst during OER.

This assumption is supported by the observed doping dependence of the $Mn^{2+}$ formation. Our in situ results show that the accordance of the differential spectra with the pure $Mn^{2+}$ reference is best for intermediate doping of $x_{Ca} = 0.3$ and 0.5, while only minor deviations are observed for $x_{Ca} = 0.8$, namely an increased intensity around the 644 eV peak of the $L_3$ edge and at the high energy tail of the $L_2$ edge (Figure 2.4). Additionally, the changes of integral intensity (from 630 to 665 eV) due to $Mn^{2+}$ formation are relatively small for $x_{Ca} = 0.3$ (+8.7 %) and 0.5 (+8.5 %) compared to the values at $x_{Ca} = 0$ (+13.9 %) and 0.8 (+10.6 %) (Figure 2.2). Finally, samples at $x_{Ca} = 0.3$ and 0.5 show a higher reversibility in UHV post reaction analysis. These findings thus indicate a higher (electro) chemical stability at intermediate $x_{Ca}$, which is in contrast to the monotonic decrease of the formation energy of manganite perovskites from the metal elements and $O_2$ with increasing Ca-doping. [121] The hereby observed maximum stability at intermediate $x_{Ca}$ is in good agreement with environmental transmission electron microscopy results comparing low/intermediate $x_{Ca}$ to high Ca-doping [73], as well as stability analysis in the whole doping range by ex situ cyclic voltammetry (see supplementary information in [73]).

In contrast to oxygen evolution in water vapor, the pretreatment of the catalyst in liquid water may facilitate the formation of an A-cation deficient surface layer, i.e., the irreversible dissolution of $Ca^{2+}$. Evidence for the irreversibility of the pretreatment is given by post reaction reoxidation in $O_2$ atmosphere, which results in restoration of the pretreated instead of the virgin state (Figure 2.3 b, blue curve). In addition to $Ca^{2+}$ dissolution, formation of O vacancies and interstitial hydrogen can take place to some extent in the absence of external bias. Our data, thus, suggest that these processes overcompensate the effect of the oxidative $Ca^{2+}$ dissolution. We cannot entirely exclude that also diffusion of vacancies or hydrogen into deeper subsurface regions during liquid water exposure contribute to the changes in the pretreated sample.

### 2.2.4 XPS

Due to in situ activation in water vapor intense additional peaks emerge in the X-ray photoelectron spectra of the Ca $2p_{3/2}$ and Ca $2p_{1/2}$ states respectively (347.5 and 351 eV), as well as of the O 1s states (532 eV) shown for the sample at $x_{Ca} = 0.5$ in Figure 2.5 a and b. According to studies on $La_{0.6}Ca_{0.4}CoO_3$ [141, 142], the changed structure of the Ca 2p spectra is consistent with the formation of surficial $Ca(OH)_2$ and CaO species. The broad additional O 1s peak indicates the formation of various weakly bound O- species on the surface including hydroxide adsorbates and point defects in the perovskite lattice. This has been found by studies on $La_{1-x}Sr_xMnO_3$ [143], $La_{0.6}Ca_{0.4}CoO_3$ [141], $La_{1-x}Ce_xMnO_3$ [144], $La_{1-x}Ca_xMnO_3$ [145], $CaO/Ca(OH)_2$ [146] and $LaMO_3$ (M = Rh, Ni, Co, Fe, Mn, Cr) [147]. For a more detailed peak analysis see 2.5.3.

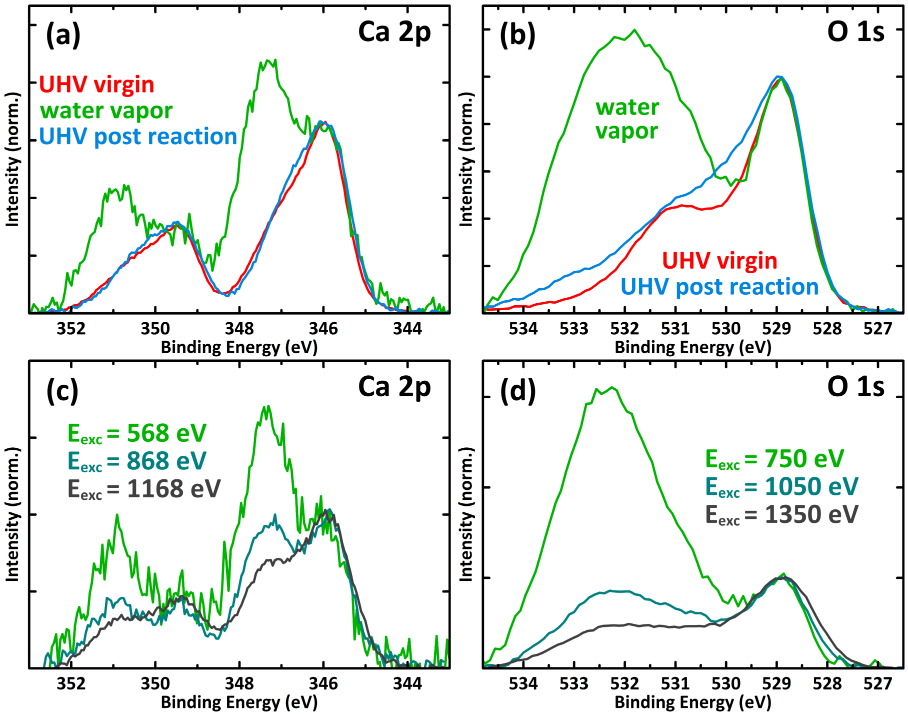

**Figure 2.5:** X-ray photoemission spectra of a PCMO film with $x_{Ca} = 0.5$. (a) Ca 2p states before (red) and during insertion of 0.1 mbar $H_2O$ with sample bias of +2.5 V against chamber ground (green), as well as in UHV after reoxidation in 0.1 mbar $O_2$ (blue); (b) O 1s states; (c) Depth profiling of Ca 2p states in active catalyst, ranging from 1 nm ($E_{exc} = 568$ eV) to 1.5 nm ($E_{exc} = 1168$ eV); (d) Depth profiling of O 1s states with the same information depths.

The spectra presented in Figure 2.5 a, b have been recorded at photon energies of 568 and 750 eV respectively, resulting in kinetic energies of the photoelectrons of about 220 eV. This corresponds to an information depth of roughly 1 nm. [148] To investigate the nature of the additional Ca and O species due to in situ activation the excitation energies were increased by 300 and 600 eV. Increasing the kinetic energy of the photoelectrons to 820 eV results in an information depth of about 1.5 nm. The decreasing intensity of the active species with increasing photon energy (Figure 2.5 c, d) thus indicates near surface changes.

## 2.3 Experimental Section

### 2.3.1 Sample Preparation and Characterization

$Pr_{1-x}Ca_xMnO_3$ (PCMO) thin films at doping levels of $x_{Ca} = 0$, 0.3, 0.5 and 0.8 have been deposited by reactive ion beam sputtering from stoichiometric targets. The Xe working gas partial pressure amounted to $1 \times 10^{-4}$ mbar and the $O_2$ partial pressure was $1.4 \times 10^{-4}$ mbar. The films have a thickness of about 300 nm and have been deposited on 200 nm Pt layers, which provide the electric back contact. These Pt films have previously been deposited on commercial MgO (001) single crystal substrates.

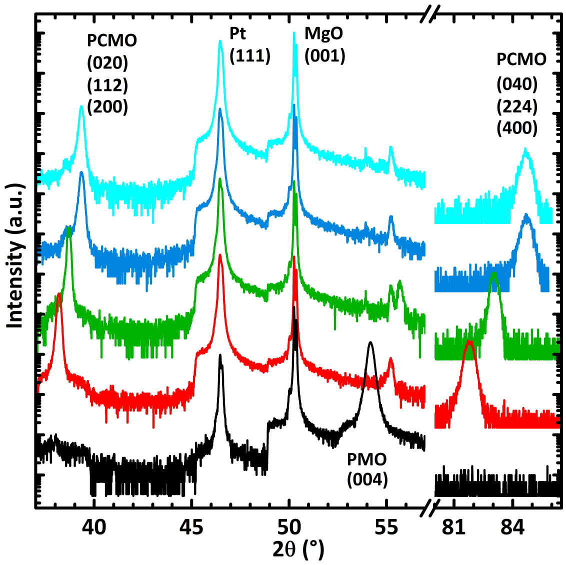

**Figure 2.6:** XRD scans in Θ-2Θ geometry. The intense substrate peaks correspond to Pt (111) and MgO (001). $PrMnO_3$ (black) exhibits a (001)/(110) twin structure, while samples with $x_{Ca} = 0.3$ (red) and 0.5 (green), as well as the two samples with $x_{Ca} = 0.8$ (blue and cyan) show a (100)/(010)/(112) texture.

The films have been characterized by means of X-ray diffraction (XRD) in Θ-2Θ geometry using an X'Pert MRD diffractometer (Philips B.V., Almelo, Netherlands) with Co Kα radiation from a tube operated at 40 kV and 30 mA. Figure 2.6summarizes the XRD results of the five investigated samples. Note that the spectra of two different samples at $x_{Ca} = 0.8$ are shown in Figure 2.6; the sample shown in cyan was used for pretreatment in liquid water. The two intense peaks at 46.5° and 50.3° can be attributed to the Pt (111) layer and the MgO (001) substrate respectively. The $PrMnO_3$ film (black curve) shows a (001) orientation with (110) twins, represented by the broadened peak at 54.2°. The Ca-doped samples (colored curves) exhibit two peaks at 38.2° − 39.4° and 81.8° − 84.7° respectively, revealing a texture containing (100), (010), and (112) orientations, which cannot be further distinguished due to overlap of the (200), (020) and (112) peaks. The systematic shift of these two peaks to higher angles with increasing $x_{Ca}$ represents the reduction in lattice parameter due to different octahedral tilts and Mn-O bonding length.[57] For the sample with $x_{Ca} = 0.5$ (green curve) (001) misorientations (<33 vol-%) are observed, represented by the (004) peak at 55.7°. Additional small peaks from 53° to 56° result from artifacts due to other X-ray wavelengths.

The surface morphology has been investigated by scanning electron microscopy (SEM) using a LEO Supra 35 (Carl Zeiss NTS GmbH, Oberkochen, Germany). A representative SEM image for each doping level $x_{Ca}$ is shown in Figure 2.7, revealing compact films. The sample with $x_{Ca} = 0$ exhibits a rod-like surface morphology due to the (110) twins (Figure 2.7 a), while the samples with $x_{Ca} = 0.3$ and 0.5 show a plate-like morphology (Figure 2.7 b, c) which most probably corresponds to the [100]/[010] orientations. The sample with $x_{Ca} = 0.8$ shows a morphology of higher complexity which may indicate a non-unique in-plane epitaxy (Figure 2.7 d). Additionally, it is revealed that the sample surfaces with $x_{Ca} = 0.3$ and 0.5 contain $MnO_x$ precipitates, which however cover only < 2 % of the surface.

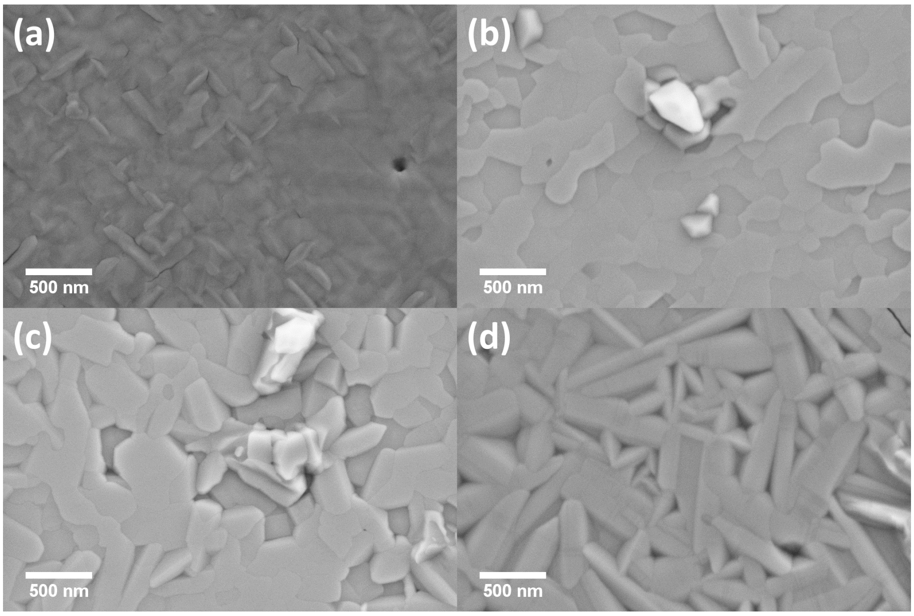

**Figure 2.7:** SEM images of samples with $x_{Ca} = 0$ (a), 0.3 (b), 0.5 (c), and 0.8 (d) after XANES/XPS investigation. Shown is the secondary electron contrast.

The catalytic activity for oxygen evolution from water splitting has been investigated at comparable samples with $x_{Ca} = 0.3$ by cyclic voltammetry (CV). Figure 2.8 shows

CV curves measured at a PCMO thin film at sweep rates of 2.5, 5, and 10 mV/s. A Pt counter electrode and commercial Ag/AgCl reference electrode have been used in aqueous 0.1 m $Na_2SO_4$ (pH 7). In addition to oxygen evolution above +1.2 V vs. SHE a reversible surface redox process is observed, which is centered at $E_0 \approx +1$ V vs. SHE. A more detailed CV investigation of different PCMO stoichiometries has been published elsewhere[73], where this process has been interpreted as oxygen vacancy formation according to Equation (2.1). No changes in surface morphology have been observed by post reaction SEM investigation.

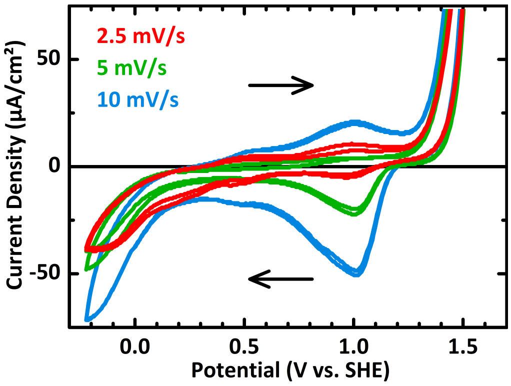

**Figure 2.8:** CV curves of a PCMO sample with $x_{Ca} = 0.3$ showing oxygen evolution above +1.2 V vs. SHE and a reversible redox process centered at +1.0 V vs. SHE (pH 7).

### 2.3.2 In Situ XANES/XPS Measurements

X-ray absorption near edge spectroscopy (XANES) as well as X-ray photoemission spectroscopy (XPS) of various edges and states has been performed at the BESSY II synchrotron facility of the Helmholtz-Zentrum Berlin, Germany (HZB), using the near ambient-pressure XPS endstation of the Fritz-Haber-Institut of the Max-Planck-Gesellschaft (FHI-MPG) at the ISISS beamline. The instrumental setup by Knop-Gericke and co-workers is described in detail elsewhere.[96]

For XANES at the Mn L-edge the excitation energy was swept from 630 to 665 eV, while the O K-edge was measured from 520 to 565 eV. The scan rate was 0.5 eV/s in continuous driving mode of the plane-grating monochromator. The fixed-focus constant was set to $c_{ff} = 2.25$ and the exit slit to 60 µm [37].[149] The presented spectra have been measured in total electron yield mode (TEY). Energy shifts have been corrected on the basis of the simultaneously measured characteristic absorption spectrum of a focusing mirror. Intensities have been normalized with respect to impinging photon flux. A linear background was subtracted and the spectra were intensity normalized to unity at 664 eV for the Mn L-edge and at 558 eV for the O K-edge to account for the increased signal in water vapor due to inelastic scattering of photoelectrons with gas molecules.

For collecting the photoemission spectra the monochromator was set to $c_{ff} = 2.25$ with an exit slit of 111 µm. Emission from the Ca 2p states has been recorded at an excitation energy of 568 eV, while emission from the O 1s states has been recorded at an excitation energy of 750 eV. For depth profiling each of the excitation energies was increased by 300 and 600 eV respectively. The step size was 50 meV for Ca 2p and 100 meV for O 1s spectra. All spectra were collected using a pass energy of 20 eV and a dwell time of 100 ms. Spectra have been intensity normalized with respect to impinging photon flux. A linear as well as a Shirley-type background were subtracted.[150] To account for loss of total signal intensity during water vapor exposure compared to UHV measurements due to inelastic scattering of photoelectrons at gas molecules, the spectra were then normalized with respect to the intensity of the bulk-like peaks of the Ca $2p_{3/2}$ states at 346 eV or the O 1s states at 529 eV respectively. These bulk-like peaks have also been used for energy alignment, e.g., for subtraction of sample bias.

Experiments have been conducted in ultra-high vacuum (UHV) and in 0.1 mbar $H_2O$ vapor with an applied sample bias of +2.5 V between the sample back contact and the chamber (ground). All measurements have been performed at room temperature. Before returning to UHV conditions the samples were heated to approximately 120 °C for 10 min and cooled for another 10 min in 0.1 mbar $O_2$ to remove accumulated surface carbon and to reestablish a fully oxygenized sample surface.

## 2.4 Conclusions

$Pr_{1-x}Ca_xMnO_3$ thin films in the doping range between $x_{Ca} = 0$ and 0.8 have been studied with respect to electro-catalytic oxygen evolution. It is found that the doping dependent Mn valence cannot be described by a mixture of $Mn^{3+}$ and $Mn^{4+}$ species but rather by an intermediate $Mn^{(3+x)+}$ state. This finding corroborates the picture of covalent-like contributions to the charge distribution in the antibonding Mn 3d $e_g$-O 2p states, which are relevant for electron transfer from oxygen-based species to Mn sites during water oxidation. In situ studies under nominally oxidizing conditions for oxygen evolution reveal the coexistence of a $Mn^{2+}$ surface species with the bulk Mn valence state. It is shown that the surface activation involves the reversible formation of surface oxygen vacancies. The observed changes are fully reversible with respect to annealing in $O_2$ atmosphere at 120°C.

We conclude that the Mn valence shift is mainly due to surface oxygen vacancy formation, which are formed by the reaction steps during water oxidation despite of the nominally oxidizing conditions. We propose that such oxygen vacancies are part of the active catalyst structure and are involved as a docking site for water molecules and reaction intermediates.

Since the occupation of antibonding $e_g$ states is changed in operation, the application of a rigid molecular orbital filling model to describe catalytic activity as a function of bulk bonding strength seems to be very limited. The bulk occupation of these states, which can be controlled by heterovalent doping, can be strongly modified at the activated surface.

## Acknowledgments

The Helmholtz-Zentrum Berlin (HZB) is acknowledged for the allocation of synchrotron measurement time. We are grateful to Helge Stein who supported the XANES and XPS measurements. Financial support by the Deutsche Forschungsgemeinschaft through the CRC 1073 project C02 is gratefully acknowledged. We thank Robert Schlögl for fruitful discussions.

## 2.5 Appendix

### 2.5.1 Linear Superposition of Experimental Mn L-Edges

To deal with the question whether the average Mn valence is comprised of a mixture of $Mn^{3+}$ and $Mn^{4+}$ species or formed by an intermediate valence state of $Mn^{(3+x)+}$, we compared stoichiometric linear superposition of Mn L-edges at high and low $x_{Ca}$ to measured spectra at intermediate $x_{Ca}$. As shown in Figure 2.9, the stoichiometric superpositions (blue curves) show significant systematic deviations from the corresponding measurements. Variations can be compared by the difference spectra which are shown as filled blue curves. They exhibit a minimum at 640.2 eV as well as two maxima at 641.0 and 642.0 eV respectively. According to Kanamori et al.[128] the bad compliance indicates an intermediate valence state instead of coexisting species. This result indicates significant covalent contributions to the Mn-O bond, i.e. a charge density distribution at the upper valence band edge which is more or less centered at the Mn-O bond instead of forming $Mn^{3+}/Mn^{4+}$ species.

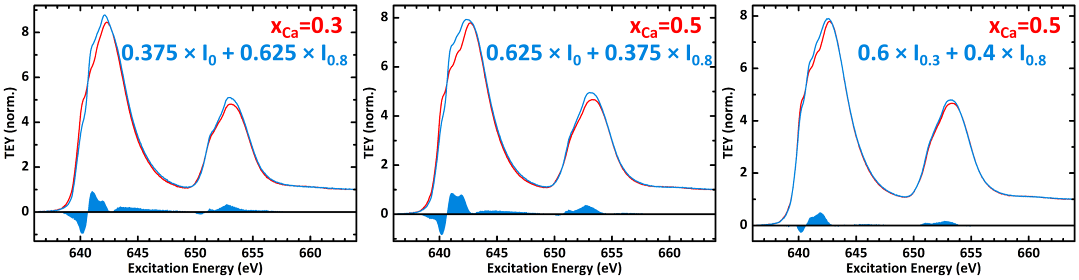

**Figure 2.9:** Comparison of linear superpostition of Mn L-edges at high and low $x_{Ca}$ to spectra at intermediate $x_{Ca}$. The superpositions (blue) are assembled according to the expected nominal concentrations of the $Mn^{3+}$ and $Mn^{4+}$ species as indicated by the formulas in blue color.

## 2.5.2 Intensity Ratio of the Mn $L_{3,2}$-Edges

For Electron Energy Loss Spectroscopy (EELS) in transmission electron microscopy (TEM) of white lines like the Mn L-edge a Hartree-Slater-type background model has been established.[131] Since the physical processes in TEY-XANES experiments are quite different, we used a constant as well as a linear background model for quantification of the integral Mn $L_{3,2}$ edge intensities of the virgin samples. The backgrounds are illustrated in Figure 2.10. A constant $L_2$ background (BG1) was used from 649.3 to 658.0 eV, while two linear backgrounds (BG2) were used from 637.3 to 649.3 eV and from 649.3 to 658.0 eV respectively.

## 2.5.3 XPS

Spin-orbit interaction splits the Ca 2p states into $2p_{1/2}$ and $2p_{3/2}$ substates at binding energies of roughly 350 and 346 eV respectively. The structure of the virgin perovskite lattice at $x_{Ca} = 0.5$ shown in Figure 2.11 a reveals further splitting into a total of four peaks labeled $P_1$ and $P_2$ for the $2p_{3/2}$ as well as $P_3$ and $P_4$ for the $2p_{1/2}$ states. $P_2$ and $P_4$ represent surface sites exhibiting less chemical shift compared to the $P_1$ and $P_3$ subsurface sites. Upon in situ activation in 0.1 mbar water vapor at a sample bias

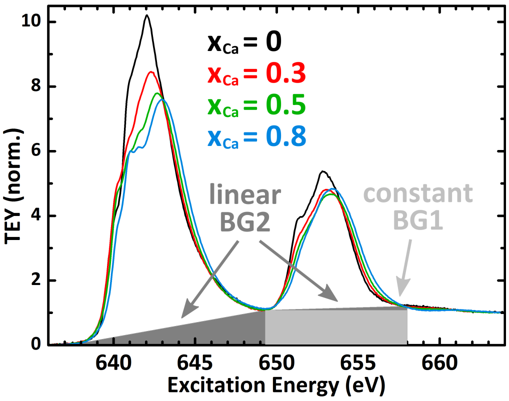

**Figure 2.10:** Simple background models used for quantification of Mn $L_{3,2}$ intensities.

of +2.5 V against the grounded chamber our data show the emergence of a second Ca species represented by the peaks labeled $A_1$ and $A_2$. According to studies on $La_{0.6}Ca_{0.4}CoO_3$ [141, 142] this could correspond to formation of surficial $Ca(OH)_2$ and CaO. Reoxidation in 0.1 mbar $O_2$ fully restores the virgin state of the surface (blue curves in Figure 2.11 a).

The four peaks of the O 1s states are shown in Figure 2.11 b. The $O^{2-}$ species of the perovskite lattice is represented by peak $P_1$ (subsurface) and $P_2$ (surface). $P_3$ corresponds to various weakly bound $O^-$ and $OH^-$ surface species, while $P_4$ represents adsorbed $H_2O$ molecules. Upon in situ activation $P_3$ and $P_4$ increase significantly. Reoxidation of the sample leaves a slightly increased intensity of $P_2$ and $P_4$ compared to the virgin surface.

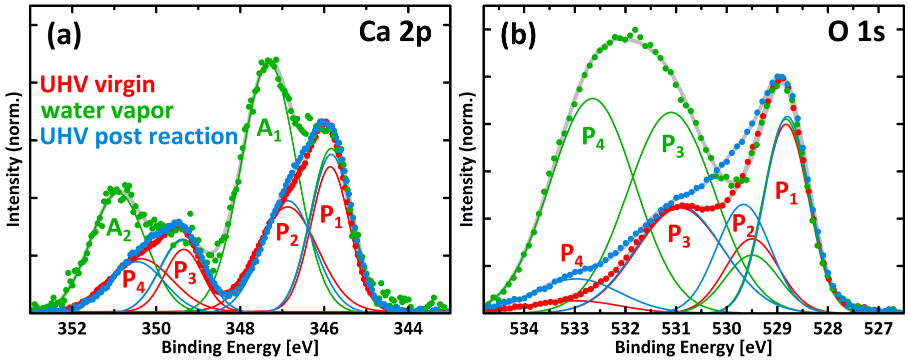

**Figure 2.11:** Peak analysis of XPS data before (red) and during insertion of 0.1 mbar $H_2O$ with sample bias of +2.5 V against grounded chamber (green), as well as in UHV after reoxidation in 0.1 mbar $O_2$ (blue). (a) Ca 2p states; (b) O 1s states.

# Chapter 3

# Environmental TEM Investigation of Electrochemical Stability

This chapter is a reproduction of the following original publication:

### Environmental TEM Investigation of Electrochemical Stability of Perovskite and Ruddlesden-Popper Type Manganite Oxygen Evolution Catalysts

***Daniel Mierwaldt***, *Vladimir Roddatis*, *Marcel Risch*, *Julius Scholz*, *Janis Geppert*, *Majid Ebrahimizadeh Abrishami*, *and Christian Jooss*

*Adv. Sustainable Syst.* **2017**, *1*(11), 1700109; doi: 10.1002/adsu.201700109

References, labels and arrangement of figures and tables have been modified to suit this thesis. Videos are accessible on the journal's website.

**Abstract** The sluggish kinetics of the oxygen evolution reaction (OER) are a grand challenge for energy storage technologies. Several perovskites and other oxides of earth-abundant elements have been found to exhibit improved catalytic OER activity. However, less attention has been paid to the electrochemical stability, an important factor for large-scale application. The ongoing search for stable catalysts calls for characterizing active catalyst surfaces and identifying mechanisms of deactivation, activation or repair. In situ techniques are indispensable for these tasks. This study

uses environmental TEM (ETEM) on the highly correlated perovskite $Pr_{1\text{-}x}Ca_xMnO_3$ and the Ruddlesden-Popper $Pr_{0.5}Ca_{1.5}MnO_4$ as model electrodes to elucidate the underlying mechanisms of the stability trends identified on rotating ring disk electrodes (RRDE). An electron beam at fluxes well below radiation damage is used to induce positive local electrode potentials due to secondary electron emission, driving electrochemical reactions in $H_2O$ vapor. Stability of the model systems increases with increasingly ionic character of the Mn-O bond, while more covalent bonds are prone to corrosion, which is triggered by formation of point defects in the oxygen sublattice.

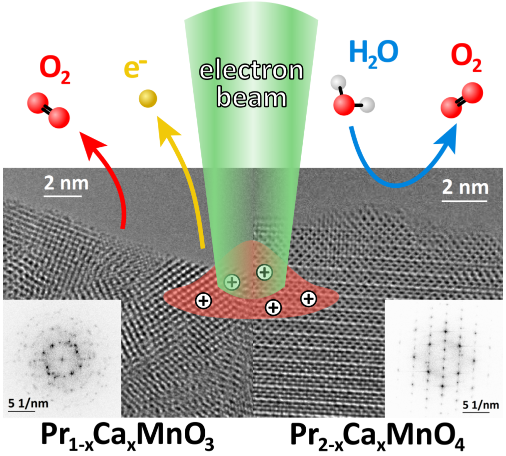

## 3.1 Introduction

Electro-chemical water splitting is a critical step of sustainable production of artificial fuels from renewable energies. Its efficiency is limited by large overpotentials of the anodic oxygen evolution reaction (OER). [2,3,50,62–65] Next to scarce noble metal oxides, several first-row transition metal oxides and, in particular, perovskite-based systems with the general formula $ABO_3$ perform well as OER catalysts. [3,27,50–52] Theoretical studies suggest that the catalytic activity of the four-electron transfer reaction forming molecular $O_2$ depends on strength and flexibility of the bond between active site and reaction intermediates [68,70] as well as on facile electron transfer. [151] In perovskites, bond strength and electron transfer are influenced by the transition metal valence as well as by distance, angle and hybridization of the metal oxygen bonds. These parameters can be tuned by heterovalent A-site doping. [54,55] The required flexibility to adjust the surface acceptor states to the various reaction intermediates is facilitated by the capability of some transition metals to form different valence states. [68,152] Specifically, valence states of Mn-based OER catalysts are found to be between 3+ and 4+, as in the $Mn_4Ca$ complex in natural photosynthesis. [64,153–158]

Searching for correlations between bond parameters and OER activity of perovskites, Suntivich et al. observed a volcano-like relationship between OER activity and bulk occupation of the σ-antibonding $e_g$ states. [49] However, active surfaces can differ significantly from the equilibrium bulk states of a catalyst, involving dynamic point defect formation and annihilation, as e.g. observed in $TiO_2$ or predicted for Au nanoparticles.[159,160] Point defect dynamics such as vacancies and interstitial atoms also have a strong impact on reaction mechanisms and activity in perovskites.[74,75] Furthermore, the reversibility of such point defect dynamics governs catalyst stability. The importance of understanding active states is underlined by the finding that high intrinsic activity is often correlated with low thermodynamic stability leading to corrosion and therefore limited long-term usability.[77–80]

Two principal scenarios for active sites and underlying reaction mechanisms are discussed for perovskite oxides, namely redox active metal versus redox active lattice oxygen sites. In the case of active metal sites, theory suggests that all OER steps occur at single metal centers.[68] Such a mechanism is supported by recent experiments on $La_{0.6}Sr_{0.4}MnO_3$ (LSMO), where a correlation between OER activity and Mn surface concentration is observed.[161,162] On the other hand, it has been proposed that surface lattice oxygen can be involved in OER by protonation (OH) and vacancy formation ($V_O$), based on in situ experiments[73,74] and recent theoretical works.[76,80] Note that previous studies have also shown lattice oxygen involvement for several highly active rutile catalysts.[83–85] Theoretical and experimental works suggest that lattice oxygen involvement is provoked by strong hybridization of the metal-oxygen bond, which can shift the redox activity from metal to lattice oxygen surface sites due to ligand hole formation.[3,73,77,81,82] Thus, an understanding of the underlying microscopic mechanisms, the nature of active sites and catalyst stability is necessary to rationalize the search for active and stable catalysts.

Using in situ X-ray absorption near-edge spectroscopy (XANES) and environmental transmission electron microscopy (ETEM) on the perovskite $Pr_{1-x}Ca_xMnO_3$ ($x \geq 0.3$), which has strong hybridization between O 2p and Mn 3d states, we have found strong evidence for lattice oxygen involvement in OER.[73,74,105] This was concluded from the experimentally observed Mn reduction at the surface under strongly oxidizing conditions, which can be explained by the formation of $V_O$ and surface protonation acting as electron donors to Mn. This scenario was proven by the observation of vacancy ordering, showing that redox activity of lattice oxygen can open up a corrosion channel.[105] $V_O$ formation during OER is facilitated by increasing Ca concentration and was interpreted by an increasing contribution of O 2p holes at the upper valence band edge based on band structure calculations. A comparative study of the perovskite (P) manganite $Pr_{1-x}Ca_xMnO_3$ and the related Ruddlesden-Popper (RP) system $Pr_{1-x}Ca_{1+x}MnO_4$ at equal doping levels of $x_{Ca} = 0.5, 0.75$ and 1 shows much higher stability of the RP structure, which was interpreted by a reduced O 2p character of the acceptor states, i.e. lower covalence factor, measured by X-ray spectroscopy at the O K-edge.[157] Different OER mechanisms, employing either O or Mn as redox active sites, therefore seem to enable different possible corrosion pathways and thus lead to remarkable differences in the stability of Mn-based electrodes.

We here present an ETEM study on the interplay of point defect chemistry and corrosion pathways, combined with ex situ rotating ring disk electrochemistry (RRDE). We compare the electrochemical stability of the perovskite $Pr_{0.7}Ca_{0.3}MnO_3$ (P73-PCMO) and the Ca-rich, layered RP system $Pr_{0.5}Ca_{1.5}MnO_4$ (RP-PCMO) in $H_2O$ vapor at a fixed pressure of 0.5 Pa. The chosen model systems are comprised of the same building blocks, namely $MnO_6$ octahedra, which provide the hybridized, redox active electronic states and similar Mn valence.[58] The systems have been chosen because of strong differences in covalence.[157] Moreover, RP systems show a much higher oxygen mobility parallel to the layers compared to perovskites and its change of lattice parameter as a function of oxygen content is one order of magnitude smaller, leading to reduced vacancy induced strain.[163,164] Differences in both properties are presumably important for explaining the observed enhanced stability of the RP phase under reactive conditions compared to the P phase. The ETEM study is extended to non-OER conditions in $O_2$ and/or He. To verify the stabilizing effect of lower covalence, the perovskite $Pr_{0.9}Ca_{0.1}MnO_3$ (P91-PCMO) with lower covalence factor than P73-PCMO is included in the ETEM study.

## 3.2 Results

### 3.2.1 Ex Situ Characterization

#### 3.2.1.1 Electrochemistry by RRDE

Catalytic properties of P73-PCMO and RP-PCMO for OER are investigated by means of rotating ring disk electrodes (RRDE). The powders are deposited onto glassy carbon to form disk electrodes. A systematic study of structural and electrochemical properties including further doping levels of the two systems has been published elsewhere.[157]

The oxygen evolution activity is demonstrated by cyclic voltammetry (CV) in Ar-saturated electrolyte (0.1 M KOH) of the disk electrode and using the Pt ring electrode for detecting evolved oxygen molecules at a constant potential of 0.4 V vs. RHE via the oxygen reduction reaction. Representative CV curves of disk and ring current densities in Figure 3.1 a-b show a comparably higher activity of the RP-PCMO both in terms of overpotential to obtain a current density of 50 µA/cm$^2$ and in terms of current density at a potential of 1.65 V vs. RHE. We observe slightly lower Tafel slopes for the P73-PCMO electrode. The same observations are made in $O_2$-saturated electrolyte, as summarized in Table 3.1. Ring currents are not superimposed by corrosion or capacitance, and correspond solely to the reduction of evolved oxygen.[161] Therefore, the simultaneous increase, i.e. similar Tafel slopes, of disk and ring currents suggests that the observed onset in fact corresponds to OER.[165]

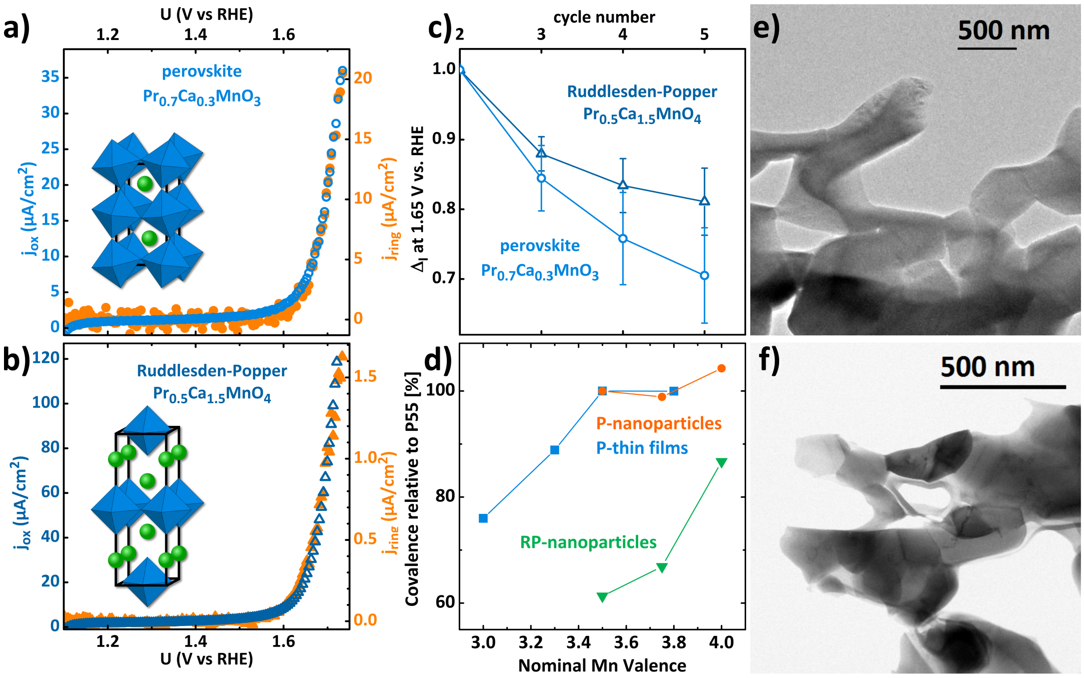

**Figure 3.1:** a)-b) Representative CV measurements (forward direction of the 5th scan) of powders of P73-PCMO (a) and RP-PCMO (b) are shown in blue and the corresponding ring currents in orange. The voltage is corrected for electrolyte resistance. Ring currents were obtained by CA at 0.4 V vs. RHE. c) Relative changes of current density at 1.65 V vs. RHE compared to the 2nd scan. All measurements were performed with 10 mV/s scan rate at 1600 rpm rotation in Ar-purged (a-b) or $O_2$-purged (c) 0.1 M KOH supporting electrolyte. d) Covalence of the Mn-O bond in $Pr_{1-x}Ca_xMnO_3$ perovskite (P) thin films (squares), P-particles (circles) and Ruddlesden-Popper (RP) particles (triangles). e)-f) Low magnification brightfield TEM images of the ion milled P73-PCMO (e) and RP-PCMO (f).

To evaluate the electrochemical stability of P73-PCMO and RP-PCMO, we compare the changes of consecutive voltage cycles relative to the 2nd cycle at a potential of 1.65 V vs. RHE. These relative changes are presented in Figure 3.1 c, showing significantly higher stability of the RP-PCMO. Note that the intermediate potential range

**Table 3.1:** The electrochemical parameters are based on CV measurements in $O_2$- or Ar-saturated 0.1 M KOH and the error represents the averaged values of three electrodes of the respective composition. Tafel slopes were calculated from the capacitance corrected 5th scan.

| material | electrolyte | U (50 µA / cm$^2$) [V vs. RHE] | $j_{oxide}$ (1.65 V vs. RHE) [µA / cm$^2$] | Tafel slope (CV) [mV / dec.] |
|---|---|---|---|---|
| P73-PCMO | $O_2$ | $1.72 \pm 0.01$ | $3.4 \pm 0.5$ | $78 \pm 3$ |
|  | Ar | n.a. | $5.6 \pm 1.2$ | $97 \pm 4$ |
| RP-PCMO | $O_2$ | $1.69 \pm 0.01$ | $21.0 \pm 5.6$ | $93 \pm 4$ |
|  | Ar | $1.68 \pm 0.01$ | $22.4 \pm 0.9$ | $97 \pm 2$ |

is chosen to avoid contribution of capacitive effects at low potential and bubble formation at high potentials.

#### 3.2.1.2 Covalence Analysis by XAS

X-ray absorption spectroscopy (XAS) at the O K-edge is very sensitive to the character of the iono-covalent Mn-O bond. As described in the SI, differences of the bond covalence can be qualitatively extracted from intensity differences of the low energy feature, reflecting the presence of O 2p hole states due to hybridization with the Mn 3d states.[133,157,166] X-ray absorption edges (total electron yield) of different P- and RP-PCMO samples at various Pr/Ca ratios are presented in Figure 3.2. The obtained covalence factors are plotted against the corresponding nominal Mn valence in Figure 3.1 d. To compare the results of thin films and submicrometer-sized particles, the factors are normalized by the respective values for P55-PCMO. Covalence is found to be highest in Ca-doped P-PCMO, decreasing towards $PrMnO_3$ below half doping. In comparison, covalence is significantly lower in RP-PCMO, showing strong decrease with increasing Pr/Ca-ratio also for Ca-rich compositions.

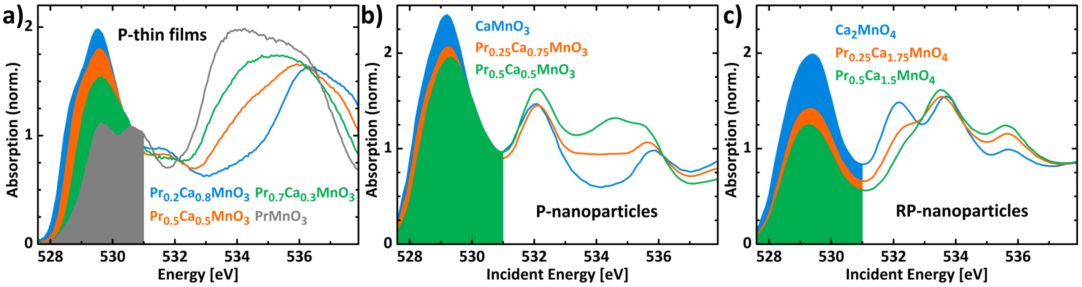

**Figure 3.2:** X-ray absorption (O K-edge, TEY) of P-PCMO thin films (a) and nanoparticles (b), as well as RP-PCMO nanoparticles (c). Intensities below 531 eV are highlighted by filled curves.

Therefore, ex situ experiments demonstrate the correlation of electrochemical stability with the iono-covalent character of the Mn-O bonds. However, understanding the mechanistic origin of corrosion pathways requires in situ studies, as presented in the following section.

### 3.2.2 ETEM Experiments

Microscopic investigation of the catalyst surfaces under reactive conditions is performed in an ETEM. Representative low magnification bright field TEM images of the ion milled specimen from sintered powder pellets are shown in Figure 3.1 e (P73-PCMO) and Figure 3.1 f (RP-PCMO). Crystal sizes of 80 to 800 nm are observed. We expose the catalysts to $H_2O$ vapor at 0.5 Pa and to different pressures of $O_2$ or He. Unless specified otherwise, an electron beam of 4 nA and 100 nm diameter is used to stimulate and observe the specimen, corresponding to an electron flux density of about 32,000 $e^{-}Å^{-2}s^{-1}$. At this rather high value, no structural changes due to beam damage are observed by high-resolution transmission electron microscopy (HRTEM) imaging in high vacuum and inert gas (He) during exposure for typically 50 min. Absence of oxygen knock-out from intact crystalline areas in high vacuum mode is proven by EELS analysis of Mn valence. In $H_2O$ vapor, the electron flux has been found to be optimal in order to induce electrochemical activity.[88]

#### 3.2.2.1 ETEM Analysis of P73-PCMO

The ETEM experiment presented in Figure 3.3 demonstrates the beam driven formation of nanocrystals from the oxygen depleted amorphous surface and the underlying (001) facet of a P73-PCMO single crystal (orthorhombic Pbnm space group) in 0.5 Pa $H_2O$. The cross-section lamella is cut from an epitaxial thin film (section 3.5.1). An amorphous layer of 2-5 nm thickness due to ion milling and carbon contamination is observed on the pristine surface. (Figure 3.3 a) The contamination is being removed upon exposure to the beam in vacuum of $10^{-4}$ Pa, while the ion beam damaged specimen material remains stable. (Figure 3.3 b, Video 1) Exposure to the same electron beam in 0.5 Pa $H_2O$ leads to rapid recrystallization of surface-near areas. (Video 2) The state of the specimen after 8 minutes of in situ recrystallization with ca. 5 nm large crystallites on the surface is shown in Figure 3.3 c.

Next, we present an ETEM experiment on a single crystalline (010) facet of a P73-PCMO particle. The pristine composition is confirmed by electron energy loss spectroscopy (EELS) and energy dispersive X-ray spectroscopy (EDX), as summarized in

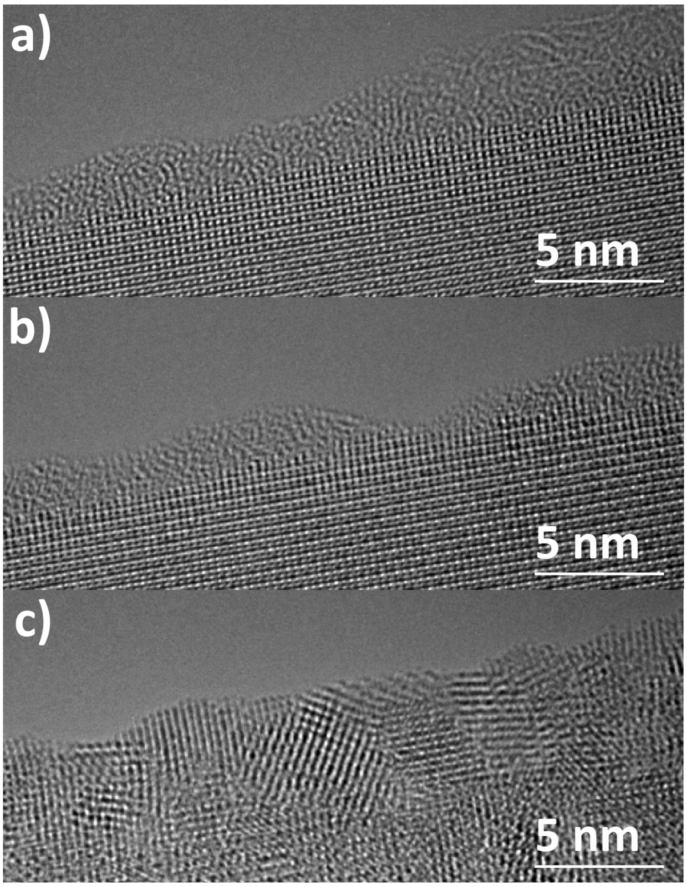

**Figure 3.3:** a) Epitaxial P73-PCMO thin film with amorphous surface layer due to specimen preparation by ion milling and carbon contamination. b) Remaining preparation induced layer, after slow removal of carbon contamination under electron beam illumination in high vacuum ($10^{-4}$ Pa). c) In 0.5 Pa $H_2O$, ca. 5 nm large crystallites start to form in random orientation on top of the single crystal surface.

Table 3.2 and described in section 3.6.2. Figure 3.4 a shows a high-resolution image of the pristine surface and Video 3 demonstrates its stability under illumination by the electron beam in vacuum of $8{\cdot}10^{-5}$ Pa. $H_2O$ vapor is introduced and a pressure of 0.5 Pa is stabilized with blanked beam for about 45 minutes. Upon exposure to the beam under these conditions, nanocrystals of various orientations start to form at the particle surface (Figure 3.4 b and Video 4). Corresponding fast Fourier transforms (FFTs) of the indicated areas are shown in Figure 3.4 c and 3.4 d. The FFT of an exemplary area marked by the blue square is still clearly dominated by the original perovskite structure (Figure 3.4 c), demonstrating that it is preserved in the bulk. The FFT of the surface crystal (Figure 3.4 d) is consistent with the perovskite structure in new orientation with deviations from the pristine lattice parameters within 10 pm and also contains weak spots originating from the bulk.

Post-mortem scanning transmission electron microscopy (STEM) and EELS analysis reveals that the experiment in $H_2O$ ultimately leads to chemical decomposition of the P73-PCMO. In order to minimize further beam-induced reactions, post-mortem analysis is performed after several hours of pumping the $H_2O$ out of the microscope returning to a vacuum of ca. $10^{-4}$ Pa. The high-angle annular dark field (HAADF) images of the reacted specimen in Figure 3.4 e and 3.5 show brightness variations between approximately 5-10 nm large areas, resulting from variations in thickness and chemical composition. Since the scattering angle is limited to 100 mrad, the HAADF signal also contains some coherent contrast from different orientations of surface crystals. EEL spectra from areas A-D (Figure 3.4 e) as well as from larger areas E-H (Figure 3.6) show varying ratios of the contained cations, as summarized in Table 3.3. Details of the quantification procedure are given in sections 3.6.2-3.6.3. Major loss of Mn is revealed in areas where the specimen has been illuminated under reactive conditions, as indicated by a strongly increased A-cation to Mn ratio compared to its stoichiometric value. Depletion of Mn increases with decreasing specimen thickness, indicating that surface reactions drive the perovskite nanocrystal formation as well as the subsequent decomposition of the perovskite into Pr-rich and Ca-rich phases. In areas G and H, which have not been exposed to the electron beam during the in situ experiment, almost no change in chemical composition is observed. In conclusion, P73-PCMO recrystallizes and subsequently decomposes whenever it is exposed to the combination of $H_2O$ and electron beam at the chosen parameters.

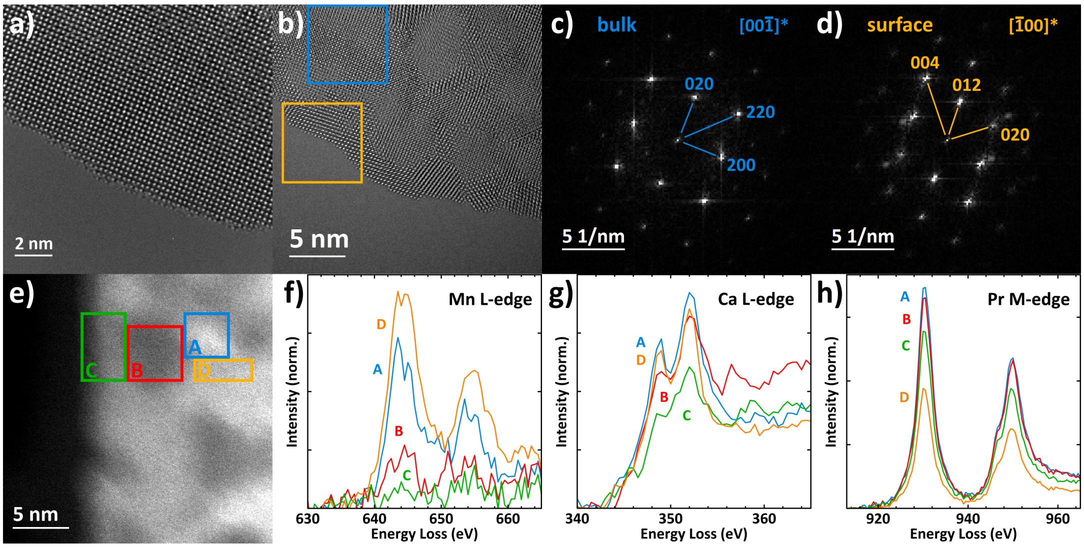

**Figure 3.4:** a) Pristine P73-PCMO (010) facet of a single crystal particle in <001> zone axis. b)-d) Beam driven nucleation of misoriented perovskite nanocrystals at the surface, observed after 3 min of illumination in 0.5 Pa $H_2O$. FFTs show that the original crystal structure still dominates the bulk (c), while misoriented grains form at the surface (d). e) Post-mortem HAADF-STEM shows brightness variations between 5-10 nm large areas, partly due to thickness variation as well as chemical decomposition. f)-h) Post-mortem EEL spectra of areas A-D marked in (e) at the Ca L-, Mn L-, and Pr M-edges demonstrate chemical decomposition due to structural disorder.

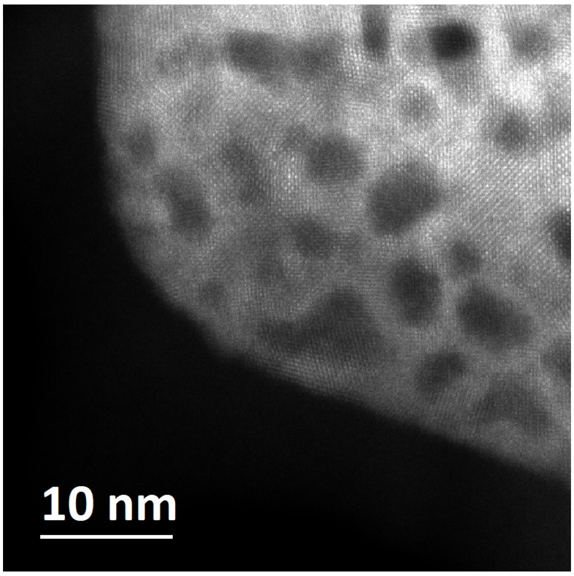

**Figure 3.5:** Post mortem HAADF-STEM overview of the reacted P73-PCMO nanoparticle.

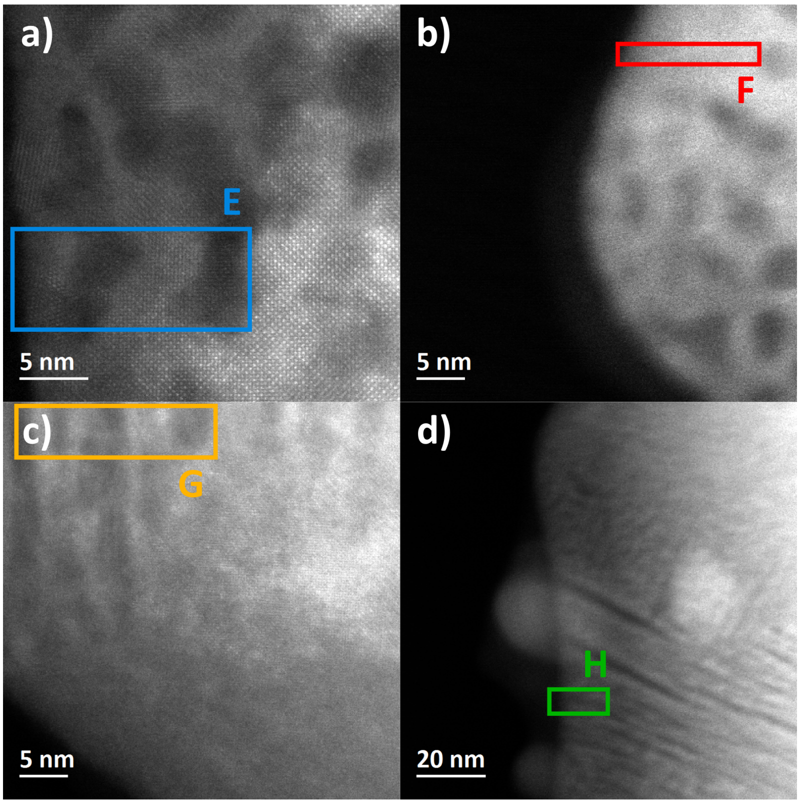

**Figure 3.6:** Post mortem HAADF-STEM images of the reacted P73-PCMO nanoparticle. Colored boxes mark the areas where EEL spectra were recorded (Table 3.3). Areas E (a) and F (b) show chemical decomposition due to structural disorder from the in situ experiment under e-beam, while the nominal composition is preserved without in situ illumination in areas G (c) and H (d).

**Table 3.2:** Chemical composition of the pristine P73-PCMO particles. Quantification of the Pr M-, Ca L-, and Mn L-edges from EELS and of the Pr L-, Ca K-, and Mn K-lines from EDX.

| **spectrum** | **$t/\lambda$** | **Pr [at-%]** | **Ca [at-%]** | **Mn [at-%]** | **(Pr + Ca) / Mn** | **Ca / (Pr + Ca)** |
|---|---|---|---|---|---|---|
| nominal composition | | 35 | 15 | 50 | 1.00 | 0.30 |
| EELS 1 | 0.40 | 34.0 | 15.8 | 50.2 | 0.99 | 0.32 |
| EELS 2 | 0.40 | 29.7 | 16.2 | 54.2 | 0.85 | 0.35 |
| EELS 3 | 0.40 | 37.5 | 14.5 | 48.0 | 1.09 | 0.28 |
| EELS 4 | 0.36 | 35.0 | 17.1 | 47.9 | 1.09 | 0.33 |
| EELS 5 | 0.51 | 38.7 | 16.3 | 45.0 | 1.22 | 0.30 |
| EELS 6 | 0.35 | 37.3 | 15.3 | 47.4 | 1.11 | 0.29 |
| EELS 7 | 0.36 | 38.3 | 15.6 | 46.2 | 1.17 | 0.29 |
| EELS average | 0.40(5) | 36(3) | 16(1) | 48(3) | 1.1(1) | 0.31(3) |
| EDX 1 | | 34.3 | 14.6 | 51.0 | 0.96 | 0.30 |
| EDX 2 | | 37.5 | 14.9 | 47.6 | 1.10 | 0.28 |
| EDX 3 | | 37.9 | 15.7 | 46.4 | 1.16 | 0.29 |
| EDX 4 | | 38.5 | 15.3 | 46.3 | 1.16 | 0.28 |
| EDX 5 | | 39.2 | 14.1 | 46.7 | 1.14 | 0.26 |
| EDX 6 | | 34.6 | 14.7 | 50.7 | 0.97 | 0.30 |
| EDX 7 | | 37.8 | 16.0 | 46.2 | 1.17 | 0.30 |
| EDX 8 | | 38.0 | 15.5 | 46.6 | 1.15 | 0.29 |
| EDX 9 | | 38.2 | 15.9 | 45.9 | 1.18 | 0.29 |
| EDX 10 | | 38.4 | 15.8 | 45.8 | 1.18 | 0.29 |
| EDX 11 | | 38.8 | 15.5 | 45.7 | 1.19 | 0.29 |
| EDX 12 | | 37.0 | 16.5 | 46.4 | 1.15 | 0.31 |
| EDX average | | 38(2) | 15(1) | 47(2) | 1.1(1) | 0.29(1) |

**Table 3.3:** Post-mortem EELS analysis of the P73-PCMO particle. Concentrations of Pr, Ca, and Mn atoms (in atomic %) are quantified by using the Pr M-, Ca L-, and Mn L-edges as described in section 3.6.3. Total relative thickness ($t_{tot}/\lambda$) has been calculated from simultaneously measured low loss spectra. It has been corrected for carbon contribution from surface contamination to give the specimen specific $t/\lambda$. HAADF images of the measured areas are shown in Figure 3.4 e (areas A-D) and Figure 3.6 (areas E-H). Areas G and H were not illuminated by the electron beam during the in situ experiment and are close to the pristine composition.

| **area** | **$t/\lambda$** | **Pr [at-%]** | **Ca [at-%]** | **Mn [at-%]** | **(Pr + Ca) / Mn** | **Ca / (Pr + Ca)** |
|---|---|---|---|---|---|---|
| nominal composition | | 35.0 | 15.0 | 50.0 | 1.0 | 0.30 |
| pristine crystal | | 37.0 | 15.5 | 47.5 | 1.1 | 0.30 |
| A | 0.09 | 62.3 | 25.9 | 11.9 | 7.4 | 0.29 |
| B | 0.06 | 53.5 | 38.9 | 7.6 | 12.2 | 0.42 |
| C | 0.06 | 59.0 | 37.2 | 3.9 | 24.9 | 0.39 |
| D | 0.10 | 45.6 | 28.3 | 26.1 | 2.8 | 0.38 |
| E | 0.07 | 58.8 | 21.6 | 19.7 | 4.1 | 0.27 |
| F | 0.21 | 54.3 | 18.6 | 27.2 | 2.7 | 0.25 |
| G (no beam) | 0.37 | 36.5 | 12.4 | 51.1 | 1.0 | 0.25 |
| H (no beam) | 0.17 | 31.1 | 17.7 | 51.2 | 1.0 | 0.36 |

#### 3.2.2.2 ETEM Analysis of P91-PCMO

A fundamentally higher stability of P91-PCMO compared to P-PCMO with higher Ca-content is observed in the ETEM under the same experimental conditions at 0.5 Pa $H_2O$. Figure 3.7 shows the single crystalline (112) facet of a particle in $<$110$>$ zone axis of the Pbnm structure during the experiment. The specimen keeps its single crystalline state over the entire course of the experiment, despite showing strong cationic dynamics in the uppermost atomic layer. As further discussed for experiments on RP-PCMO and in section 3.6.5, the very weak contrast of the light oxygen atoms confines our observations to movement of the cations.

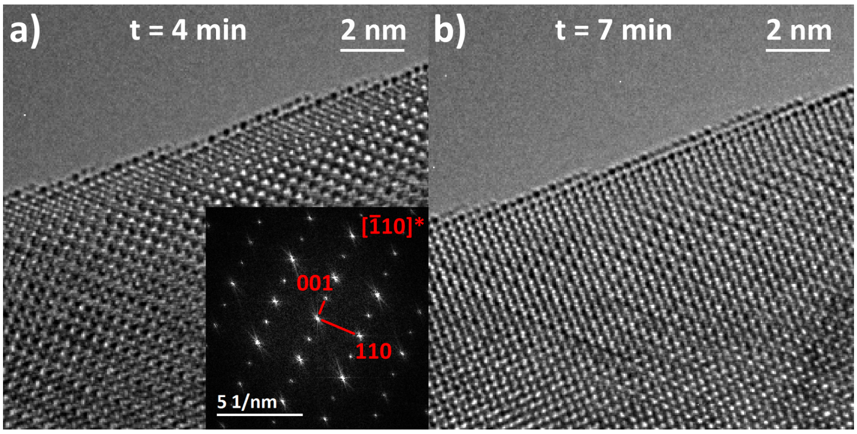

**Figure 3.7:** P91-PCMO single crystal observed at $<$110$>$ zone axis after 4 min (a) and 7 min (b) of the ETEM experiment in 0.5 Pa $H_2O$. The FFT is shown as an inset.

#### 3.2.2.3 ETEM Analysis of RP-PCMO

RP-PCMO particles are exposed to $H_2O$ vapor at 0.5 Pa. The example in Figure 3.8 shows such a particle in $<$110$>$ projection with a curved edge close to a (001) facet (orthorhombic Fmm2 space group) with an amorphous surface layer due to lamella preparation. The pristine composition is confirmed by EELS and EDX, as summarized in Table 3.4 and described in section 3.6.2. Upon exposure to the beam in $H_2O$, the up to 3 nm thick surface layer starts to crystallize mostly epitaxially on top of the Ruddlesden-Popper particle. (Video 5) Some amorphous material is still left on the surface after 7 minutes of illumination in $H_2O$. (Figure 3.8 a) Note that the area of the low indexed (001) surface facet (marked by arrows) acts as the most stable substrate leading to faster (and epitaxial) growth compared to edges, corners, and higher indexed surfaces. After 11 minutes, most of the surface material is crystallized and some misoriented grains start to grow. (Figure 3.8 b) After another 13 minutes, the misoriented grains have grown. (Figure 3.8 c) FFTs of the 550 nm$^2$ large areas at the observed surface after 7 and 24 minutes are shown in Figure 3.8 d and 3.8 e respectively. The single crystal peaks of the RP-PCMO clearly dominate both FFTs, demonstrating its high structural stability. As can be seen in Video 5, the nanocrystals are mostly formed from the initially amorphous surface layer. This is in contrast to P73-PCMO, where nanocrystals are formed from bulk material.

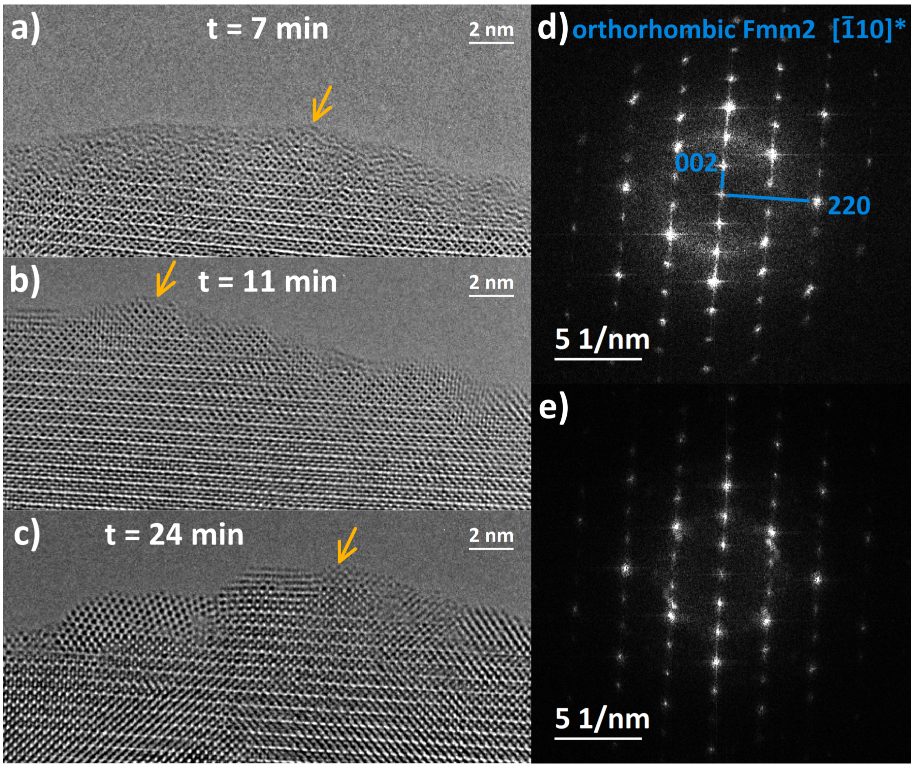

**Figure 3.8:** a)-c) RP-PCMO single crystalline particle with a near (001) facet observed in <110> zone axis after 7, 11, and 24 minutes of the in situ experiment in 0.5 Pa $H_2O$. The preparation induced amorphous surface layer (a) begins to crystallize epitaxially on top of the RP-PCMO (b). After more than 20 minutes, crystals of random orientation start to form at curved and higher indexed surfaces, while the epitaxy appears stronger on the flat (001) surface as marked by the arrow (c). d)-e) FFTs of 550 nm$^2$ large areas after 7 (d) and 24 (e) minutes demonstrate the stability of the bulk structure during the entire time.

**Table 3.4:** Chemical composition of the pristine RP-PCMO. Quantification of the Pr M-, Ca L-, and Mn L-edges from EELS and of the Pr L-, Ca K-, and Mn K-lines from EDX. The quantification procedure is the same as described for pristine P73-PCMO in section 3.6.2.

| spectrum | $t/\lambda$ | Pr [at-%] | Ca [at-%] | Mn [at-%] | (Pr + Ca) / Mn | Ca / (Pr + Ca) |
|---|---|---|---|---|---|---|
| nominal composition | | 16.67 | 50.00 | 33.33 | 2.00 | 0.75 |
| EELS 1 | 0.20 | 15.1 | 48.1 | 36.7 | 1.72 | 0.76 |
| EELS 2 | 0.22 | 14.9 | 48.2 | 36.9 | 1.71 | 0.76 |
| EELS 3 | 0.45 | 20.7 | 43.5 | 35.8 | 1.80 | 0.68 |
| EELS 4 | 0.86 | 17.8 | 48.2 | 34.0 | 1.94 | 0.73 |
| EELS 5 | 0.53 | 15.7 | 50.8 | 33.5 | 1.98 | 0.76 |
| EELS 6 | 0.30 | 14.3 | 50.4 | 35.3 | 1.83 | 0.78 |
| EELS average | 0.4(3) | 16(3) | 48(3) | 35(1) | 1.8(1) | 0.75(4) |
| EDX 1 | | 14.8 | 55.2 | 30.0 | 2.33 | 0.79 |
| EDX 2 | | 15.6 | 54.1 | 30.3 | 2.30 | 0.78 |
| EDX 3 | | 14.4 | 53.7 | 31.8 | 2.14 | 0.79 |
| EDX 4 | | 14.8 | 55.2 | 30.0 | 2.33 | 0.79 |
| EDX 5 | | 15.3 | 52.6 | 32.1 | 2.12 | 0.77 |
| EDX 6 | | 15.3 | 52.9 | 31.8 | 2.15 | 0.78 |
| EDX 7 | | 15.4 | 53.4 | 31.2 | 2.20 | 0.78 |
| EDX 8 | | 15.3 | 52.0 | 32.7 | 2.06 | 0.77 |
| EDX 9 | | 14.9 | 49.5 | 35.6 | 1.81 | 0.77 |
| EDX 10 | | 14.2 | 50.5 | 35.3 | 1.84 | 0.78 |
| EDX 11 | | 14.4 | 50.1 | 35.5 | 1.82 | 0.78 |
| EDX 12 | | 14.2 | 51.1 | 34.7 | 1.89 | 0.78 |
| EDX 13 | | 14.4 | 50.5 | 35.1 | 1.85 | 0.78 |
| EDX average | | 15(1) | 52(2) | 33(2) | 2.1(2) | 0.78(1) |

### 3.2.2.4 EELS Analysis of RP- and P73-PCMO

A deeper understanding of the electrochemical processes underlying the different stability of RP- and P73-PCMO is gained from the study of changes in the Mn oxidation state via EELS. A RP-PCMO particle is investigated under the same conditions of 0.5 Pa of $H_2O$ by means of in situ EELS at the O K-edge and Mn L-edge. (Figure 3.9 a-b) HAADF-STEM images of the ca. 20 x 40 $nm^2$ large areas are shown in Figure 3.10. The low energy feature of the O K-edge at around 529 eV represents excitation into hybridized antibonding states of Mn 3d $e_g$ character.[58] It is therefore highly sensitive to changes in Mn valence state and hybridization of the Mn-O bond.[157, 166] The shift of the onset towards lower energy demonstrates oxidation of the Mn during the in situ experiment. The post-mortem valence is slightly lower, but still above the value of the pristine specimen. A similar shift of the edge onset to lower energy is found post-mortem in a nearby area, which has not been illuminated while in contact with the $H_2O$. The Mn L-edge shows the same general trend with the highest valence state during the in situ experiment in $H_2O$ vapor, as shown by the lowest intensity of the low energy flank of the $L_3$-edge at around 640 eV. The lowest valence is found in the initial state. The same edge shape is found post-mortem in the area, which has not been illuminated during the experiment. Quantification of the Mn valence is given in Table 3.5. Details on calibration and normalization of the spectra are presented in section 3.6.4.

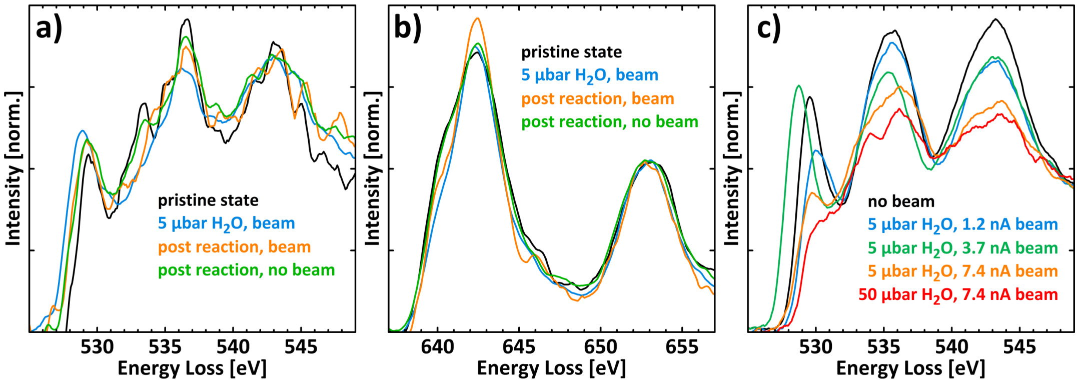

**Figure 3.9:** a)-b) EELS at the Mn L- and O K-edge of a pristine single crystalline RP-PCMO particle observed in <110> zone axis (black), in 0.5 Pa $H_2O$ (blue), and in high vacuum (HV) after the experiment of the same area (orange) and an area, which had not been illuminated by the beam during the in situ experiment (green). c) Post-mortem EELS at O K-edge of 5 areas of a P73-PCMO thin film after exposure to $H_2O$ vapor. The areas have been illuminated by 1.2 nA for 12 min (blue), 3.7 nA for 8 min (green), and 7.4 nA for 13 min (orange) in 0.5 Pa $H_2O$ as well as by 7.4 nA for 8 min in 5 Pa $H_2O$ (red). A spectrum from an unilluminated area is shown in black.

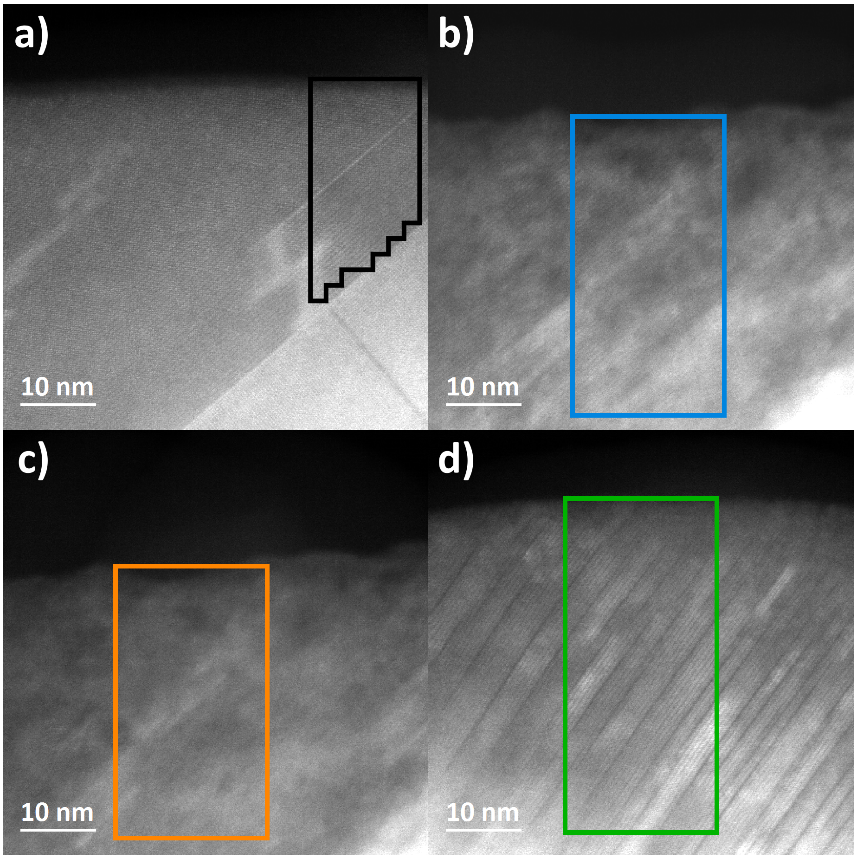

**Figure 3.10:** HAADF-STEM images of the areas, in which the EEL spectra in Figure 3.9 a-b were collected. a) before the experiment, b) in 0.5 Pa $H_2O$, c) in UHV after the experiment, d) an area in UHV, which had not been illuminated during the in situ experiment and showing a high density of stacking faults.

**Table 3.5:** Calculated Mn oxidation state from the EEL spectra in Figure 3.9 b.

| spectrum | Mn valence |
|---|---|
| initial state | 3.26 |
| 0.5 Pa $H_2O$ | 3.46 |
| post reaction | 3.30 |
| porst reaction, no beam | 3.43 |

Corrosion of P73-PCMO via nanocrystal formation and subsequent chemical decomposition is analyzed by post-mortem EELS at the O K-edge after exposure to $H_2O$ vapor at 0.5 or 5 Pa. The cross-section lamella, cut from an epitaxial thin film, is stimulated by a beam of 145 nm diameter and 1.2, 3.7 or 7.4 nA (flux densities of 4,500 - 28,000 $e^{-}Å^{-2}s^{-1}$). After 12 min at 1.2 nA in 0.5 Pa $H_2O$, some fcc nanocrystals are formed from the amorphous surface material, as demonstrated by the rotationally averaged FFT of a 16 x 16 $nm^2$ area at the edge (Figure 3.11), while the Pbnm single crystal clearly dominates the FFT of a 32 x 32 $nm^2$ area. (Figure 3.12 a-b) The reduced intensity of the low-energy feature of the O K-edge (528-530 eV) from the entire illuminated area of 16,500 $nm^2$ shows reduction of the P73-PCMO in comparison to an area that has not been illuminated during the ETEM experiment. (Figure 3.9 c) Higher beam current or $H_2O$ pressure strongly accelerate the formation and growth of nanocrystals from the surface and bulk material, which is demonstrated by increasing number and intensity of polycrystalline peaks and decreasing intensity of the Pbnm single crystal peaks. (Figure 3.12 c-h) As a result, the P73-PCMO increasingly decomposes into fcc nanocrystals (Figure 3.11), which can lead to both oxidized or reduced Mn species. (Figure 3.9 c) In summary, we observe electronic changes of both the corroding P73-PCMO as well as the stable RP-PCMO.

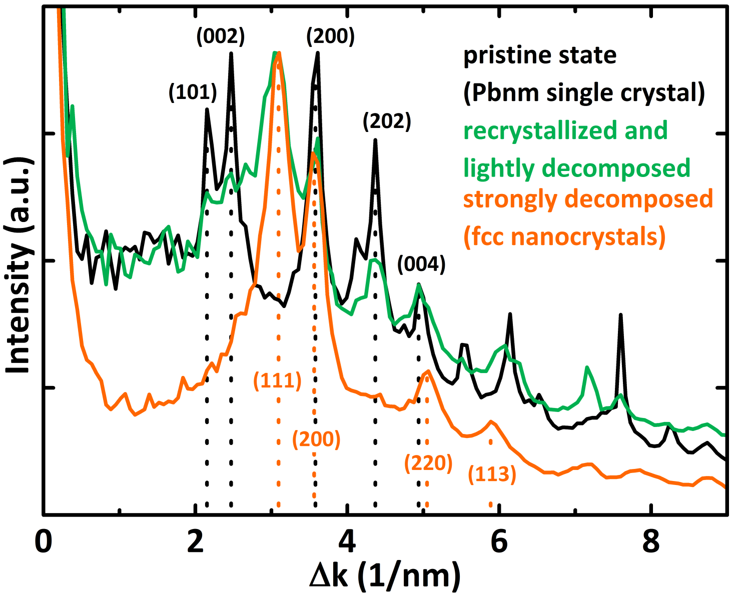

**Figure 3.11:** Rotationally averaged FFTs of 16 x 16 $nm^2$ large areas at the edge of a P73-PCMO thin film. Shown is the pristine Pbnm single crystal (black), the fcc nanocrystals after decomposition for 8 min at 7.4 nA in 5 Pa $H_2O$ (orange), and the lightly decomposed state after 12 min at 1.2 nA in 0.5 Pa $H_2O$ (green).

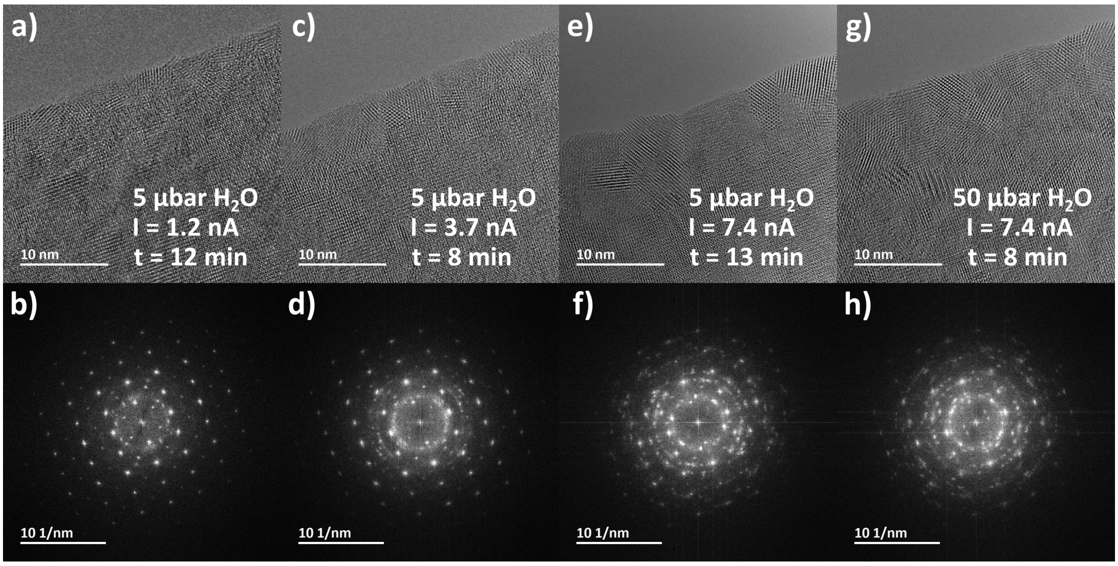

**Figure 3.12:** Bright field TEM images of the P73-PCMO edge and corresponding FFTs after various times at various beam intensities and $H_2O$ pressures, as indicated in the image.

#### 3.2.2.5 ETEM control experiments on RP-PCMO in $O_2$ and/or He

Prior to the ETEM experiment presented in Figure 3.8, the same RP-PCMO particle has been exposed to the beam in vacuum and 0.7 Pa of He. Its amorphous surface layer is stable against beam damage in vacuum and is only partly being removed in He (Video 6), presumably only some carbon-rich areas formed in high vacuum.

Other RP-PCMO particles are exposed to $O_2$ (or $O_2 + He$) to study the electrochemical oxidation of amorphous surface layers in the absence of catalysis. In the first experiment, we expose a particle to 100 Pa of $O_2$. The pristine state of a near $(1\bar{1}3)$ facet observed in <110> orientation of the Fmm2 structure is shown in Figure 3.13 a. Some stacking fault-like, Pr-rich defects of perovskite structure are observed due to incomplete reaction with CaO. Arrows mark such a layer of three perovskite unit cells. At this high oxygen pressure, in situ electron beam illumination results in strong cationic surface movement, especially at corners and curved facets. (Video 7) However, while some amorphous material is removed, it mostly crystallizes to form low indexed facets of the underlying single crystal (Figure 3.13 b). Contrary to the trend with Ca-content in P-PCMO and despite the 200 times higher pressure compared to other ETEM experiments, the RP-PCMO is very stable during the 14 minutes of the in situ experiment.

The second experiment is performed on a crystal observed in <110> zone axis with a 3-4 nm thick layer of amorphous material on its surface due to lamella preparation. (Figure 3.13 c) The particle is exposed to a mixture (1:1) of He and $O_2$ at a pressure of 0.6 Pa. Under these conditions, the surface material crystallizes to form a Pr-rich perovskite, while the RP-PCMO acts as a stable substrate allowing epitaxial growth. (Figure 3.13 d) The epitaxial relationship is clearly demonstrated by FFTs of the orthorhombic bulk (blue, space group Fmm2) and the pseudo-cubic surface (red, space group Pm3m). Post-mortem EELS points to depletion of Mn and Ca in the surface layer, due to damage created during lamella preparation and leaching during the ETEM experiment. (Figure 3.14)

In summary, the ETEM experiments in section 3.2.2 confirm the stability trends found by ex situ electrochemistry and provide valuable complementary insight: P91- and RP-PCMO retain their structure, while recrystallization of the P73-PCMO triggers and facilitates chemical decomposition.

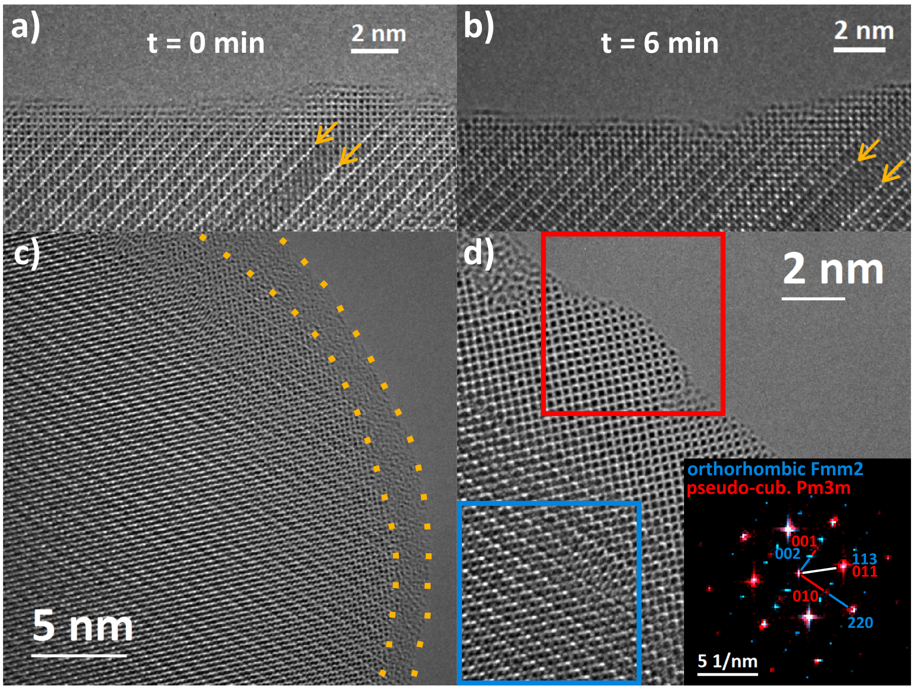

**Figure 3.13:** a)-b) RP-PCMO single crystal with a Pr-rich perovskite stacking fault-like defect observed in <110> zone axis at different times of the in situ experiment in 100 Pa $O_2$. c)-d) Other single crystal observed in <110> zone axis in 0.3 Pa $O_2$ + 0.3 Pa He. c) Pristine state with amorphous surface layer due to specimen preparation. d) Epitaxial crystallization in pseudo-cubic perovskite structure (<100> zone axis) on top of the RP-PCMO single crystal during the in situ experiment, as demonstrated by the inset of corresponding FFTs.

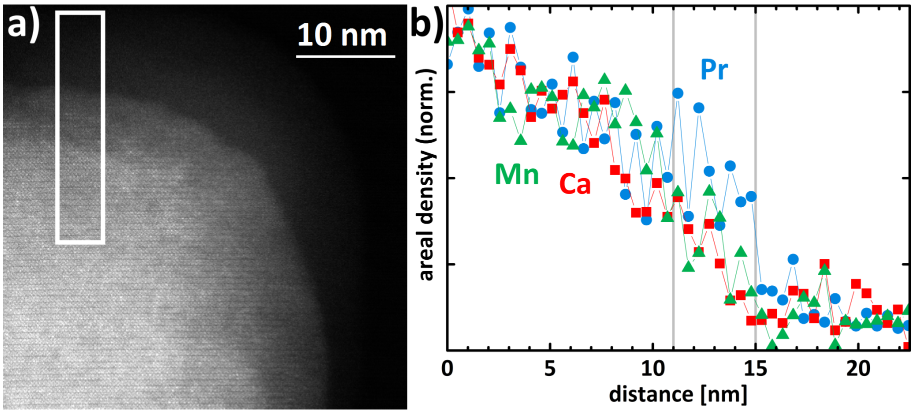

**Figure 3.14:** a) HAADF STEM image of RP-PCMO after ETEM experiment in $O_2$ + He. The white rectangle marks the area, in which the areal density of Pr, Ca, and Mn has been measured by EELS. b) Line profiles of Pr (M-edge, blue circles), Ca (L-edge, red squares), and Mn (L-edge, green triangles) after horizontal integration and normalization of each profile in the thick region. Significantly increased Pr concentration compared to the bulk composition is observed within the in situ crystallized material at 11-15 nm (Figure 3.13 d).

# 3.3 Discussion

## 3.3.1 Electron Beam Driven Electrochemistry in ETEM

The comparison of stability trends in RRDE and ETEM studies as a function of material composition is a powerful approach for identifying destabilizing processes and corrosion channels. However, ETEM observations cannot be directly compared to ex situ electrochemical stability analysis due to differences in composition and conductivity of the electrolyte, pH value, pressure, and beam-induced effects.[73, 88, 105] Thus, distinguishing between electrochemical and beam damage effects is an important challenge of ETEM studies. Inelastic scattering of beam electrons has two main effects: First, the emission of secondary electrons creates a positive space charge within the material, which can drive electrochemical surface reactions. Second, knock-on damage induces point defects by displacing lattice atoms. Control experiments in high vacuum or He demonstrate that all systems, including P73-PCMO, are stable against beam damage, ruling out knock on processes as a significant mechanism for the observed effects during ETEM experiments. Additionally, instead of purely chemical effects, we observe beam-induced electrochemistry, which is supported by the fact that the structural and chemical effects as well as changes in oxidation state in reactive gasses ($O_2$, $H_2O$) only occur in combination with the electron beam, i.e. the observed changes set in only after unblanking of the beam. Macroscopic electrical measurements yield a specific resistance of the porous electrode materials of 4.7 kΩcm. The investigated TEM specimens can therefore be estimated to have a ground resistance of roughly 500 MΩ. The surface potential under illumination by an electron beam of 4 nA is evaluated to a value of ca. $0.7 \pm 0.1$ V by using equation (7) in Mildner et al.[105] The relatively large error in this order of magnitude estimation stems from uncertainties in estimated electric resistance of the porous thin lamella areas as well as from the deviation of the studied samples from planar lamella geometry underlying equation (7). Nevertheless, the estimated potential is electrochemically relevant for either driving material dependent electrode redox processes or even the OER. Increasing the electron flux accelerates the observed processes, but does not lead to new phenomena within the used limits.

### 3.3.2 Corrosion Pathways and Driving Forces

We suggest that the observed stability trends can be mainly attributed to different character of the iono-covalent Mn-O bond. In the P-PCMO systems, Ca-doping shifts the O 2p and Mn 3d bands towards each other, increasing hybridization and covalence of the Mn-O bond, as shown by X-ray absorption spectroscopy. (Figure 3.1 d) Higher covalence shifts the O 2p band towards the Fermi level and thus facilitates the oxidation of surface lattice oxygen and the formation of point defects like $V_O$ and protonation.[73,81] Redox active lattice oxygen can therefore participate in OER mechanisms, creating an active state that is vulnerable to corrosion.[76,167] Specifically, lattice oxygen mediated OER mechanisms bear the risk of $V_O$ diffusion into the bulk of the catalyst, creating inhomogeneous strain.[168,169] This strain can drive nucleation of misoriented surface nanocrystals and therefore further drive the corrosion from an O depleted perovskite structure towards a chemically decomposed state, as observed in ETEM experiments on P73-PCMO. (Figure 3.3 and 3.4) In previous ETEM and in situ XANES experiments in $H_2O$ vapor under positive bias, surface reduction of P-PCMO at intermediate and high Ca doping was observed despite nominally oxidizing conditions due to formation of $V_O$ acting as electron donors.[73,74,105] Phase decomposition of P-PCMO into A-O and Mn-O rich phases above a critical $V_O$ concentration has also been observed for vacuum annealed thin films.[170]

In contrast, the increased ionic character of the Mn-O bond in Pr-rich P91-PCMO suppresses significant OER involvement of lattice O by preventing the formation of $O^{1-}$ species and $V_O$.[171,172] Its remarkable stability in ETEM experiments suggests that no significant $V_O$ formation occurs in contact with $H_2O$ vapor at positive potentials. (Figure 3.7) Accordingly, in situ XANES at the Mn L-edge of $PrMnO_3$ showed additional changes compared to Ca-doped specimens, which cannot simply be interpreted as $Mn^{2+}$ formation.[74]

In summary, continuous $V_2$ generation at the surface during OER and their migration into the subsurface can induce phase decomposition of the perovskite structure by inducing point defect strain. The highly strained grain boundaries between the formed nanocrystals may then further facilitate chemical decomposition. The subsequent beam-driven leaching of Ca and Mn or, in other words, knockout of light cations is shown by EELS. (Figure 3.4 e-h) In addition, the high solubility of Ca promotes the formation of weakly bound CaOH in the liquid surface layer, which is then likely to be knocked out by the beam. This can result in reduced or oxidized Mn species, as demonstrated in earlier ETEM experiments at different pressures of $H_2O$.[88]

However, the higher stability of RP-PCMO despite its much higher Ca content compared to P73-PCMO rules out Ca dissolution as the primary driving force for corrosion. Also, RP-PCMO shows clear Mn oxidation in 0.5 Pa $H_2O$, which points against the $V_O$ formation of its perovskite counterparts and is probably caused by uptake of oxygen from $H_2O$ molecules. The observed formation of nanocrystals in $H_2O$ evolves from the amorphous surface material instead of recrystallization of the RP phase. (Figure 3.8) Moreover, its ability to enforce epitaxial growth of the thick, initially amorphous surface layer during beam-driven crystallization in $O_2 + He$ further demonstrates its high structural stability. (Figure 3.13 d) However, crystallization forms Pr-rich P-PCMO instead of RP-PCMO, as the electron beam can knock Ca and Mn out of the weakly bound amorphous material. Leaching of the light cations apparently decreases the A/Mn ratio to nearly 1 (the stoichiometric value of P-PCMO). Furthermore, the A/Mn ratio could already have been decreased in the initial state of the amorphous TEM specimen regions due to preparation by ion milling.

In conclusion, we suggest that the more ionic character of the Mn-O bond of P91- and RP-PCMO (Figure 3.1 d) inhibits excessive $V_O$ formation, avoiding inhomogeneous strain at the catalyst surface. In addition, the rock salt-like AO double layers permit much easier relaxation of strain by non-stoichiometric oxygen compared to the perovskite structure.[164] Finally, increased diffusion within these layers may also play a role by homogenizing strain fields within the material.[173]

## 3.4 Conclusions

We demonstrate that all investigated systems (P73-PCMO, P91-PCMO, and RP-PCMO) are stable against beam damage in the TEM, unless their bond strength and phase stability is reduced by beam driven electrochemistry involving reactive gasses during ETEM experiments. In the case of P-PCMO, the electrochemical stability shows a strong dependence on Ca-doping, stemming from change of the Mn-O bond character. Most probably, the more ionic character in P91-PCMO stabilizes the material against point defect-driven corrosion, while P73-PCMO recrystallizes and chemically decomposes during ETEM experiments due to its highly covalent bond character. In contrast, RP-PCMO is much more stable despite its high Ca content, highlighting the importance of ionic bond character over effects of Ca-stoichiometry. These observations demonstrate that perovskite electrocatalysts of improved activity and stability can be developed by systematically tuning the defect chemistry by covalence of the transition metal-oxygen bonds.

## 3.5 Experimental Section

### 3.5.1 Sample Preparation

The perovskite powders are synthesized from calcium nitrate tetrahydrate $Ca(NO_3)_2$ $4\,H_2O$ (99%), manganese nitrate tetrahydrate $Mn(NO_3)_2$ $4\,H_2O$ (99.5%), praseodymium nitrate hexahydrate $Pr(NO_3)_3\,6\,H_2O$ (99.9%), and gelatin using a wet chemistry method. Appropriate amounts of nitrates for 10 g of final product are dissolved in distilled water and stirred at room temperature for 20 min. Then, the 10 g gelatin solution, stirred at 40 °C for 30 min, is added to the solution of the cations and the whole solution is continually stirred at 60 °C for 2 h until it becomes clear with no precipitates or particulates. Then, a heat bath at 90 °C is used to evaporate the solvents until the desired resin-like product is obtained followed by drying at 200 °C for 5 min. Finally, the brownish black powder is calcined at 900 °C for 5 h.

Ruddlesden-Popper powders are prepared by conventional solid-state reaction but with a novel approach starting from a stoichiometric mixture of $Pr_{0.5}Ca_{0.5}MnO_3$ and CaO powders. The reagents are mixed in an agate mortar, ball-milled for 15 min, and heated in air at 1100 °C for 24 h. Structural analysis by X-ray Diffraction (XRD) and Rietveld refinement has already been published. [157]

The oxide electrodes for electrochemical measurements are prepared using a protocol published by Suntivich et al. but omitting Nafion. [174] The ink is prepared using acetylene black (AB) carbon (99.9+%, Alfa Aesar) treated in nitric acid overnight at 80 °C and subsequently filtered and dried at 100 °C. Additionally, tetrahydrofuran (THF, 99.9+%, Sigma Aldrich) and the respective oxide powder are mixed and sonicated for 30 min. The ink is composed of 1 mg $mL^{-1}$ AB carbon and 5 mg $mL^{-1}$ oxide particles. Finally, $2 \cdot 5\,\mu L$ of the ink are drop-casted on a freshly polished glassy carbon (GC) electrode (0.1257 $cm^2$ area, ALS Co. Ltd) to yield 0.4 $mg_{ox}\,cm^{-2}$ disk oxide loading, carefully controlling the drying to ensure a homogeneous coverage.

Particle TEM specimens are produced from pressed pellets of the respective powders. They are mechanically polished and ion-milled until perforation using a Gatan PIPS 691 system.

$Pr_{0.7}Ca_{0.3}MnO_3$ (P73-PCMO) thin films of 300 nm thickness are prepared by reactive ion beam sputtering (Xe sputter gas at 1 kV, 20 mA) from a sintered target onto single crystalline MgO substrate. TEM cross-section lamellae are cut by focused ion beam (30 kV, 7 nA - 300 pA) and are subsequently thinned at 5 kV and 29 pA in a FEI Nova Nanolab 600 dual beam FIB (focused ion beam). Further thinning is done by Ar ion milling at 2 kV to 500 V in a Gatan 671 Precision Ion Polishing System. The final lamellae have an amorphous layer of 2 - 5 nm thickness on the single crystalline edge. Amorphization is accompanied by some oxygen depletion due to preferential etching as indicated by EELS based on a reduced Mn valence state, i.e. increased $L_3/L_2$ ratio and reduced intensity of the low-energy O K-edge feature.

### 3.5.2 RRDE Characterization

Electrochemical measurements are carried out with two Interface 1000E (Gamry Instruments Inc.) used as bipotentiostats assembled with a RRDE-3A rotator (ALS Co. Ltd) in a polytetrafluoroethylene (P73-PCMO) or glass (RP-PCMO) cell using a three-electrode configuration at room temperature. The measurements are performed in 0.1 M KOH prepared from 1 M stock solution (Sigma Aldrich) and Milli-Q water (> 16.5 MΩcm) saturated with either $O_2$ or Ar (99.999%, Air liquid). The potentials are referenced to a saturated calomel electrode (ALS Co. Ltd) calibrated to the reversible hydrogen electrode (RHE) scale by CV measurement of hydrogen evolution in $H_2$-saturated 0.1 M KOH, where the average voltages of zero current from the positive and negative-going CV scans are found at 0.997 V vs. RHE. Additionally, the potentials are corrected for electrolyte resistance extracted from the high frequency intercept of the real impedance measured by impedance spectroscopy at the disk. Cleanliness of the Pt ring is checked before each experiment by matching cyclic voltammograms (CV) with polycrystalline Pt. [175] CV measurements at the disk are performed at 10 mV $s^{-1}$ and 1600 rpm. The ring voltage is always set to 0.4 V vs. RHE, where the ring current is diffusion-limited. The currents of the oxide electrodes are corrected for the amount of the deposited oxide and corresponding surface area obtained by scanning electron microscopy (SEM) analysis of the particle size distribution. [157]

### 3.5.3 ETEM

The HRTEM images and related videos presented in this work are collected using an aberration-corrected, Schottky field-emission gun transmission electron microscope

(FEI Titan 80–300 environmental (S)TEM) operated at 300 kV. The microscope base pressure under high vacuum (HV) condition is below $10^{-4}$ Pa. During the experiments, up to 100 Pa of $O_2$, $O_2$ + He, He or $H_2O$ vapor is introduced into the ETEM. The in situ videos are acquired using a script for Gatan's Digital Micrograph software. The script is provided by the Ernst Ruska-Centre (ER-C) for Microscopy and Spectroscopy. E-beam intensities indicated are measured using the e-beam current reading from the phosphor viewing screen. All particles or films are characterized in high vacuum before introducing any gas into the TEM chamber. At least three particles are tested and observed for each material to check the repeatability of observations.

### 3.5.4 EELS and EDX

Spectroscopy is performed in scanning diffraction mode, using a Gatan Quantum 965ER post-column energy filter for EELS and an Oxford Instruments X-Max 80 $mm^2$ silicon drift detector for EDX. Quantification of the EDX spectra on the basis of the Pr L-, Ca K-, and Mn K-lines is performed by the Cliff Lorimer thin ratio section method using the commercial software INCA (Oxford Instruments). The energy resolution for EELS is ca. 1 eV, measured as the full width at half height of the zero-loss peak. The convergence angle is 10.0 mrad and the effective collection angle is 21.9 mrad. Quantification of the EEL spectra is performed on the basis of the Pr M-, Ca L-, and Mn L-edges, which is described in more detail in section 3.6.

## Acknowledgments

Funding from the Deutsche Forschungsgemeinschaft (DFG) within SFB1073 (project C02) is gratefully acknowledged.

## 3.6 Supporting Experimental Section

### 3.6.1 Covalence of the Mn-O Bond

X-ray absorption at the O K-edge is very sensitive to the character of the iono-covalent Mn-O bond. The low energy feature around 528-531 eV represents excitation into

O 2p states hybridized with Mn 3d $e_g$. Its intensity thus mainly increases in response to two effects, namely the increasing nominal Mn valence and increasing covalence of the Mn-O bond. The number of $e_g$ holes per Mn is determined by the nominal Mn valence due to substitution of $Pr^{3+}$ by $Ca^{2+}$ assuming ionic bonds with $O^{2-}$ and strong Hund's coupling in both PCMO systems.[58] Remaining intensity differences qualitatively reflect the covalence factor. X-ray absorption edges (total electron yield) of different P- and RP-PCMO samples at various Pr/Ca ratios are presented in Figure 3.2, where the integrated areas are highlighted by filled curves. The integrated intensity below 531 eV has been divided by the nominal Mn valence to cancel the effect of $e_g$ filling. The thin film measurements were performed at BESSY II (Helmholtz-Zentrum Berlin, Germany) and the nanoparticle measurements at the Canadian Light Source (Saskatoon, Canada). Details of the measurements have been described elsewhere.[74, 157] To compare the results of thin films and nanoparticles, the obtained covalence factors are normalized by the value for P55-PCMO (Figure 3.1 d). Covalence is found to be highest in Ca-doped P-PCMO and decreases towards $PrMnO_3$ below half doping. In contrast, Pr-doping of $Ca_2MnO_4$ (RP-PCMO) leads to much stronger decrease in covalence.

### 3.6.2 Chemical Composition of the Pristine P73-PCMO Particles

The chemical composition of pristine P73-PCMO nanoparticles is characterized by electron energy loss spectroscopy (EELS) and energy dispersive X-ray spectroscopy (EDX) in scanning transmission mode (STEM). A total of twelve EDX spectra are recorded at different particles. EEL spectra are extracted from seven spectrum images of different particles. The Pr M-, Ca L-, and Mn L-edges are used for quantification. Power-law functions are fit to 50 eV wide windows in front of each edge for background subtraction. Hartree-Slater type cross-section functions from Gatan's Digital Micrograph are fit to the post-edge regions, starting behind the white lines to avoid artifacts from ligand field or oxidation state. The windows are located at 960 - 1055 eV (Pr M), 360 - 395 eV (Ca L), and 665 - 730 eV (Mn L), being as wide as 10% of the corresponding edge energy. Results are summarized in Table 3.2. Deviations from the nominal composition of $Pr_{0.7}Ca_{0.3}MnO_3$ are within statistical errors of the average values, as given in parenthesis.

### 3.6.3 Post Mortem EELS of P73-PCMO

Quantification of the post mortem EEL spectra follows the same protocol as described for the pristine state. During the post mortem analysis, carbon-rich contamination from the TEM accumulated in a thick surface layer, producing a strong C K-edge signal and largely contributing to the total relative specimen thickness $t_{tot} / \lambda$. The contribution of Pr, Ca, Mn, and C to the total relative thickness is calculated by weighting each mole fraction by the element specific scattering cross section.[176] The specimen specific thickness $t / \lambda$ as given in Table 3.3 is then corrected for C contribution according to $t = t_{tot} \cdot (1 - x_C)$, where $x_C$ denotes the weighted mole fraction of carbon calculated from the C K-edge. An overview of the corroded region is given in the HAADF-STEM image in Figure 3.5. The varying fractions of the three cations in areas A-D (Figure 3.4 e) is demonstrated by the corresponding high loss edges in Figure 3.4 f-h. HAADF-STEM images of areas E-H are shown in Figure 3.6.

### 3.6.4 In Situ EELS of RP-PCMO in $H_2O$

The energy scale of the O K-edge spectra in Figure 3.9 a is calibrated by adjusting the high-energy maximum, identified by a parabolic fit, to 543 eV. A power-law background function, fit from 510 to 525 eV, is then subtracted. Finally, a parabolic fit is used to identify the intensity of the high-energy maximum, by which the spectra are divided for normalization. Sawatzki–Golay smoothening is applied by fitting 3rd order polynoms to 15 adjacent data points. The Mn L-edge spectra in Figure 3.9 b are energy calibrated, so that the $L_2$ maximum lies at 653 eV. A power-law background is fit from 580 to 635 eV and subtracted. The remaining intensities are divided by the $L_2$ maximum for normalization.

A similar normalization protocol, including subtraction of a Hartree-Slater type background, and integration of the $L_3$ and $L_2$ edges is used to calculate the Mn valence state.[177] The results reflect the qualitative observation of in situ oxidation and slight reduction afterwards (Table 3.5) The absolute values might be subject to systematic errors due the fact that the relationship between $L_3 / L_2$ ratio and Mn valence was established for perovskite $La_{1-x}Ca_xMnO_3$ instead of Ruddlesden-Popper type materials.[178] HAADF-STEM images of the areas of spectrum collection are shown in Figure 3.10.

### 3.6.5 Image Simulation

Electrochemical reactions strongly depend on the surface chemistry. However, TEM only allows for the observation of projected edges, where the signal-to-noise ratio of both EELS and EDX is poor and usually requires long exposures or strong beam currents. All this can mask the real composition of studied materials in contact with an environmental medium because of beam induced changes. Therefore, we perform thorough HRTEM image simulations using the QSTEM package.[179] The main questions are:

1. What is the thickness of specimen at the edge?
2. Is it possible to see a difference between oxygen and cation terminated surfaces of RP-PCMO?
3. Is it possible to observe and distinguish individual Pr, Mn, Ca and O atoms?

Figure 3.15 shows an exemplary experimental and simulated image as well as the corresponding atomic model to answer these questions. Our simulations fit to experimental images when the thickness is in a range between 2 and 3 nm. The rock salt-like bilayers can be identified as the bright lines with the dark adjacent Pr/Ca columns. Varying intensity in these columns reflects the random distribution of Pr and Ca. The dark circles between the rock salt layers represent the MnO columns of the perovskite-like layers. In order to understand image contrast at the surface, cation-terminated and oxygen-terminated $(1\bar{1}3)$ facets are constructed Figure 3.15 b. The simulated image (Figure 3.15 c) shows a clear but weak difference between two types of termination. However, one should take into account that each oxygen column has no vacancies, there is no movement, the specimen is perfectly stable and there is no amorphous layer. The contrast difference between Ca, Mn and Pr cations is not significant and depends on the particular atomic arrangements at the surface.

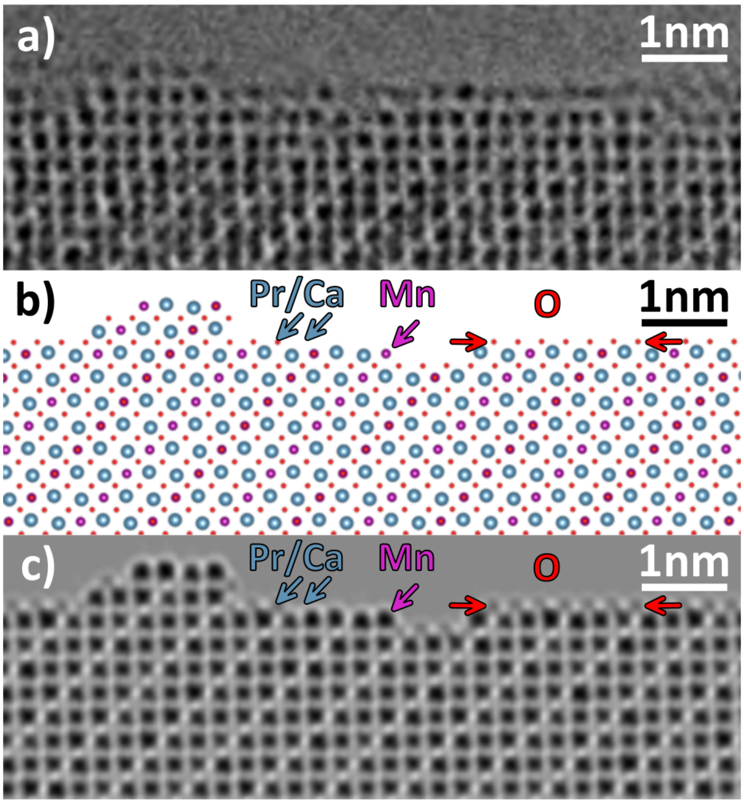

**Figure 3.15:** Image simulation of a $(1\bar{1}3)$ facet of RP-PCMO with either cation or oxygen termination. a) experimental bright field image, b) atomic model, c) image simulation, showing weak contrast of fully occupied surface oxygen columns and some brightness variations in A-site columns due to random distribution of Pr and Ca, while MnO columns are of uniform contrast. At the surface and the corners, atomic columns of cations can have significantly different contrast depending of their atomic environment.

# Chapter 4

# Summary and Outlook

It is well accepted that active catalyst surfaces differ from their equilibrium state. This is due to dynamic valence changes and structural responses to intermediate reaction steps. In situ studies of these active states are a crucial component of gaining a mechanistic understanding of the underlying processes. This thesis applies two complementary in situ methods, soft X-ray spectroscopy and environmental transmission electron microscopy (ETEM), to study the catalysis of the oxygen evolution reaction (OER) on manganite model catalysts. Spectroscopy using soft X-ray synchrotron radiation combines high energy resolution with high surface sensitivity. ETEM provides atomically resolved structural, chemical and electronic information and uses the electron beam to induce positive potentials. However, interpretation of ETEM data requires considering side effects of the high energy electron beam due to four orders of magnitude higher scattering cross section compared to photons. It is therefore a major challenge to distinguish between effects of beam-induced electrochemistry and radiation damage. In particular, radiation damage is strongly influenced by preexisting damage from specimen preparation or electrochemically induced corrosion of otherwise stable materials. Reversible changes of the topmost surface are observed during X-ray spectroscopy, whereas ETEM enables the observation of atom dynamics on active surfaces, if clean, undamaged, electron transparent specimens can be prepared.

In principle, surface processes in the gaseous environment of in situ experiments at µbar to mbar pressure may differ from the behavior in liquid electrolytes at atmospheric pressure. However, the presented results show similar stability trends with Ca-doping for the $Pr_{1-x}Ca_xMnO_3$ perovskite (P-PCMO) as well as in comparison with its layered Ruddlesden-Popper type $Pr_{0.5}Ca_{1.5}MnO_4$ counterpart (RP-PCMO).

The in situ studies at P-PCMO in water vapor show formation of surface point defects, which is enhanced at higher Ca-doping. Formation of defects like oxygen vacancies is, for instance, supported by XANES based on manganese reduction despite nominally oxidative bias and subsequent annihilation in oxygen gas. In contrast, no vacancy formation is observed for Ca-rich RP-PCMO. Instead, in situ electron energy loss spectroscopy (EELS) shows manganese oxidation which is most likely induced by uptake of oxygen from water molecules.

P-PCMO at intermediate Ca-doping levels is relatively unstable. This is demonstrated via ETEM by real-time in situ observation of recrystallization on a 10 - 20 nm scale. On the other hand, under the same ETEM conditions, the Pr-rich P-PCMO ($x_{Ca} = 0.1$) as well as the Ca-rich RP-PCMO surfaces are significantly more stable, keeping their single-crystalline state. This is in close agreement with stability trends seen by ex situ experiments. Nevertheless, significant movement of cations across the structurally stable surfaces is observed during the ETEM experiments. First results show that cation dynamics are confined to the uppermost atomic layer on low-indexed facets of clean, crystalline edges. (section 3.2.2.2) A preferential formation and annihilation of Mn vacancies compared to A-cations is observed, which points towards a metal-centered OER mechanism.

The results of this thesis clearly indicate that electrochemical stability can primarily be ascribed to the character of the Mn–O bond based on soft X-ray spectroscopy on the pristine catalysts. The bond is significantly more ionic in the relatively stable RP-PCMO compared to the relatively unstable P-PCMO, where stronger O 2p contributions to the hybridized states at the valence band edge lead to more covalent bond character. In addition, a trend of increasing covalence with increasing Ca-doping is observed for P-PCMO. However, the high stability of the Ca-rich RP-PCMO demonstrates that bond covalence dominates over direct effects of chemical composition.

The observation of cation movement across stable catalyst surfaces opens up new perspectives for future ETEM work. For instance, systematic investigation of the atom dynamics on intact crystalline P-PCMO edges in comparison to more stable catalysts is a promising focus. The presented results demonstrate that challenging requirements would have to be fulfilled. First, preparation of specimen edges completely free of amorphous layers obscuring the crystal surface is especially challenged by high etching cross sections of Ca-rich materials. Secondly, the tendency for fast accumulation of point defects in P-PCMO suggests experiments at sufficiently low pressures to avoid recrystallization and degradation of the material. Differences in the characteristics of surface dynamics might yet unveil valuable information on redox active species and nature of active sites as a function of catalyst material. A further step would be to control surface dynamics by external bias in various 2-electrode geometries which is severely challenged by uncertainties about the electric field distribution across the catalyst's interface to the gaseous electrolyte. (section 1.3) Future quantification of these fields via off-axis electron holography as planned in Göttingen can provide the necessary feedback allowing systematic bias control. For example, TEM specimen holders equipped with a scanning tunneling microscope (STM) tip can in principle be used for applying local voltages.[180–182] This type of holder was successfully applied to suppress reactions of Ca-rich P-PCMO with a $H_2O/SiH_4$ mixture in earlier ETEM work.[73] A complementary approach aiming to bridge the conditions between high resolution ETEM conditions in gas phases and liquid phase electrochemistry is the use of liquid flow cell TEM holders.[183] These membrane holders allow implementation of a reference electrode for quantitative potential control while strongly limiting the spatial resolution of the TEM. In conclusion, the combination of different in situ methods and complementary rotating ring disk electrochemistry (RRDE) provides valuable information on active catalysts in non-equilibrium states and is thus a necessary step in the search for stable electrocatalysts with high efficiency for water oxidation and oxygen evolution.

# Bibliography

[1] John A. Turner. A realizable renewable energy future. *Science*, 285(5428):687–689, 1999.

[2] N. S. Lewis and Daniel G Nocera. Powering the planet: Chemical challenges in solar energy utilization. *Proceedings of the National Academy of Sciences*, 103(43):15729–15735, 2006.

[3] Wesley T Hong, Marcel Risch, Kelsey A Stoerzinger, Alexis Grimaud, Jin Suntivich, and Yang Shao-Horn. Toward the rational design of non-precious transition metal oxides for oxygen electrocatalysis. *Energy Environ. Sci.*, 8(5):1404–1427, 2015.

[4] Maximilian Schalenbach, Geert Tjarks, Marcelo Carmo, Wiebke Lueke, Martin Mueller, and Detlef Stolten. Acidic or alkaline? towards a new perspective on the efficiency of water electrolysis. *Journal of The Electrochemical Society*, 163(11):F3197–F3208, 2016.

[5] Kai Zeng and Dongke Zhang. Recent progress in alkaline water electrolysis for hydrogen production and applications. *Progress in Energy and Combustion Science*, 36(3):307 – 326, 2010.

[6] Marcelo Carmo, David L. Fritz, Jürgen Mergel, and Detlef Stolten. A comprehensive review on pem water electrolysis. *International Journal of Hydrogen Energy*, 38(12):4901 – 4934, 2013.

[7] L. D. Burke and T. O. O'Meara. Oxygen electrode reaction. part 2. - behaviour at ruthenium black electrodes. *J. Chem. Soc., Faraday Trans. 1*, 68:839–848, 1972.

[8] D.N. Buckley and L.D. Burke. The oxygen electrode. part 4. - lowering of overvoltage for oxygen evolution at noble-metal electrodes in presence of ruthenium

salts. *Journal of Electroanalytical Chemistry and Interfacial Electrochemistry*, 52(3):433 – 442, 1974.

[9] Denis N. Buckley and Laurence D. Burke. The oxygen electrode. part 6. - oxygen evolution and corrosion at iridium anodes. *J. Chem. Soc., Faraday Trans. 1*, 72:2431–2440, 1976.

[10] Denis N. Buckley, Laurence D. Burke, and Joseph K. Mulcahy. The oxygen electrode. part 7. - influence of some electrical and electrolyte variables on the charge capacity of iridium in the anodic region. *J. Chem. Soc., Faraday Trans. 1*, 72:1896–1902, 1976.

[11] M.H. Miles, E.A. Klaus, B.P. Gunn, J.R. Locker, W.E. Serafin, and S. Srinivasan. The oxygen evolution reaction on platinum, iridium, ruthenium and their alloys at 80 °C in acid solutions. *Electrochimica Acta*, 23(6):521 – 526, 1978.

[12] Sergio Trasatti and Giovanni Buzzanca. Ruthenium dioxide: A new interesting electrode material. solid state structure and electrochemical behaviour. *Journal of Electroanalytical Chemistry and Interfacial Electrochemistry*, 29(2):A1 – A5, 1971.

[13] R. Kötz, H. J. Lewerenz, and S. Stucki. XPS Studies of Oxygen Evolution on Ru and $RuO_2$ Anodes. *Journal of The Electrochemical Society*, 130(4):825–829, 1983.

[14] R. Kötz and S. Stucki. Stabilization of $RuO_2$ by $IrO_2$ for anodic oxygen evolution in acid media. *Electrochimica Acta*, 31(10):1311 – 1316, 1986.

[15] M. H. Miles, G. Kissel, P. W. T. Lu, and S. Srinivasan. Effect of Temperature on Electrode Kinetic Parameters for Hydrogen and Oxygen Evolution Reactions on Nickel Electrodes in Alkaline Solutions. *Journal of The Electrochemical Society*, 123(3):332–336, 1976.

[16] P. Oliva, J. Leonardi, J.F. Laurent, C. Delmas, J.J. Braconnier, M. Figlarz, F. Fievet, and A.de Guibert. Review of the structure and the electrochemistry of nickel hydroxides and oxy-hydroxides. *Journal of Power Sources*, 8(2):229 – 255, 1982.

[17] S. Trasatti. Electrocatalysis in the anodic evolution of oxygen and chlorine. *Electrochimica Acta*, 29(11):1503 – 1512, 1984.

[18] M.R. Gennero de Chialvo and A.C. Chialvo. Oxygen evolution reaction on thick hydrous nickel oxide electrodes. *Electrochimica Acta*, 33(6):825 – 830, 1988.

[19] Xianyou Wang, Hean Luo, Hongping Yang, P.J. Sebastian, and S.A. Gamboa. Oxygen catalytic evolution reaction on nickel hydroxide electrode modified by electroless cobalt coating. *International Journal of Hydrogen Energy*, 29(9):967 – 972, 2004. Cancun 2002.

[20] Lena Trotochaud, Samantha L. Young, James K. Ranney, and Shannon W. Boettcher. Nickel–Iron Oxyhydroxide Oxygen-Evolution Electrocatalysts: The Role of Intentional and Incidental Iron Incorporation. *Journal of the American Chemical Society*, 136(18):6744–6753, 2014. PMID: 24779732.

[21] José Ramón Galán-Mascarós. Water Oxidation at Electrodes Modified with Earth-Abundant Transition-Metal Catalysts. *ChemElectroChem*, 2(1):37–50, 2015.

[22] Seth Dunn. Hydrogen futures: toward a sustainable energy system. *International Journal of Hydrogen Energy*, 27(3):235 – 264, 2002.

[23] F. Mueller-Langer, E. Tzimas, M. Kaltschmitt, and S. Peteves. Techno-economic assessment of hydrogen production processes for the hydrogen economy for the short and medium term. *International Journal of Hydrogen Energy*, 32(16):3797 – 3810, 2007. TMS06: Symposium on Materials in Clean Power Systems.

[24] John B Goodenough. Theory of the Role of Covalence in the Perovskite-Type Manganites [La, M(II)]$MnO_3$. *Physical Review*, 100(2):564–573, 1955.

[25] John B. Goodenough. Perspective on Engineering Transition-Metal Oxides. *Chemistry of Materials*, 26(1):820–829, 2014.

[26] Oscar Diaz-Morales, Isis Ledezma-Yanez, Marc T. M. Koper, and Federico Calle-Vallejo. Guidelines for the Rational Design of Ni-Based Double Hydroxide Electrocatalysts for the Oxygen Evolution Reaction. *ACS Catalysis*, 5(9):5380–5387, 2015.

[27] Y. Matsumoto and E. Sato. Electrocatalytic properties of transition metal oxides for oxygen evolution reaction. *Materials Chemistry and Physics*, 14(5):397–426, 1986.

[28] Y. Matsumoto and E. Sato. Oxygen evolution on $La_{1-x}Sr_xMnO_3$ electrodes in alkaline solutions. *Electrochimica Acta*, 24(4):421 – 423, 1979.

[29] Masayuki Morita, Chiaki Iwakura, and Hideo Tamura. The anodic characteristics of massive manganese oxide electrode. *Electrochimica Acta*, 24(4):357 – 362, 1979.

[30] Yoshinori Naruta, Masa-aki Sasayama, and Takao Sasaki. Oxygen evolution by oxidation of water with manganese porphyrin dimers. *Angewandte Chemie International Edition*, 33(18):1839–1841, 1994.

[31] F. A. Armstrong. Why did nature choose manganese to make oxygen? *Philos. T. Roy. Soc. B*, 363:1263–1270, 2008.

[32] Mathias Wiechen, Hans-Martin Berends, and Philipp Kurz. Water oxidation catalysed by manganese compounds: from complexes to 'biomimetic rocks'. *Dalton Trans.*, 41:21–31, 2012.

[33] Mohammad Mahdi Najafpour and Davood Jafarian Sedigh. Water oxidation by manganese oxides, a new step towards a complete picture: simplicity is the ultimate sophistication. *Dalton Trans.*, 42:12173–12178, 2013.

[34] Michael Huynh, D. Kwabena Bediako, and Daniel G. Nocera. A Functionally Stable Manganese Oxide Oxygen Evolution Catalyst in Acid. *Journal of the American Chemical Society*, 136(16):6002–6010, 2014. PMID: 24669981.

[35] Mohammad Mahdi Najafpour, Gernot Renger, Malgorzata Holynska, Atefeh Nemati Moghaddam, Eva Mari Aro, Robert Carpentier, Hiroshi Nishihara, Julian J. Eaton-Rye, Jian Ren Shen, and Suleyman I. Allakhverdiev. Manganese Compounds as Water-Oxidizing Catalysts: From the Natural Water-Oxidizing Complex to Nanosized Manganese Oxide Structures. *Chemical Reviews*, 116(5):2886–2936, 2016.

[36] Jaemin Kim, Xuxia Chen, Yung-Tin Pan, Pei-Chieh Shih, and Hong Yang. W-Doped $CaMnO_{2.5}$ and $CaMnO_3$ Electrocatalysts for Enhanced Performance in Oxygen Evolution and Reduction Reactions. *Journal of The Electrochemical Society*, 164(12):F1074–F1080, 2017.

[37] Matthew P. Johnson. Photosynthesis. *Essays In Biochemistry*, 60(3):255–273, 2016.

[38] Junko Yano, Jan Kern, Kenneth Sauer, Matthew J. Latimer, Yulia Pushkar, Jacek Biesiadka, Bernhard Loll, Wolfram Saenger, Johannes Messinger, Athina Zouni, and Vittal K. Yachandra. Where water is oxidized to dioxygen: Structure of the photosynthetic $mn_4ca$ cluster. *Science*, 314(5800):821–825, 2006.

[39] Yulia Pushkar, Junko Yano, Pieter Glatzel, Johannes Messinger, Azul Lewis, Kenneth Sauer, Uwe Bergmann, and Vittal Yachandra. Structure and Orientation of the $Mn_4Ca$ Cluster in Plant Photosystem II Membranes Studied by Polarized Range-extended X-ray Absorption Spectroscopy. *Journal of Biological Chemistry*, 282(10):7198–7208, 2007.

[40] Nicholas Cox, Marius Retegan, Frank Neese, Dimitrios A. Pantazis, Alain Boussac, and Wolfgang Lubitz. Electronic structure of the oxygen-evolving complex in photosystem II prior to O-O bond formation. *Science*, 345(6198):804–808, 2014.

[41] Changhui Chen, Chunxi Zhang, Hongxing Dong, and Jingquan Zhao. A synthetic model for the oxygen-evolving complex in $Sr^{2+}$-containing photosystem II. *Chem. Commun.*, 50:9263–9265, 2014.

[42] André Klauss, Michael Haumann, and Holger Dau. Alternating electron and proton transfer steps in photosynthetic water oxidation. *Proceedings of the National Academy of Sciences*, 109(40):16035–16040, 2012.

[43] Demetrios F Ghanotakis and Charles F Yocum. Photosystem II and the oxygen-evolving complex. *Annual review of plant biology*, 41(1):255–276, 1990.

[44] Vittal K. Yachandra and Junko Yano. Calcium in the oxygen-evolving complex: Structural and mechanistic role determined by x-ray spectroscopy. *Journal of Photochemistry and Photobiology B: Biology*, 104(1):51 – 59, 2011. Special Issue on Recent Progress in the Studies of Structure and Function of Photosystem II.

[45] Jacob S. Kanady, Emily Y. Tsui, Michael W. Day, and Theodor Agapie. A Synthetic Model of the $Mn_3Ca$ Subsite of the Oxygen-Evolving Complex in Photosystem II. *Science*, 333(6043):733–736, 2011.

[46] John O Bockris and Takaaki Otagawa. Mechanism of oxygen evolution on perovskites. *The Journal of Physical Chemistry*, 87(15):2960–2971, 1983.

[47] D. E. Hall. Alkaline water electrolysis anode materials. *Journal of The Electrochemical Society*, 132(2):41C–48C, 1985.

[48] S. K. Tiwari, P. Chartier, and R. N. Singh. Preparation of perovskite-type oxides of cobalt by the malic acid aided process and their electrocatalytic surface properties in relation to oxygen evolution. *Journal of The Electrochemical Society*, 142(1):148–153, 1995.

[49] J. Suntivich, K. J. May, H. A. Gasteiger, J. B. Goodenough, and Y. Shao-Horn. A Perovskite Oxide Optimized for Oxygen Evolution Catalysis from Molecular Orbital Principles. *Science*, 334(6061):1383–1385, 2011.

[50] C C L McCrory, S H Jung, J C Peters, and T F Jaramillo. Benchmarking Heterogeneous Electrocatalysts for the Oxygen Evolution Reaction. *Journal of the American Chemical Society*, 135(45):16977–16987, 2013.

[51] Rosalba A. Rincõn, Edgar Ventosa, Frank Tietz, Justus Masa, Sabine Seisel, Volodymyr Kuznetsov, and Wolfgang Schuhmann. Evaluation of Perovskites as Electrocatalysts for the Oxygen Evolution Reaction. *ChemPhysChem*, 15(13):2810–2816, 2014.

[52] Michaela S. Burke, Shihui Zou, Lisa J. Enman, Jaclyn E. Kellon, Christian A. Gabor, Erica Pledger, and Shannon W. Boettcher. Revised Oxygen Evolution Reaction Activity Trends for First-Row Transition-Metal (Oxy)hydroxides in Alkaline Media. *Journal of Physical Chemistry Letters*, 6(18):3737–3742, 2015.

[53] N. Ramadass. $ABO_3$-type oxides – Their structure and properties – A bird's eye view. *Materials Science and Engineering*, 36(2):231 – 239, 1978.

[54] John O'M. Bockris and Takaaki Otagawa. The Electrocatalysis of Oxygen Evolution on Perovskites. *Journal of The Electrochemical Society*, 131(2):290–302, 1984.

[55] David M. Sherman. The electronic structures of manganese oxide minerals. *Am. Mineral.*, 69(7-8):788–799, 1984.

[56] V. M. Goldschmidt. Die gesetze der krystallochemie. *Naturwissenschaften*, 14(21):477–485, 1926.

[57] Z. Jirák, S. Krupička, Z. Šimša, M. Dlouhá, and S. Vratislav. Neutron diffraction study of $Pr_{1-x}Ca_xMnO_3$ perovskites. *Journal of Magnetism and Magnetic Materials*, 53(1-2):153–166, 1985.

[58] Mohsen Sotoudeh, Sangeeta Rajpurohit, Peter Blöchl, Daniel Mierwaldt, Jonas Norpoth, Vladimir Roddatis, Stephanie Mildner, Birte Kressdorf, Benedikt Ifland, and Christian Jooss. Electronic structure of $Pr_{1-x}Ca_xMnO_3$. *Phys. Rev. B*, 95(23):235150, 2017.

[59] P. G. Radaelli, M. Marezio, H. Y. Hwang, S-W. Cheong, and B. Batlogg. Charge localization by static and dynamic distortions of the $MnO_6$ octahedra in perovskite manganites. *Phys. Rev. B*, 54:8992–8995, Oct 1996.

[60] J. A. V. Butler. Hydrogen overvoltage and the reversible hydrogen electrode. *Proceedings of the Royal Society of London. Series A, Mathematical and Physical Sciences*, 157(891):423–433, 1936.

[61] Erwin Riedel and Christoph Janiak. *Anorganische Chemie*. de Gruyter, 2007.

[62] Nicola Armaroli and Vincenzo Balzani. The future of energy supply: Challenges and opportunities. *Angewandte Chemie - International Edition*, 46(1-2):52–66, 2007.

[63] A. Marshall, B. Børresen, G. Hagen, M. Tsypkin, and R. Tunold. Hydrogen production by advanced proton exchange membrane (PEM) water electrolysers-Reduced energy consumption by improved electrocatalysis. *Energy*, 32(4):431–436, 2007.

[64] Holger Dau, Christian Limberg, Tobias Reier, Marcel Risch, Stefan Roggan, and Peter Strasser. The Mechanism of Water Oxidation: From Electrolysis via Homogeneous to Biological Catalysis. *ChemCatChem*, 2(7):724–761, 2010.

[65] Robert Schlögl. Sustainable Energy Systems: The Strategic Role of Chemical Energy Conversion. *Topics in Catalysis*, 59(8-9):772–786, 2016.

[66] P Sabatier. La catalyse en chimie organique. *Catalysis in Organic Chemistry (translated by Reidl. EE), Van Norstrand: Princeton, NJ*, 923, 1913.

[67] John B Goodenough, R Manoharan, and M Paranthaman. Surface protonation and electrochemical activity of oxides in aqueous solution. *Journal of the American Chemical Society*, 112(6):2076–2082, 1990.

[68] Isabela C. Man, Hai Yan Su, Federico Calle-Vallejo, Heine A. Hansen, José I. Martínez, Nilay G. Inoglu, John Kitchin, Thomas F. Jaramillo, Jens K. Nørskov, and Jan Rossmeisl. Universality in Oxygen Evolution Electrocatalysis on Oxide Surfaces. *ChemCatChem*, 3(7):1159–1165, 2011.

[69] J. Rossmeisl, A. Logadottir, and J.K. Nørskov. Electrolysis of water on (oxidized) metal surfaces. *Chemical Physics*, 319(1):178 – 184, 2005.

[70] J. Rossmeisl, Z.-W. Qu, H. Zhu, G.-J. Kroes, and J.K. Norskov. Electrolysis of water on oxide surfaces. *Journal of Electroanalytical Chemistry*, 607(1-2):83–89, 2007.

[71] Marc T.M. Koper. Thermodynamic theory of multi-electron transfer reactions: Implications for electrocatalysis. *Journal of Electroanalytical Chemistry*, 660(2):254 – 260, 2011. Physics and Chemistry of Charge Transfer in Condensed Media.

[72] Venkatasubramanian Viswanathan and Heine Anton Hansen. Unifying solution and surface electrochemistry: Limitations and opportunities in surface electrocatalysis. *Topics in Catalysis*, 57(1):215–221, 2014.

[73] S. Raabe, D. Mierwaldt, J. Ciston, M. Uijttewaal, H. Stein, J. Hoffmann, Y. Zhu, P. Blöchl, and C. Jooss. In situ electrochemical electron microscopy study of oxygen evolution activity of doped manganite perovskites. *Adv. Funct. Mater.*, 22(16):3378–3388, 2012.

[74] Daniel Mierwaldt, Stephanie Mildner, Rosa Arrigo, Axel Knop-Gericke, Emanuel Franke, Andreas Blumenstein, Jörg Hoffmann, and Christian Jooss. In Situ XANES/XPS Investigation of Doped Manganese Perovskite Catalysts. *Catalysts*, 4(2):129–145, 2014.

[75] J. Tyler Mefford, Xi Rong, Artem M. Abakumov, William G. Hardin, Sheng Dai, Alexie M. Kolpak, Keith P. Johnston, and Keith J. Stevenson. Water electrolysis on $La_{1-x}Sr_xCoO_{3-\delta}$ perovskite electrocatalysts. *Nature Communications*, 7:11053, 2016.

[76] Xi Rong, Jules Parolin, and Alexie M. Kolpak. A Fundamental Relationship between Reaction Mechanism and Stability in Metal Oxide Catalysts for Oxygen Evolution. *ACS Catalysis*, 6(2):1153–1158, 2016.

[77] Kevin J. May, Christopher E. Carlton, Kelsey A. Stoerzinger, Marcel Risch, Jin Suntivich, Yueh-Lin Lee, Alexis Grimaud, and Yang Shao-Horn. Influence of Oxygen Evolution during Water Oxidation on the Surface of Perovskite Oxide Catalysts. *The Journal of Physical Chemistry Letters*, 3(22):3264–3270, 2012.

[78] Seo Hyoung Chang, Nemanja Danilovic, Kee-Chul Chang, Ram Subbaraman, Arvydas P. Paulikas, Dillon D. Fong, Matthew J. Highland, Peter M. Baldo, Vojislav R. Stamenkovic, John W. Freeland, Jeffrey A. Eastman, and Nenad M. Markovic. Functional links between stability and reactivity of strontium ruthenate single crystals during oxygen evolution. *Nature Communications*, 5:4191, 2014.

[79] Binghong Han, Marcel Risch, Yueh-Lin Lee, Chen Ling, Hongfei Jia, and Yang Shao-Horn. Activity and stability trends of perovskite oxides for oxygen evolution catalysis at neutral pH. *Phys. Chem. Chem. Phys.*, 17(35):22576–22580, 2015.

[80] Alexis Grimaud, Kevin J May, Christopher E Carlton, Yueh-Lin Lee, Marcel Risch, Wesley T Hong, Jigang Zhou, and Yang Shao-Horn. Double perovskites as a family of highly active catalysts for oxygen evolution in alkaline solution. *Nature communications*, 4:2439, 2013.

[81] A Grimaud, W T Hong, Y Shao-Horn, and J M Tarascon. Anionic redox processes for electrochemical devices. *Nature Materials*, 15(2):121–126, 2016.

[82] Chunzhen Yang and Alexis Grimaud. Factors Controlling the Redox Activity of Oxygen in Perovskites: From Theory to Application for Catalytic Reactions. *Catalysts*, 7(5):149, 2017.

[83] M. Wohlfahrt-Mehrens and J. Heitbaum. Oxygen evolution on Ru and $RuO_2$ electrodes studied using isotope labelling and on-line mass spectrometry. *Journal of Electroanalytical Chemistry and Interfacial Electrochemistry*, 237(2):251–260, 1987.

[84] Stéphane Fierro, Tina Nagel, Helmut Baltruschat, and Christos Comninellis. Investigation of the oxygen evolution reaction on $Ti/IrO_2$ electrodes using isotope labelling and on-line mass spectrometry. *Electrochemistry Communications*, 9(8):1969–1974, 2007.

[85] Katerina Macounova, Marina Makarova, and Petr Krtil. Oxygen evolution on nanocrystalline $RuO_2$ and $Ru_{0.9}Ni_{0.1}O_{2-\delta}$ electrodes – DEMS approach to reaction mechanism determination. *Electrochemistry Communications*, 11(10):1865–1868, 2009.

[86] Maija M. Kuklja, Yuri A. Mastrikov, Bavornpon Jansang, and Eugene A. Kotomin. The Intrinsic Defects, Disordering, and Structural Stability of

$Ba_xSr_{1-x}Co_yFe_{1-y}O_{3-\delta}$ Perovskite Solid Solutions. *The Journal of Physical Chemistry C*, 116(35):18605–18611, 2012.

[87] Yuri A. Mastrikov, Rotraut Merkle, Eugene A. Kotomin, Maija M. Kuklja, and Joachim Maier. Formation and migration of oxygen vacancies in $La_{1-x}Sr_xCo_{1-y}Fe_yO_{3-\delta}$ perovskites: insight from ab initio calculations and comparison with $Ba_{1-x}Sr_xCo_{1-y}Fe_yO_{3-\delta}$. *Phys. Chem. Chem. Phys.*, 15:911–918, 2013.

[88] Christian Jooss, Stephanie Mildner, Marco Beleggia, Daniel Mierwaldt, and Vladimir Roddatis. *ETEM Studies of Electrodes and Electro-catalysts*, pages 301–329. Springer International Publishing, Cham, 2016.

[89] CH Hamann and W Vielstich. *Elektrochemie, 4., vollst. überarb. und aktualisierte Aufl.* Wiley-VCH, Weinheim, 2005.

[90] Ronald F Probstein. *Physicochemical hydrodynamics: an introduction*. John Wiley & Sons, 2005.

[91] Charles E Mortimer and Ulrich Müller. *Chemie: Das Basiswissen der Chemie; 126 Tabellen*. Georg Thieme Verlag, 2007.

[92] D.C. Koningsberger, B.L. Mojet, G.E. van Dorssen, and D.E. Ramaker. XAFS spectroscopy; fundamental principles and data analysis. *Topics in Catalysis*, 10(3):143–155, May 2000.

[93] Matthew Newville. Fundamentals of XAFS. *Reviews in Mineralogy and Geochemistry*, 78(1):33–74, 2014.

[94] B. H. Frazer, B. Gilbert, B. R. Sonderegger, and G. de Stasio. The probing depth of total electron yield in the sub-keV range: TEY-XAS and X-PEEM. *Surf. Sci.*, 537:161–167, 2003.

[95] E M Vass, M Hävecker, S Zafeiratos, D Teschner, A Knop-Gericke, and R Schlögl. The role of carbon species in heterogeneous catalytic processes:an in situ soft x-ray photoelectron spectroscopy study. *Journal of Physics: Condensed Matter*, 20(18):184016, 2008.

[96] Axel Knop-Gericke, Evgueni Kleimenov, Michael Hävecker, Raoul Blume, Detre Teschner, Spiros Zafeiratos, Robert Schlögl, Valerii I. Bukhtiyarov, Vasily V. Kaichev, Igor P. Prosvirin, Alexander I. Nizovskii, Hendrik Bluhm, Alexei Barinov,

Pavel Dudin, and Maya Kiskinova. Chapter 4: X-ray photoelectron spectroscopy for investigation of heterogeneous catalytic processes. In Bruce C. Gates and Helmut Knözinger, editors, *Advances in Catalysis*, volume 52, pages 213 – 272. Academic Press, 2009.

[97] Rosa Arrigo, Michael Hävecker, Manfred E. Schuster, Chinmoy Ranjan, Eugen Stotz, Axel Knop-Gericke, and Robert Schlögl. In situ study of the gas-phase electrolysis of water on platinum by nap-xps. *Angewandte Chemie International Edition*, 52(44):11660–11664, 2013.

[98] Michele Lazzeri and Annabella Selloni. Stress-Driven Reconstruction of an Oxide Surface: The Anatase $TiO_2$(001)-(1x4) Surface. *Phys. Rev. Lett.*, 87:266105, Dec 2001.

[99] R. Pentcheva, F. Wendler, H. L. Meyerheim, W. Moritz, N. Jedrecy, and M. Scheffler. Jahn-Teller Stabilization of a "Polar" Metal Oxide Surface: $Fe_3O_4$(001). *Phys. Rev. Lett.*, 94:126101, Apr 2005.

[100] D. Thompsett. *Handbook of Fuel Cells*, chapter Pt alloys as oxygen reduction catalysts. John Wiley & Sons, Ltd, 2010.

[101] Hai-Yan Su, Yelena Gorlin, Isabela C. Man, Federico Calle-Vallejo, Jens K. Norskov, Thomas F. Jaramillo, and Jan Rossmeisl. Identifying active surface phases for metal oxide electrocatalysts: a study of manganese oxide bifunctional catalysts for oxygen reduction and water oxidation catalysis. *Phys. Chem. Chem. Phys.*, 14:14010–14022, 2012.

[102] Rasmus Frydendal, Elisa A. Paoli, Brian P. Knudsen, Björn Wickman, Paolo Malacrida, Ifan E. L. Stephens, and Ib Chorkendorff. Benchmarking the Stability of Oxygen Evolution Reaction Catalysts: The Importance of Monitoring Mass Losses. *ChemElectroChem*, 1(12):2075–2081, 2014.

[103] Xi Rong and Alexie M. Kolpak. Ab Initio Approach for Prediction of Oxide Surface Structure, Stoichiometry, and Electrocatalytic Activity in Aqueous Solution. *The Journal of Physical Chemistry Letters*, 6(9):1785–1789, 2015. PMID: 26263350.

[104] Ray F Egerton. *Electron energy-loss spectroscopy in the electron microscope*. Springer Science & Business Media, 2011.

[105] Stephanie Mildner, Marco Beleggia, Daniel Mierwaldt, Thomas W. Hansen, Jakob B. Wagner, Sadegh Yazdi, Takeshi Kasama, Jim Ciston, Yimei Zhu, and Christian Jooss. Environmental TEM study of electron beam induced electrochemistry of $Pr_{0.64}Ca_{0.36}MnO_3$ catalysts for oxygen evolution. *Journal of Physical Chemistry C*, 119(10):5301–5310, 2015.

[106] P Butler and K Hale. In situ gas-solid reactions. *Practical Methods in Electron Microscopy*, 9:239, 1981.

[107] Pratibha L. Gai. Developments in in situ Environmental Cell High-Resolution Electron Microscopy and Applications to Catalysis. *Topics in Catalysis*, 21(4):161–173, 2002.

[108] Renu Sharma. An environmental transmission electron microscope for in situ synthesis and characterization of nanomaterials. *Journal of Materials Research*, 20(7):1695–1707, 2005.

[109] T. W. Hansen, J. B. Wagner, and R. E. Dunin-Borkowski. Aberration corrected and monochromated environmental transmission electron microscopy: challenges and prospects for materials science. *Materials Science and Technology*, 26(11):1338–1344, 2010.

[110] Binghong Han, Kelsey A. Stoerzinger, Vasiliki Tileli, Andrew D. Gamalski, Eric A. Stach, and Yang Shao-Horn. Nanoscale structural oscillations in perovskite oxides induced by oxygen evolution. *Nature Materials*, 1(October), 2016.

[111] Max Haider, Harald Rose, Stephan Uhlemann, Eugen Schwan, Bernd Kabius, and Knut Urban. A spherical-aberration-corrected 200kv transmission electron microscope. *Ultramicroscopy*, 75(1):53–60, 1998.

[112] Maximilian Haider, Harald Rose, Stephan Uhlemann, Bernd Kabius, and Knut Urban. Towards 0.1 nm resolution with the first spherically corrected transmission electron microscope. *Journal of Electron Microscopy*, 47(5):395–405, 1998.

[113] B. Freitag, S. Kujawa, P.M. Mul, J. Ringnalda, and P.C. Tiemeijer. Breaking the spherical and chromatic aberration barrier in transmission electron microscopy. *Ultramicroscopy*, 102(3):209–214, 2005.

[114] O.L. Krivanek, G.J. Corbin, N. Dellby, B.F. Elston, R.J. Keyse, M.F. Murfitt, C.S. Own, Z.S. Szilagyi, and J.W. Woodruff. An electron microscope for the aberration-corrected era. *Ultramicroscopy*, 108(3):179 – 195, 2008.

[115] Lan Yun Chang, Amanda S. Barnard, Lionel Cervera Gontard, and Rafal E. Dunin-Borkowski. Resolving the Structure of Active Sites on Platinum Catalytic Nanoparticles. *Nano Letters*, 10(8):3073–3076, 2010. PMID: 20666362.

[116] David B. Williams and C. Barry Carter. *The Transmission Electron Microscope*. Springer US, Boston, MA, 1996.

[117] Jacques Cazaux. Mechanisms of charging in electron spectroscopy. *Journal of Electron Spectroscopy and Related Phenomena*, 105(2):155 – 185, 1999.

[118] Stephanie Mildner. *$Pr_{1\text{-}x}Ca_xMnO_3$ for Catalytic Water Splitting-Optical Properties and In Situ ETEM Investigations*. PhD thesis, Georg-August-Universität Göttingen, 2015.

[119] V. E. Cosslett. Radiation damage in the high resolution electron microscopy of biological materials: A review. *Journal of Microscopy*, 113(2):113–129, 1978.

[120] R.F. Egerton, P. Li, and M. Malac. Radiation damage in the TEM and SEM. *Micron*, 35(6):399 – 409, 2004. International Wuhan Symposium on Advanced Electron Microscopy.

[121] Federico Calle-Vallejo, José I. Martínez, Juan M. García-Lastra, Mogens Mogensen, and Jan Rossmeisl. Trends in stability of perovskite oxides. *Angewandte Chemie - International Edition*, 49(42):7699–7701, 2010.

[122] B. Raveau. The crucial role of mixed valence in the magnetoresistance properties of manganites and cobaltites. *Philos. T. Roy. Soc. A*, 366(1862):83–92, 2008.

[123] S. Grenier, J. P. Hill, Doon Gibbs, K. J. Thomas, M. v. Zimmermann, C. S. Nelson, V. Kiryukhin, Y. Tokura, Y. Tomioka, D. Casa, T. Gog, and C. Venkataraman. Resonant x-ray diffraction of the magnetoresistant perovskite $Pr_{0.6}Ca_{0.4}MnO_3$. *Phys. Rev. B*, 69:134419, 2004.

[124] F. M. F. de Groot, J. C. Fuggle, B. T. Thole, and G. A. Sawatzky. 2p x-ray absorption of 3d transition-metal compounds: An atomic multiplet description including the crystal field. *Phys. Rev. B*, 42:5459–5468, 1990.

[125] M. M. Grush, J. Chen, T. L. Stemmler, S. J. George, C. Y. Ralston, R. T. Stibrany, A. Gelasco, G. Christou, S. M. Gorun, J. E. Penner-Hahn, and S. P. Cramer. Manganese l-edge x-ray absorption spectroscopy of manganese catalase from lactobacillus plantarum and mixed valence manganese complexes. *J. Am. Chem. Soc.*, 118(1):65–69, 1996.

[126] S. Imada, S. Suga, T. Muro, S. Ueda, R.-J. Jung, M. Kotsugi, Y. Saitoh, T. Matsushita, H. Kuwahara, H. Moritomo, and Y. Tokura. Local magnetic states in $La_{1-x}Sr_xMnO_3$ and $Nd_{1-x}Sr_xMnO_3$. *Physica B*, 281&282:498–499, 2000.

[127] G. Subías, J. García, M. C. Sánchez, J. Blasco, and M. G. Proietti. Soft x-ray absorption spectroscopy (Mn $L_{2,3}$ and O K) in mixed valence manganites. *Surf. Rev. Let.*, 09:1071–1078, 2002.

[128] H. Kanamori, T. Yoshioka, K. Hirose, and T. Yamamoto. Determination of valence state of Mn ions in $Pr_{1-x}A_xMnO_{3-\delta}$ (A = Ca, Sr) by Mn-$L_3$ X-ray absorption near-edge structure analysis. *J. Electron Spectrosc.*, 185:129–132, 2012.

[129] M. Abbate, F. M. F. de Groot, J. C. Fuggle, A. Fujimori, O. Strebel, F. Lopez, M. Domke, G. Kaindl, G. A. Sawatzky, M. Takano, Y. Takeda, H. Eisaki, and S. Uchida. Controlled-valence properties of $La_{1-x}Sr_xFeO_3$ and $La_{1-x}Sr_xMnO_3$ studied by soft-x-ray absorption spectroscopy. *Phys. Rev. B*, 46:4511–4519, 1992.

[130] R. S. Liu, J. B. Wu, C. Y. Chang, J. G. Lin, C. Y. Huang, J. M. Chen, and R. G. Liu. Determination of Mn valence from x-ray absorption near edge structure and study of magnetic behavior in hole-doped $(Nd_{1-x}Ca_x)MnO_3$ system. *J. Solid State Chem.*, 125(1):112–115, 1996.

[131] H. K. Schmid and W. Mader. Oxidation states of Mn and Fe in various compound oxide systems. *Micron*, 37(5):426–432, 2006.

[132] T. Riedl, T. Gemming, W. Gruner, J. Acker, and K. Wetzig. Determination of manganese valency in $La_{1-x}Sr_xMnO_3$ using elnes in the (S)TEM. *Micron*, 38:224–230, 2007.

[133] F. M. F. de Groot, M. Grioni, J. C. Fuggle, J. Ghijsen, G. A. Sawatzky, and H. Petersen. Oxygen 1s x-ray-absorption edges of transition-metal oxides. *Phys. Rev. B*, 40:5715–5723, 1989.

[134] G. Saucke, J. Norpoth, C. Jooss, D. Su, and Y. Zhu. Polaron absorption for photovoltaic energy conversion in a manganite-titanate pn heterojunction. *Phys. Rev. B*, 85:165315, 2012.

[135] J. H. Jung, K. H. Kim, D. J. Eom, T. W. Noh, E. J. Choi, Jaejun Yu, Y. S. Kwon, and Y. Chung. Determination of electronic band structures of $CaMnO_3$ and $LaMnO_3$ using optical-conductivity analyses. *Phys. Rev. B*, 55:15489–15493, 1997.

[136] K. Mette, A. Bergmann, J.-P. Tessonnier, M. Hävecker, L. Yao, T. Ressler, R. Schlögl, P. Strasser, and M. Behrens. Nanostructured manganese oxide supported on carbon nanotubes for electrocatalytic water splitting. *ChemCatChem*, 4(6):851–862, 2012.

[137] G. Cressey, C. M. B. Henderson, and G. Laan. Use of L-edge x-ray absorption spectroscopy to characterize multiple valence states of 3d transition metals; a new probe for mineralogical and geochemical research. *Phys. Chem. Miner.*, 20(2):111–119, 1993.

[138] J. M. Alonso, R. Cortés-Gil, L. Ruiz-González, J. M. González-Calbet, A. Hernando, M. Vallet-Regí, M. E. Dávila, and M. C. Asensio. Influence of the synthetic pathway on the properties of oxygen-deficient manganese-related perovskites. *Eur. J. Inorg. Chem.*, 2007(21):3350–3355, 2007.

[139] B. Gilbert, B. H. Frazer, A. Belz, P. G. Conrad, K. H. Nealson, D. Haskel, J. C. Lang, G. Srajer, and G. De Stasio. Multiple scattering calculations of bonding and x-ray absorption spectroscopy of manganese oxides. *J. Phys. Chem. A*, 107(16):2839–2847, 2003.

[140] S. P. Cramer, F. M. F. DeGroot, Y. Ma, C. T. Chen, F. Sette, C. A. Kipke, D. M. Eichhorn, M. K. Chan, and W. H. Armstrong. Ligand field strengths and oxidation states from manganese L-edge spectroscopy. *J. Am. Chem. Soc.*, 113:7937–7940, 1991.

[141] M. J. Montenegro, T. Lippert, S. Müller, A. Weidenkaff, P. R. Willmott, and A. Wokaun. Pulsed laser deposition of electrochemically active perovskite films. *Appl. Surf. Sci.*, 197-198:505–511, 2002.

[142] M. J. Montenegro, M. Döbeli, T. Lippert, S. Müller, B. Schnyder, A. Weidenkaff, P. R. Willmott, and A. Wokaun. Pulsed laser deposition of $La_{0.6}Ca_{0.4}CoO_3$

(LCCO) films. a promising metal-oxide catalyst for air based batteries. *Phys. Chem. Chem. Phys.*, 4:2799–2805, 2002.

[143] Jianrong Niu, Jiguang Deng, Wei Liu, Lei Zhang, Guozhi Wang, Hongxing Dai, Hong He, and Xuehong Zi. Nanosized perovskite-type oxides $La_{1-x}Sr_xMO_{3-\delta}$ (M = Co, Mn; x = 0, 0.4) for the catalytic removal of ethylacetate. *Catal. Today*, 126:420–429, 2007.

[144] Y. Zhang-Steenwinkel, J. Beckers, and A. Bliek. Surface properties and catalytic performance in CO oxidation of cerium substituted lanthanum-manganese oxides. *Appl. Catal. A - Gen.*, 235:79–92, 2002.

[145] J. Choi, J. Zhang, S.-H. Liou, P. A. Dowben, and E. W. Plummer. Surfaces of the perovskite manganites $La_{1-x}Ca_xMnO_3$. *Phys. Rev. B*, 59:13453–13459, 1999.

[146] J.-C. Dupin, D. Gonbeau, P. Vinatier, and A. Levasseur. Systematic XPS studies of metal oxides, hydroxides and peroxides. *Phys. Chem. Chem. Phys.*, 2:1319–1324, 2000.

[147] J. L. G. Fierro and L. G. Tejuca. Non-stoichiometric surface behaviour of $LaMO_3$ oxides as evidenced by XPS. *Appl. Surf. Sci.*, 27(4):453–457, 1987.

[148] G. A. Somorjai and Y. Li. *Introduction to Surface Chemistry and Catalysis*. Wiley, New York, USA, 1994.

[149] R. Follath, F. Senf, and W. Gudat. Plane-grating monochromator at BESSY II using collimated light. *J. Synchrotron Rad.*, 5:769–771, 1998.

[150] D. A. Shirley. High-resolution x-ray photoemission spectrum of the valence bands of gold. *Phys. Rev. B*, 5:4709–4714, 1972.

[151] Stephen Fletcher. Tafel slopes from first principles. *Journal of Solid State Electrochemistry*, 13(4):537–549, 2009.

[152] J B Goodenough and B L Cushing. Oxide-based ORR catalysts. In *Handbook of Fuel Cells*, volume 2, pages 1–14. John Wiley & Sons, Ltd, Chichester, UK, dec 2010.

[153] Ivelina Zaharieva, M. Mahdi Najafpour, Mathias Wiechen, Michael Haumann, Philipp Kurz, and Holger Dau. Synthetic manganese-calcium oxides mimic the water-oxidizing complex of photosynthesis functionally and structurally. *Energy & Environmental Science*, 4(7):2400, 2011.

[154] Ivelina Zaharieva, Petko Chernev, Marcel Risch, Katharina Klingan, Mike Kohlhoff, Anna Fischer, and Holger Dau. Electrosynthesis, functional, and structural characterization of a water-oxidizing manganese oxide. *Energy & Environmental Science*, 5(5):7081, 2012.

[155] Yelena Gorlin, Benedikt Lassalle-Kaiser, Jesse D Benck, Sheraz Gul, Samuel M Webb, Vittal K Yachandra, Junko Yano, and Thomas F Jaramillo. In Situ X-ray Absorption Spectroscopy Investigation of a Bifunctional Manganese Oxide Catalyst with High Activity for Electrochemical Water Oxidation and Oxygen Reduction. *J. Am. Chem. Soc.*, 135(23):8525, 2013.

[156] Alejandra Ramírez, Philipp Hillebrand, Diana Stellmach, Matthias M. May, Peter Bogdanoff, and Sebastian Fiechter. Evaluation of $MnO_x$, $Mn_2O_3$, and $Mn_3O_4$ Electrodeposited Films for the Oxygen Evolution Reaction of Water. *The Journal of Physical Chemistry C*, 118(26):14073–14081, 2014.

[157] Majid Ebrahimizadeh Abrishami, Marcel Risch, Julius Scholz, Vladimir Roddatis, Norbert Osterthun, and Christian Jooss. Oxygen Evolution at Manganite Perovskite Ruddlesden-Popper Type Particles: Trends of Activity on Structure, Valence and Covalence. *Materials*, 9(11):921, 2016.

[158] I. Zaharieva, D. González-Flores, B. Asfari, C. Pasquini, M. R. Mohammadi, K. Klingan, I. Zizak, S. Loos, P. Chernev, and H. Dau. Water oxidation catalysis – role of redox and structural dynamics in biological photosynthesis and inorganic manganese oxides. *Energy Environ. Sci.*, 9(7):2433–2443, 2016.

[159] Yang-Gang Wang, Donghai Mei, Vassiliki-Alexandra Glezakou, Jun Li, and Roger Rousseau. Dynamic formation of single-atom catalytic active sites on ceria-supported gold nanoparticles. *Nature Communications*, 6:6511, 2015.

[160] Huilei Zhao, Fuping Pan, and Ying Li. A review on the effects of $TiO_2$ surface point defects on $CO_2$ photoreduction with $H_2O$. *Journal of Materiomics*, 3(1):17–32, 2017.

[161] Julius Scholz, Marcel Risch, Kelsey A. Stoerzinger, Garlef Wartner, Yang Shao-Horn, and Christian Jooss. Rotating Ring–Disk Electrode Study of Oxygen Evolution at a Perovskite Surface: Correlating Activity to Manganese Concentration. *The Journal of Physical Chemistry C*, 120(49):27746–27756, 2016.

[162] Julius Scholz, Marcel Risch, Garlef Wartner, Christoph Luderer, Vladimir Roddatis, and Christian Jooss. Tailoring the Oxygen Evolution Activity and Stability Using Defect Chemistry. *Catalysts*, 7(5):139, 2017.

[163] Dongkyu Lee and Ho Lee. Controlling Oxygen Mobility in Ruddlesden–Popper Oxides. *Materials*, 10(4):368, 2017.

[164] Takashi Nakamura, Yihan Ling, and Koji Amezawa. The effect of interstitial oxygen formation on the crystal lattice deformation in layered perovskite oxides for electrochemical devices. *Journal of Materials Chemistry A*, 3(19):10471–10479, 2015.

[165] Qiang Gao, Chinmoy Ranjan, Zoran Pavlovic, Raoul Blume, and Robert Schlögl. Enhancement of Stability and Activity of $MnO_x$/Au Electrocatalysts for Oxygen Evolution through Adequate Electrolyte Composition. *ACS Catalysis*, 5(12):7265–7275, 2015.

[166] J. Suntivich, W.T. T Hong, Y.-L. Lee, J.M. M Rondinelli, W. Yang, J.B. B Goodenough, B. Dabrowski, J.W. W Freeland, and Y. Shao-Horn. Estimating Hybridization of Transition Metal and Oxygen States in Perovskites from O K-edge X-ray Absorption Spectroscopy. *The Journal of Physical Chemistry C*, 118:1856–1863, 2014.

[167] William G. Hardin, J. Tyler Mefford, Daniel A. Slanac, Bijal B. Patel, Xiqing Wang, Sheng Dai, Xin Zhao, Rodney S. Ruoff, Keith P. Johnston, and Keith J. Stevenson. Tuning the electrocatalytic activity of perovskites through active site variation and support interactions. *Chemistry of Materials*, 26(11):3368–3376, 2014.

[168] Ulrich Aschauer, Reto Pfenninger, Sverre M. Selbach, Tor Grande, and Nicola A. Spaldin. Strain-controlled oxygen vacancy formation and ordering in $CaMnO_3$. *Physical Review B - Condensed Matter and Materials Physics*, 88(5):1–7, 2013.

[169] Ravini U. Chandrasena, Weibing Yang, Qingyu Lei, Mario U. Delgado-Jaime, Kanishka D. Wijesekara, Maryam Golalikhani, Bruce A. Davidson, Elke Arenholz, Keisuke Kobayashi, Masaaki Kobata, Frank M. F. de Groot, Ulrich Aschauer, Nicola A. Spaldin, Xiaoxing Xi, and Alexander X. Gray. Strain-Engineered Oxygen Vacancies in $CaMnO_3$ Thin Films. *Nano Lett.*, 17(2):794–799, 2017.

[170] Thilo Kramer, Malte Scherff, Daniel Mierwaldt, Joerg Hoffmann, and Christian Jooss. Role of oxygen vacancies for resistive switching in noble metal sandwiched $Pr_{0.67}Ca_{0.33}MnO_{3-\delta}$. *Applied Physics Letters*, 110(24):243502, 2017.

[171] Lisbeth Rørmark, Kjell Wiik, Svein Stølen, and Tor Grande. Oxygen stoichiometry and structural properties of $La_{1-x}A_xMnO_{3\pm\delta}$ ($A = Ca$ or Sr and $0 \leq x \leq 1$). *Journal of Materials Chemistry*, 12:1058–1067, 2002.

[172] E I Leonidova, A A Markov, M V Patrakeev, I A Leonidov, and V L Kozhevnikov. Oxygen Nonstoichiometry and the Thermodynamic and Structural Properties of Double Perovskites $PrBaCo_{2-x}Cu_xO_{5+\delta}$. *Russian Journal of Physical Chemistry*, 83(5):2009–2009, 2009.

[173] Anirban Das, Enxhi Xhafa, and Eranda Nikolla. Electro- and thermal-catalysis by layered, first series Ruddlesden-Popper oxides. *Catalysis Today*, 277:214–226, 2016.

[174] Jin Suntivich, Hubert A Gasteiger, Naoaki Yabuuchi, and Yang Shao-Horn. Electrocatalytic Measurement Methodology of Oxide Catalysts Using a Thin-Film Rotating Disk Electrode. *Journal of The Electrochemical Society*, 157(8):B1263–B1268, 2010.

[175] Philipp Rheinländer, Sebastian Henning, Juan Herranz, and Hubert A Gasteiger. Comparing Hydrogen Oxidation and Evolution Reaction Kinetics on Polycrystalline Platinum in 0.1 M and 1 M KOH. *ECS Transactions*, 50(2):2163–2174, 2013.

[176] G. H. Smith and R. E. Burge. The analytical representation of atomic scattering amplitudes for electrons. *Acta Crystallographica*, 15:182–186, 1962.

[177] Thilo Kramer, Daniel Mierwaldt, Malte Scherff, Mike Kanbach, and Christian Jooss. Developing an in situ environmental TEM set up for investigations of resistive switching mechanisms in Pt–$Pr_{1-x}Ca_xMnO_{3-\delta}$–Pt sandwich structures. *Ultramicroscopy*, in review, 2016.

[178] M. Varela, M. P. Oxley, W. Luo, J. Tao, M. Watanabe, A. R. Lupini, S. T. Pantelides, and S. J. Pennycook. Atomic-resolution imaging of oxidation states in manganites. *Physical Review B - Condensed Matter and Materials Physics*, 79(8):1–14, 2009.

[179] Christoph Koch. *Determination of core structure periodicity and point defect density along dislocations*. PhD thesis, Arizona State University, 2002.

[180] Dmitri Golberg, Pedro MFJ Costa, Masanori Mitome, and Yoshio Bando. Nanotubes in a gradient electric field as revealed by stm tem technique. *Nano Research*, 1(2):166–175, 2008.

[181] Zhi Xu, Dmitri Golberg, and Yoshio Bando. In situ tem-stm recorded kinetics of boron nitride nanotube failure under current flow. *Nano Letters*, 9(6):2251–2254, 2009. PMID: 19413292.

[182] Wenyao Li, Qian Liu, Yangang Sun, Jianqing Sun, Rujia Zou, Gao Li, Xianghua Hu, Guosheng Song, Guanxiang Ma, Jianmao Yang, et al. $Mno_2$ ultralong nanowires with better electrical conductivity and enhanced supercapacitor performances. *Journal of Materials Chemistry*, 22(30):14864–14867, 2012.

[183] K.L. Klein, I.M. Anderson, and N. De Jonge. Transmission electron microscopy with a liquid flow cell. *Journal of Microscopy*, 242(2):117–123, 2011.

# Author Contributions

This thesis includes two articles which present original research by the author and have been published or submitted for publication:

Chapter 2:

**In Situ XANES/XPS Investigation of Doped Manganese Perovskite Catalysts**
*Catalysts* **2014**, *4*(2), 129 - 145

Chapter 3:

**Environmental TEM Investigation of Electrochemical Stability of Perovskite and Ruddlesden-Popper Type Manganite Oxygen Evolution Catalysts**
submitted for publication to *Advanced Sustainable Systems*

XANES and XPS results on thin film specimens in Chapter 2 as well as in Figures 3.1 d and 3.2 a (Chapter 3) were obtained at the BESSY II synchrotron facility of the Helmholtz-Zentrum Berlin, Germany (HZB). The near ambient-pressure XPS endstation of the Fritz-Haber-Institut of the Max-Planck-Gesellschaft (FHI-MPG) at the ISISS beamline was used. XAS of nanoparticles presented in Figures 3.1 d and 3.2 b-c was recorded at the Canadian Light Source (Saskatoon, Canada). Author contributions for both articles are disclosed in the following.

Thin film specimens for the study in Chapter 2 were prepared by the author (all Ca-doped PCMO specimens) and Dr. Stephanie Mildner ($PrMnO_3$). Characterization by scanning electron microscopy (SEM) and X-ray diffraction (XRD) was performed by the author, except for post mortem SEM by Andreas Blumenstein. XANES and XPS measurements were performed by the author under guidance of Dr. Rosa Arrigo and Dr. Axel Knop-Gericke (FHI-MPG) and with support by Emanuel Franke, Dr. Stephanie Mildner, Andreas Blumenstein and Helge Stein. The CV measurements (including preparation of the thin film electrode) were conducted by the author. All data in this study were analyzed by the author. The manuscript was primarily written by the author in collaboration with Dr. Jörg Hoffmann and Prof. Christian Jooß.

Thin film specimens for the study in Chapter 3 were prepared by the author. The P- and RP-PCMO powders were synthesized by Dr. Majid Ebrahimizadeh Abrishami. Nanoparticle TEM specimens were prepared by Dr. Vladimir Roddatis. ETEM experiments were carried out and analyzed by the author and Dr. Vladimir Roddatis. RRDE measurements (including preparation of the oxide disk electrodes) were conducted and analyzed by Julius Scholz and Janis Geppert. XAS of thin films (Figures 3.1 d and 3.2 a) was part of the measurements described for the study in Chapter 2. XAS of nanoparticles was conducted by Dr. Marcel Risch (Figures 3.1 d and 3.2 b-c). Simulation of high-resolution TEM images was performed by Dr. Vladimir Roddatis. The manuscript was primarily written by the author in collaboration with Dr. Marcel Risch, Prof. Christian Jooß, and Dr. Vladimir Roddatis.

# Acknowledgments

I would like to thank several colleagues, family and friends who supported my work and contributed to the success of this thesis in various ways.

First of all, I am very grateful to my thesis adviser Prof. Christian Jooß for his committed guidance, motivation and confidence in my work. I am also very thankful to Prof. Simone Techert for her supervision and many inspiring discussions.

My resounding thanks go to Dr. Vladimir Roddatis for our countless productive hours at the ETEM and his remarkable specimen preparation skills.

Moreover, I thank Dr. Rosa Arrigo and Dr. Axel Knop-Gericke from the Fritz-Haber-Institut who supported the fruitful synchrotron experiments at BESSY II, as well as Dr. Stephanie Mildner, Emanuel Franke and Andreas Blumenstein for their support during the beamtime.

I greatly benefited from the collaboration with further members of the Institut für Materialphysik, to whom I owe sincere thanks: Dr. Majid Ebrahimizadeh Abrishami prepared the oxide powders on which the exciting ETEM experiments were performed. Interpretation of the ETEM results was substantially supported by ex situ experiments performed by Dr. Marcel Risch, Julius Scholz and Janis Geppert as well as TEM work in collaboration with Dr. Stephanie Mildner.

Furthermore, I owe special gratitude to Dr. Jörg Hoffmann for his motivational support and enlightening discussions. My gratitude naturally extends to several not specifically mentioned (current and former) PhD, master and bachelor students as well as technicians at the Institut für Materialphysik. I also thank the Deutsche Forschungsgemeinschaft (DFG) for the financial support within the Sonderforschungsbereich 1073.

Last but not least, I wholeheartedly thank my beloved wife Sandra as well as my family and friends for their moral and emotional support throughout the years.